Technische Universität München

Fakultät für Physik
Lehrstuhl für Neutronenstreuung

Mathematical Analysis of the Phase Problem for *in situ* Neutron Reflectometry using an Algorithmic Approach

Alexander Book

Vollständiger Abdruck der von der Fakultät für Physik der Technischen Universität München zur Erlangung des akademischen Grades eines

Doktors der Naturwissenschaften (Dr. rer. nat.)

genehmigten Dissertation.

Vorsitzender:
Prof. Dr. Martin Zacharias

Prüfende der Dissertation:
1. Prof. Dr. Peter Böni
2. Prof. Dr. Christian Back

Die Dissertation wurde am 01.09.2021 bei der Technischen Universität München eingereicht und durch die Fakultät für Physik am 15.10.2021 angenommen.

Abstract

Polarized neutron reflectometry (PNR) is a power tool to investigate the atomic and magnetic structure of thin films. The measured reflectivity, however, cannot be mapped to a unique sample description as the complex reflection coefficient (or phase information) is lost during the data acquisition.

In this work, the theory for phase-sensitive PNR is presented based on reference layers, which uniquely determine the reflection. A comparison with traditional data fitting techniques for PNR is carried out, which demonstrates the advantages of the more sophisticated phase-sensitive PNR technique.

As the reference layer method allows only the reconstruction of the reflection above the total reflection edge, a fixed-point algorithm is presented which retrieves the missing reflection. Without this information, the inversion of the reflection to recover the sample description is futile. The fixed-point algorithm only requires the knowledge of the total film thickness to guarantee the convergence to a superb approximation of the reflection. Studies based on actual experiments and simulated data are successfully carried out.

The feasibility of phase-sensitive PNR technique is demonstrated using *in situ* PNR measurements on Cu/Fe thin films. The reconstruction is based on magnetic Fe reference layers, whose nuclear and magnetic structure is varied. Two different reference layer approaches are compared.

Zusammenfassung

Polarisierte Neutronen Reflektometrie (PNR) ist ein mächtiges Werkzeug, um die atomare und magnetische Struktur von dünnen Schichten zu untersuchen. Die gemessene Reflektivität kann jedoch nicht einer Probenbeschreibung eindeutig zugeordnet werden, da der komplexe Reflektionskoeffizient (bzw. Phaseninformation) während der Datenakquisition verloren geht.

In dieser Arbeit wird die Theorie für phasensensitive PNR basierend auf Referenzschichten vorgestellt, welche die Reflektion eindeutig bestimmt. Ein Vergleich mit der herkömmlichen Ausgleichsrechnung für PNR wird getätigt, der die Vorteile der anspruchsvolleren phasensensitiven PNR Technik aufzeigt.

Die Methode der Referenzschichten ermöglicht die Rekonstruktion der Reflektion nur oberhalb der Totalreflektionskante, weshalb ein Fixpunkt–Algorithmus vorgestellt wird, der die fehlende Reflektion wiederherstellt. Ohne diese Information ist eine Invertierung der Reflektion, um die Probenbeschreibung zu erlangen, erfolglos. Der Algorithmus benötigt nur die Kenntnis der gesamten Probendicke, um eine Konvergenz zu einer hervorragenden Approximation der Reflektion zu gewährleisten. Studien basierend auf tatsächlichen Experimenten und simulierten Daten werden erfolgreich durchgeführt.

Die Machbarkeit der phasensensitiven PNR Technik wird anhand von *in situ* PNR Messungen an Cu/Fe Dünnschichten demonstriert. Die Rekonstruktion basiert auf magnetischen Fe Referenzschichten, dessen nukleare und magnetische Struktur variiert wird. Es werden zwei verschiedene Ansätze von Referenzschichten verglichen.

Contents

1 Introduction

Thin film and heterostructures gave rise to a whole new world of interesting physical phenomena. The reduced dimensionality of a layer or the influence of two surfaces on each other changes the internal physical properties and processes of an object and are, therefore, different from those of a bulk material. Moreover, advances in this scientific field are accomplished due to reliable and highly adjustable thin film deposition techniques like molecular beam epitaxy, thermal evaporation, pulsed laser deposition or sputter deposition which allows the systematic production of samples with varying characteristics.

The discovery of novel physical phenomena like the giant magnetoresistance (GMR) [1, 2] or the tunnel magnetoresistance (TMR) [3–5] has led to an increasing interest in the magnetism and morphology of thin films and heterostructures. These phenomena (GMR, TMR) play an important role in spintronics [6], e. g. magnetoresistive random access memory (MRAM), magnetic sensors or logic devices [7]. The investigation of the structural composition and magnetic structure of heterostructures leads to a deeper understanding of these phenomena. Parameters like film thickness, interfaces and density play a crucial role for the appearance of these phenomena. In the case of (i) Fe/Cr multilayers the GMR decreases with an increase in the Cr layer thickness due to the weakening of antiferromagnetic coupling between the Fe layers [1] or in (ii) Fe/MgO/Fe sandwich junctions the TMR is enhanced with an increase in the MgO layer thickness [8]. These correlations are then used to fine tune the physical properties of thin films in applications.

An ideal tool to analyze both the morphology and magnetic structure of thin films is polarized neutron reflectometry (PNR) [9–13]. It is a non-destructive scattering technique, capable of resolving the structural and magnetic depth profile of a thin film or heterostructures on length scales between 10 Å up to several hundred nanometers. PNR is sensitive to light elements and isotopes [14] due to the unique properties of neutrons which can be exploited by variation of contrast of specific components by isotopic substitution, e. g. deuteration [15, 16].

A mathematical analysis of the acquired PNR data extracts the desired information by fitting a model to the reflectivity data. This approach, however, has several drawbacks, namely, (i) the fitting is time consuming and impedes the evaluation of the feedback from experiments which may be carried out in much shorter time scales [17] (ii) it requires *a priori* knowledge of the sample to set up a suitable model and (iii) the extracted information is neither unique nor necessarily correct due to the *phase problem*: In reflectometry experiments the measured quantity is the squared modulus of the complex reflection, i. e. the reflectivity. The phase information is lost. Hence, a manifold of equiv-

alent models exists which generate the exact same reflectivity but differ in the reflection. This ambiguity is known as the phase problem.

Recent advances in artificial neural networks and machine learning [17–20] alleviate problems (i) and (ii) and research is still ongoing. These new tools can quickly and reliably (provided a proper training data set was used) estimate layer thickness, density and roughness of reflectivity curves, which are used as an initial prediction for a subsequent conventional fit and dramatically support the researcher. The predictions can be calculated within a few milliseconds [17] and the reliability depends on the training data set used for the learning process of the artificial neutral network [19]. For example, estimating the parameters of a four layer sample using a neural network which was trained on reflectivity curves with no more than three layers will not be successful.

In this thesis, the novel technique of *in situ* polarized neutron reflectometry is utilized to tackle the phase problem (iii). The aim is to develop a framework in which the phase information or reflection is retrieved using *in situ* PNR measurements to track the evolution of a sample. Additionally, tools for the reconstruction of the reflection and inversion of the sample description are implemented and for a practical assessment of the quality of the retrieved reflection, the influence of various systematic and random (statistical) measurement uncertainties is analyzed. Measurements of Fe/Cu thin films conducted at the neutron reflectometer Amor at the Swiss Spallation Neutron Source, Paul Scherrer Institut, Villigen have been successfully analyzed and prove the feasibility of phase reconstruction for *in situ* PNR which provides a unique sample description.

This work is arranged in three main chapters. The basic theory of neutron reflectometry is introduced in chapter 2. The primary features of a reflectometry curve are explained using the Born-Approximation and the exact reflection computation within the dynamical theory is shown to derive important facts about the reflection.

The two main analysis techniques in neutron reflectometry which are data fitting and the method of potential inversion with phase reconstruction is discussed in chapter 3. For this purpose, the reflection reconstruction using reference layers is presented and an algorithm to retrieve the reflection at the total reflection edge is described together with two simulated examples. Additionally, the influence of limitations of the measurement, e. g. bandwidth limitation, resolution and measurement noise on the retrieved reflection and inverted potential is simulated and discussed.

The developed framework of phase sensitive *in situ* polarized neutron reflectometry is then applied in chapter 4 to a Fe/Cu thin film to yield a unique determination of the sample structure. Subsequently, the influence of the reference layer on the quality of the reconstructed reflection is discussed and an extrapolation of the reflection is carried out to eliminate bandwidth limitation effects.

Definitions and Notation

The L^p space is a function space which contains all measurable functions which have a finite p-Norm:

$$L^p \coloneqq \{f \colon \mathbb{R} \to \mathbb{R} \text{ measurable } : \|f\|_{L^p} < +\infty\} \tag{1.1}$$

with the usual norm

$$\|f\|_{L^p} \coloneqq \left(\int_{\mathbb{R}} |f(x)|^p \mathrm{d}x \right)^{1/p}. \tag{1.2}$$

For $f \in L^1$, the non-unitary Fourier transform $\mathcal{F}$ is defined by

$$\mathcal{F}[f](q) = \int_{-\infty}^{\infty} f(z) e^{-iqz} \mathrm{d}z \tag{1.3}$$

and the corresponding inverse Fourier transform of a function $\hat{f}$ is then

$$\mathcal{F}^{-1}[\hat{f}](z) = \frac{1}{2\pi} \int_{-\infty}^{\infty} \hat{f}(q) e^{iqz} \mathrm{d}q. \tag{1.4}$$

The *Heaviside* function Θ is defined by

$$\Theta(z) = \begin{cases} 0, & z < 0 \\ 1, & z \geq 0 \end{cases} \tag{1.5}$$

and its (improper) Fourier transform is $\mathcal{F}[\Theta](q) = (iq)^{-1}$ [21].

The *characteristic* or *indicator* function of a set $S \subset \mathbb{R}$ is denoted by χ_S and defined as

$$\chi_S(x) = \begin{cases} 1, & x \in S \\ 0, & \text{otherwise} \end{cases}. \tag{1.6}$$

The *complement* of a set $S \subset \mathbb{R}$ is $S^{\complement} \coloneqq \mathbb{R} \setminus S$, the *identity* matrix in $\mathbb{R}^{n \times n}$ is denoted by $\mathbb{1}_n$ and the complex conjugation of $z \in \mathbb{C}$ is indicated by $\overline{z}$.

Let X be a topological space and $f \colon X \to \mathbb{R}$ a function. The support of f is the closure of the non-zeros of f

$$\operatorname{supp} f \coloneqq \overline{\{x \in X \mid f(x) \neq 0\}}. \tag{1.7}$$

2 Neutron Reflectometry

In a neutron reflectometry experiment a beam of neutrons with a well-defined incident wave vector $\vec{k}_i \in \mathbb{R}^3$ interacts with the sample under investigation. Due to the interactions between the sample and the neutrons, the neutrons are scattered to a different state with reflected wave vector $\vec{k}_r$ (figure 2.1).

In free space, a neutron is represented by a plane wave ψ with a wave vector $\vec{k}$ by

$$\psi(\vec{k}, \vec{r}) = e^{i\vec{k}\cdot\vec{r}}. \tag{2.1}$$

As usual, the squared modulus of the wave function $|\psi|^2$ is interpreted as the probability density of finding the neutron in a given location ($\vec{r}$) and momentum ($\vec{k}$). The interaction of the neutron with the sample is described by the time-independent Schrödinger-equation

$$\left[V(\vec{r}) - \frac{\hbar^2}{2m}\nabla^2\right]\psi = E\psi, \tag{2.2}$$

where m is the neutrons mass, V is the interaction (scattering) potential, $\hbar$ is the reduced Planck constant and E is the total energy. Assuming elastic scattering ($|\vec{k}_i| = |\vec{k}_r|$), the total energy equals the kinetic energy of a neutron in free space

$$E = \frac{\hbar^2|\vec{k}_i|^2}{2m}. \tag{2.3}$$

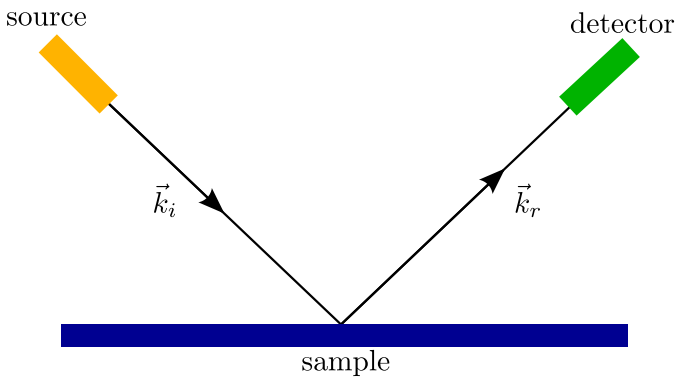

Figure 2.1: Schematic of a reflectometry experiment. Incident neutrons with wave vector $\vec{k}_i$ interact with the sample and are reflected with wave vector $\vec{k}_r$.

2.1 Nuclear Scattering Potential

The interaction of a neutron with a nucleus located at position $\vec{R}$ can be described with the Fermi pseudopotential [22, 23] by

$$V(\vec{r}) = \frac{2\pi\hbar^2}{m} b\delta(\vec{r} - \vec{R}), \tag{2.4}$$

where δ is the Dirac delta distribution and b is the bound coherent neutron scattering length. Inside a material with a collection of nuclei j located at $\vec{R}_j$, the neutron beam interacts with the sum of nuclear scattering potentials, i. e.

$$V(\vec{r}) = \frac{2\pi\hbar^2}{m} \sum_j b_j \delta(\vec{r} - \vec{R}_j). \tag{2.5}$$

If, instead, assuming a continuous distribution of matter[1], the (nuclear) scattering interaction potential V can be expressed as

$$V(\vec{r}) = \frac{2\pi\hbar^2}{m} \rho_n(\vec{r}), \tag{2.6}$$

where ρ_n is the nuclear scattering length density (SLD) and defined as [24, 25]

$$\rho_n = \mathcal{N}_A \frac{\sum_j n_j b_j}{\sum_j n_j M_j} \rho_{\text{density}}. \tag{2.7}$$

The variable ρ_{density} denotes the mass density of the material, $\mathcal{N}_A$ is the Avogadro constant, M_j is the molar mass, b_j is the bound scattering length and n_j is the number of the j-th constituent in a unit volume.

The bound scattering length $b = b' + ib''$ of a nucleus is a complex quantity. It is related to the scattering and absorption cross section by [14, 26]

$$\begin{aligned} \sigma_{\text{s}} &= 4\pi|b|^2, \\ \sigma_{\text{abs}} &= \frac{4\pi}{k} b''. \end{aligned} \tag{2.8}$$

The imaginary part b'' corresponds to the absorption of a neutron by the nucleus. In neutron reflectometry with cold neutrons (1 Å to 10 Å) the imaginary part of the SLD is negligible for most materials; exceptions are e. g. Gd, Eu, Sm and Cd. The real part b' describes the magnitude of refraction of the neutron with the material.

For x-rays, the SLD is similarly defined, however, since the incident wave mainly interacts with the electron cloud of the atoms, the scattering length is [27]

$$b_{\text{X-ray}} = Z + f' + if'', \tag{2.9}$$

[1] In fact, this assumption is supported by simulations with varying discretizations step sizes, i. e. atomic scale granularity, see figure 2.10.

where Z is the atomic number and f', f'' are correction terms depending on the specific atom and x-ray wavelength being used. In comparison with neutron scattering the absorption effects for x-rays cannot be neglected.

2.2 Magnetic Scattering Potential

Neutrons do not carry any electric charge, however, they have a magnetic dipole moment $\vec{\mu}_n$ which interacts with the atomic magnetic moments in samples. Being spin-$\frac{1}{2}$ particles, neutrons have a quantized associated spin angular momentum allowing only two discrete energy states in a magnetic field $\vec{H}$ (spin-up $(+)$ and spin-down $(-)$). The two discrete neutron spin states are parallel to the axis of quantization, which is defined by the direction of a magnetic field $\vec{H}$.

The magnetic interaction corresponding to a spin state is described by the Zeeman energy [25]

$$V_{\mathrm{mag},\pm} = \mp\mu_n|\vec{B}|, \tag{2.10}$$

where $\vec{B}$ is the magnetic induction and $\mu_n \approx -9.66 \times 10^{-27}\,\mathrm{J/T}$. The magnetic contribution adds to the total scattering interaction potential V_{total},

$$V_{\mathrm{total}} = V_{\mathrm{nuclear}} + V_{\mathrm{mag},\pm} \tag{2.11}$$

and a magnetic SLD $\rho_m^{\pm} = \mp\frac{m}{2\pi\hbar^2}\mu_n B$ is introduced to express the total scattering interaction by

$$V_{\mathrm{total}} = \frac{2\pi\hbar^2}{m}\left(\rho_n + \rho_m^{\pm}\right) = \frac{2\pi\hbar^2}{m}\left(\mathcal{N}_A\frac{\sum_j n_j b_j}{\sum_j n_j M_j}\rho_{\mathrm{density}} \mp \frac{m}{2\pi\hbar^2}\mu_n B\right). \tag{2.12}$$

The (total) SLD $\rho^{\pm}$ is defined as the sum of the nuclear and magnetic SLD

$$\rho^{\pm} = \rho_n + \rho_m^{\pm}. \tag{2.13}$$

In the following the explicit spin dependence of the SLD is suppressed, i. e. $\rho = \rho^{\pm}$.

2.3 Reflection

Substituting the SLD and kinetic energy $E = \frac{\hbar^2 k_i^2}{2m}$ into the Schrödinger-equation (2.2) yields the three dimensional wave equation

$$[k_{i,x,y,z}^2 - 4\pi\rho + \nabla^2]\psi = 0, \tag{2.14}$$

where $k_{i,x,y,z}$ is the neutron wave vector in free space and $\nabla^2 = \sum_j \frac{\partial^2}{\partial x_j^2}$ is the Laplace operator. If the scattering potential (or equivalently the SLD) varies only along z, no force along the x and y direction can act on the neutron and the corresponding moments

and wave vectors components are conserved, resulting in a reduction of dimensionality

$$\left[k^2 - 4\pi\rho + \frac{\partial^2}{\partial z^2}\right]\psi = 0, \tag{2.15}$$

with $k = k_{i,z}$.

2.3.1 Helmholtz Equation

Before considering solutions of the wave equation for neutron and x-ray reflectometry, it is instructive to consider the Helmholtz equation in only one spatial dimension:

$$\frac{\partial^2\psi}{\partial z^2} = -k^2\psi, \tag{2.16}$$

where k^2 is the eigenvalue and ψ the eigenfunction of the equation. Note that the Helmholtz equation originates from the wave equation in reflectometry (2.15) by removing the scattering potential, i. e. $V = \rho = 0$. Also the Helmholtz equation is the time-independent representation of the wave equation

$$\frac{\partial^2\psi}{\partial x^2} - \frac{1}{c^2}\frac{\partial^2\psi}{\partial t^2} = 0 \tag{2.17}$$

after a separation of variables. Solutions of the Helmholtz equation are of the form

$$\psi(k, z) = e^{\pm ikz}. \tag{2.18}$$

The wave equation in reflectometry can be viewed as a perturbation of the Helmholtz equation, hence, if the perturbation ρ is of sufficient decay at $\pm\infty$ it is plausible that solutions of the wave equation exist which have the same asymptotics as solutions of the Helmholtz equation for $z \to \pm\infty$. The pertubation ρ is sufficiently decaying at infinity if $\|z\rho(z)\|_{L^1(\mathbb{R})} < \infty$ [28].

Indeed, reformulating the wave equation (2.15) as an integral equation at $\pm\infty$ yields the following representation [29] for $k \neq 0$ called the Jost equation

$$\psi^+(k, z) = e^{+ikz} - 4\pi k^{-1}\int_z^\infty \sin\left(k(z-\xi)\right)\rho(\xi)\psi^+(k, \xi)\mathrm{d}\xi, \tag{2.19}$$

$$\psi^-(k, z) = e^{-ikz} + 4\pi k^{-1}\int_{-\infty}^z \sin\left(k(z-\xi)\right)\rho(\xi)\psi^-(k, \xi)\mathrm{d}\xi. \tag{2.20}$$

If ψ solves one of the integral equations then ψ is a solution of the wave equation as well. The point here is that for sufficiently decaying perturbations ρ the solution $\psi^\pm$ behaves as $e^{\pm ikz}$ as $z \to \pm\infty$.

From a mathematical point of view, these integral equations are of great interest. They are Volterra type integral equations and a standard method of solving them is by successive iteration [30], also known as Picard iteration.

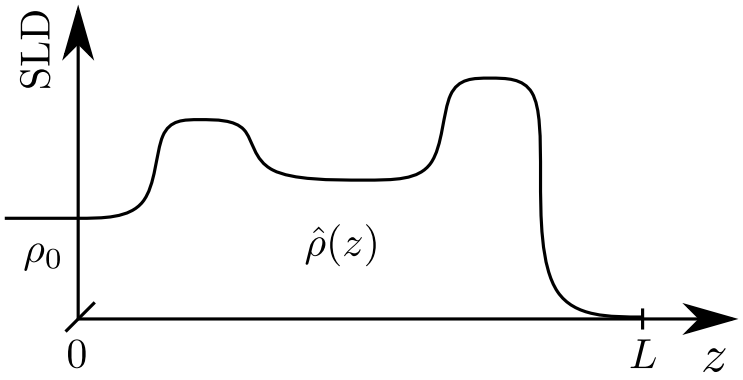

Figure 2.2: Exemplary SLD distribution of a sample corresponding to equation (2.21).

2.3.2 Reflection Coefficient

The coordinate system of the sample is chosen such that the substrate extends towards $z = -\infty$ and the top surface is at $z = 0$. The structure of the sample is depicted in figure 2.2. More precisely, the structure of the SLD is assumed to be of the form

$$\rho(z) = \begin{cases} \rho_0, & z \leq 0 \\ \hat{\rho}(z), & 0 \leq z \leq L \\ 0, & L \leq z \end{cases} \tag{2.21}$$

with $L > 0$ denoting the film thickness of the sample.

Trivial solutions of the wave equation (2.15) with a constant SLD are $\psi(z) = e^{\pm i\kappa z}$ with $\kappa^2 = k^2 - 4\pi\rho$, which correspond to solutions of the Helmholtz equation with a shift of the wave vector by the SLD. Hence, in the region $z \geq L$ with the scattering potential being zero, the general solution is the superposition of an incident plane wave with amplitude I traveling to $z \to -\infty$ and with a reflected plane wave with amplitude R propagating to $z \to \infty$

$$\psi(k, z) \sim Ie^{-ikz} + R(k)e^{ikz}, \quad z \to \infty \tag{2.22}$$

The incident amplitude I is usually normalized to 1. The variable R is called the reflection (coefficient), which is in general a complex quantity and cannot be measured directly. Likewise, in the region $z \leq 0$ the solution ψ behaves asymptotically as

$$\psi(k, z) \sim T(k)e^{-ikn(k)z}, \quad z \to -\infty, \tag{2.23}$$

where T is the transmitted amplitude and $n(k) = \sqrt{1 - 4\pi\rho_0/k^2}$ is the refractive index of the substrate for $k^2 > \rho_0$.

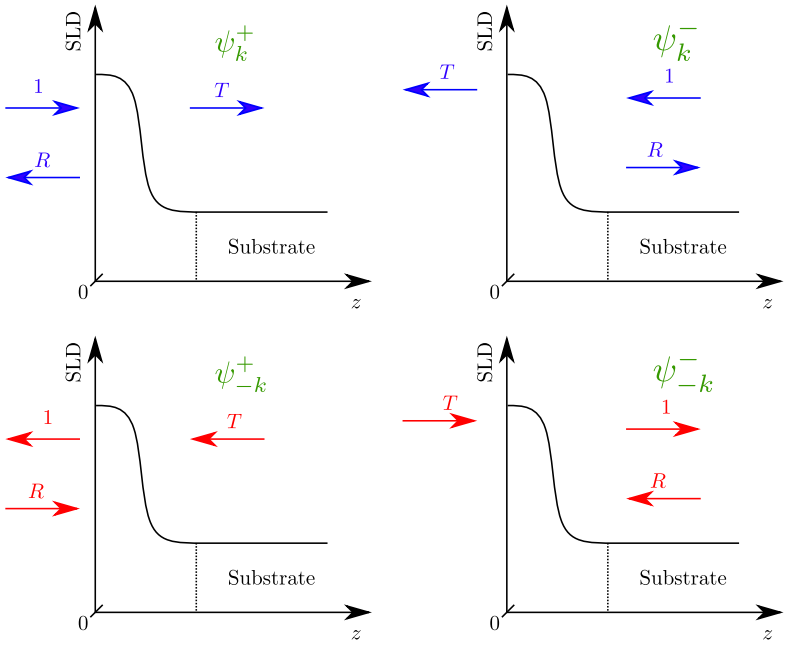

Figure 2.3: Illustration of the four different situations corresponding to $\psi_{\pm k}^{\pm}$ of the wave equation (2.15). The solution ψ^+ travel trough air and is reflected at the top layer whereas ψ^- travel through substrate and is reflected at the bottom layer. The change $\psi_k \to \psi_{-k}$ describes a reversal of time.

Proposition 1. *Let ψ be a solution of the wave equation* (2.15) *such that the asymptotics* (2.22) *and* (2.23) *for $z \to \pm\infty$ hold. Then the reflection for $k \neq 0$ can be calculated by*

$$R(k) = \frac{2\pi}{ik} \int_{-\infty}^{\infty} e^{-ikz} \rho(z) \psi(k, z) \mathrm{d}z.$$

Proof. Multiplying equation (2.15) by $\varphi(k, x) := e^{-ikx}$ and integrating gives

$$\begin{aligned} 4\pi \int_a^b \varphi(k, z) \rho(z) \psi(k, z) \mathrm{d}z &= \int_a^b k^2 \psi\varphi + \varphi\psi'' \mathrm{d}z \\ &= \left[\psi'\varphi + ik\psi\varphi\right]_a^b - \int_a^b \varphi'\psi' + ik\psi\varphi \mathrm{d}z \\ &= \left[\psi'\varphi - \psi\varphi'\right]_a^b = W[\psi, \varphi](b) - W[\psi, \varphi](a) \end{aligned}$$

where integration by parts was used and the last integral on the right hand side vanishes. The right hand side is called the Wronskian W and is defined as $W[f, g] = f'g - fg'$. Passing to the limit $a \to -\infty$ and $b \to \infty$ yields

$$4\pi \int_{-\infty}^{\infty} \varphi(k, z) \rho(z) \psi(k, z) \mathrm{d}z = 2ikR(k),$$

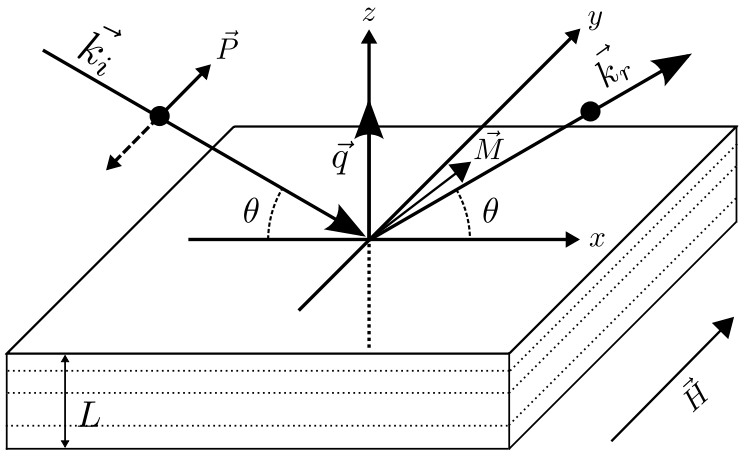

Figure 2.4: Illustration of specular reflection from a thin film of thickness L. The neutrons are polarized along the polarization axis $\vec{P}$, which is perpendicular to $\vec{q}$ and defined by the external magnetic guide field $\vec{H}$. The sample magnetization $\vec{M}$ lies in-plane and can vary from layer to layer.

since $W[\psi,\varphi](b) \to 2ikR(k)$ and $W[\psi,\varphi](a) \to 0$ hold due to the asymptotics of ψ at $z \to \pm\infty$. In particular $W[\psi,\varphi](b) \to W[e^{-ikx} + R(k)e^{ikx}, e^{-ikx}] = 2ikR(k)$ as $b \to +\infty$. Note that φ was chosen to be the solution of the wave equation with $\rho = 0$. A more general statement holds even by taking φ as a solution of the wave equation (2.15) with non-zero SLD, see [31, 32]. □

Assuming elastic and specular scattering, the incidence and reflected wave vector of a neutron plane wave have the same modulus, i. e. $k_i = k_r = k$. The resulting wave vector transfer q_z is then equal to

$$q_z = \left|\vec{k}_r - \vec{k}_i\right| = 2k_z = \frac{4\pi}{\lambda}\sin\theta, \tag{2.24}$$

where θ is the angle of incidence relative to the samples surface.

The squared absolute value of the reflection R is called the reflectivity $|R|^2$, which is the quantity measured in reflectometry experiments as a function of the moment transfer $q = q_z$. In experiments it is measured by

$$|R|^2 = \frac{\text{Number of reflected neutrons}}{\text{Number of incident neutrons}}. \tag{2.25}$$

As neutrons interact with the magnetic field inside the sample, the reflectivity is spin-dependent. Thus, polarized neutron reflectometry (PNR) can resolve the samples magnetization as a function of depth and due to the Halperin effect, only the component of the film magnetization perpendicular to the neutron wave vector transfer q is probed [25].

2.3.3 Total Reflection and Critical Wave Vector

Total reflection refers to the physical phenomena when all incoming neutrons are reflected at the interface of two (non-absorbing) materials. The reflectivity $|R|^2$ is then equal to 1, however, the reflection R itself is an element of the unit circle in the complex plane and is usually not equal to 1.

Materials with a positive SLD are optically denser than air for neutrons and it is possible for neutrons to be totally reflected at the interface for a specific critical angle θ_c. From Snell's law, the critical angle is

$$\theta_c = \arccos n(k) \approx \lambda\sqrt{\rho/\pi}, \tag{2.26}$$

where θ is the angle of grazing incidence, i. e. the angle between the neutron beam and the surface, and n the refractive index of the material for neutrons, which can be expressed as

$$n(k) = \sqrt{1 - 4\pi\rho/k^2}. \tag{2.27}$$

For $k^2 < 4\pi\rho$, the refractive index is extended to $n(k) = i\sqrt{4\pi\rho/k^2 - 1}$. Expressing the critical angle in terms of the critical wave vector results in

$$q_c = \frac{4\pi}{\lambda}\sin\theta_c = \sqrt{16\pi\rho}. \tag{2.28}$$

An alternative way of describing the total reflection is as follows. Total reflection occurs if the energy of the neutron is not sufficient to penetrate into the sample, i. e. if the kinetic energy of the neutron is smaller than the scattering potential. This immediately leads to the equation of the critical wave vector and the refractive index comes from the difference of the kinetic energy with the scattering potential in the wave equation (2.15), namely

$$\left[k^2 n^2 + \frac{\partial^2}{\partial z^2}\right]\psi = 0. \tag{2.29}$$

2.3.4 Symmetry of the Reflection

This section shows the symmetry relation $\overline{R(k)} = R(-k)$ and $\overline{T(k)} = T(-k)$ if the scattering potential is real valued, i. e. the sample is non-absorbing. This relation will be important later in this work for the calculation of the Fourier transform of R as it is reduced to a simpler cosine or sine transform over only half of the k space.

There is a common misconception of the quantity $R(-k)$. It does not correspond to the reflection of the "reversed" sample, i. e. the back reflection that is measured when "flipping" the sample upside down. $R(-k)$ rather corresponds to the mathematical extension of the reflection to negative wave vector transfers, which are in general not possible to measure.

The wave equation (2.15) has in general two solutions as it is a second order linear differential equation. A specific solution is specified by the asymptotic behavior as $z \to +\infty$ or $z \to -\infty$. As previously stated, the two solutions of the wave equation

satisfy either one of the following integral equations

$$\begin{aligned}\psi_k^+(z) &= e^{+ikz} - 4\pi k^{-1}\int_z^\infty \sin\left(k(z-\xi)\right)\rho(\xi)\psi_k^+(\xi)\mathrm{d}\xi,\\ \psi_k^-(z) &= e^{-ikz} + 4\pi k^{-1}\int_{-\infty}^z \sin\left(k(z-\xi)\right)\rho(\xi)\psi_k^-(\xi)\mathrm{d}\xi.\end{aligned} \tag{2.30}$$

The solution ψ^+ corresponds to the reflectometry setup, when the neutrons impinge on the surface (top), whereas ψ^- corresponds to the reversed case, when the neutrons travel through the substrate and impinge on the flipped sample (bottom). See figure 2.3 for an illustration of the described situations. From a mathematical point of view, ψ^- originates from ψ^+ when changing $\rho(z) \to \rho(-z)$ in the integral equations (2.30). Hence, ψ^- is also called the *reversed* wave ψ^+ as it originates by simply reversing ρ.

Furthermore, the wave equation is invariant under the change $k \to -k$ since k appears as a squared quantity in the wave equation. This property can be verified with the integral equations as well. Thus there are two additional solutions ψ_{-k}^+ and ψ_{-k}^-. The wave ψ_{-k}^+ is thus called the *mirrored* wave of ψ_k^+ since it originates by mirroring the z axis (in principle a reversing of ρ is required as well, but this makes the naming convention unnecessarily complicated). The four solutions are linearly dependent as the solution space is only two dimensional. Thus, it is possible to find coefficients $\alpha_k^+, \beta_k^+ \in \mathbb{C}$ such that

$$\psi_k^- = \alpha_k^+\psi_k^+ + \beta_k^+\psi_{-k}^+. \tag{2.31}$$

Setting it equal with the asymptotic solution in (2.22) and (2.23) yields

$$\psi(k,z) = T(k)\psi_k^-(z) = 1\psi_{-k}^+(z) + R(k)\psi_k^+(z). \tag{2.32}$$

After dividing by T, one finds the following relations for the reflection and transmission coefficient

$$\beta_k^+ = \frac{1}{T(k)}, \quad \alpha_k^+ = \frac{R(k)}{T(k)}. \tag{2.33}$$

To derive the symmetry of R and T, it is sufficient to show that $\overline{\alpha_k^+} = \alpha_{-k}^+$ and $\overline{\beta_k^+} = \beta_{-k}^+$ holds.

Taking the complex conjugate of the integral equations (2.30) will result in exactly the same integral equation when replacing $k \to -k$ if the SLD ρ is real. Since the equation has a unique solution, it follows that $\overline{\psi_k^\pm} = \psi_{-k}^\pm$ and thus the symmetry of R and T follows immediately when considering equation (2.31) as well.

2.3.5 Conservation of Probability and Number of Neutrons

For a non-absorbing material the number of incident neutrons should equal the number of transmitted plus reflected neutrons. In terms of the reflection and transmittance coefficient, the following equation holds

$$1 = |R(k)|^2 + |T(k)|^2. \tag{2.34}$$

This equation can also be read from a probabilistic point of view, stating that the total probability of finding a neutron being reflected or being transmitted is equal to unity.

Before stating a proof of the conservation of neutrons, a simple fact about the Wronskian is needed. The following lemma states that for solutions of the integral equations (2.30) the wave ψ_k^+ and the mirrored wave ψ_{-k}^+ are linearly independent and the Wronskian can be calculated explicitly for these solutions.

Lemma 1. *Let f, g be two solutions of the wave equation (2.15) for a fixed $k \in \mathbb{R} \setminus \{0\}$ with a real-valued ρ. The Wronskian $W[f,g]$ is constant and the integral equation solutions ψ^+, ψ^- satisfy $W[\psi_k^\pm, \psi_{-k}^\pm] = \pm 2ik$.*

Proof. Taking the derivative of $W[f,g]$ and observing that f and g solve the wave equation gives

$$\begin{aligned}\partial_z W[f(z), g(z)] &= f''(z)g(z) - f(z)g''(z) \\ &= \left(4\pi\rho(z) - k^2\right) f(z)g(z) - f(z)\left(4\pi\rho(z) - k^2\right) g(z) = 0.\end{aligned}$$

Hence, the Wronskian is constant in the limit $z \to +\infty$ as well and the solutions ψ_k^+ and ψ_{-k}^+ yield

$$W[\psi_k^+, \psi_{-k}^+] = \lim_{z\to\infty} W[\psi_k^+(z), \psi_{-k}^+(z)] = \lim_{z\to\infty} W[e^{ikz}, e^{-ikz}] = 2ik.$$

By taking the limit $z \to -\infty$, the Wronskian of $\psi_{\pm k}^-$ evaluates to $W[\psi_k^-, \psi_{-k}^-] = -2ik$. □

The value of the Wronskian corresponds to the frequency difference of ψ_k^+ and ψ_{-k}^+ which is to be expected since the waves have an asymptotic angular frequency of $\pm k$. This result allows to relate the Wronskian of $\psi_{\pm k}^-$ with the Wronskian of $\psi_{\pm k}^+$ by the coefficients $\alpha_{\pm k}^+$ and $\beta_{\pm k}^+$, which determine R and T.

Proposition 2. *Let ρ be a real-valued SLD. Then the total number of neutrons is conserved for any $k \in \mathbb{R} \setminus \{0\}$*

$$|T(k)|^2 + |R(k)|^2 = 1.$$

Proof. As shown in section 2.3.4, the solutions $\psi_{\pm k}^-$ are a linear combination of $\psi_{\pm k}^+$, and the Wronskian is by Lemma 1 given as

$$\begin{aligned}-2ik = W[\psi_k^-, \psi_{-k}^-] &= W[\alpha_k^+\psi_k^+ + \beta_k^+\psi_{-k}^+, \alpha_{-k}^+\psi_{-k}^+ + \beta_{-k}^+\psi_k^+] \\ &= \alpha_k^+\alpha_{-k}^+ W[\psi_k^+, \psi_{-k}^+] + \beta_k^+\beta_{-k}^+ W[\psi_{-k}^+, \psi_k^+] \\ &= 2ik\left(|\alpha_k^+|^2 - |\beta_k^+|^2\right),\end{aligned}$$

since $\overline{\alpha_k^+} = \alpha_{-k}^+$ and $\overline{\beta_k^+} = \beta_{-k}^+$. Thus, $|\beta_k^+|^2 = 1 + |\alpha_k^+|^2$ and the proposition follows by the relations $T(k) = 1/\beta_k^+$ and $R(k) = \alpha_k^+/\beta_k^+$. □

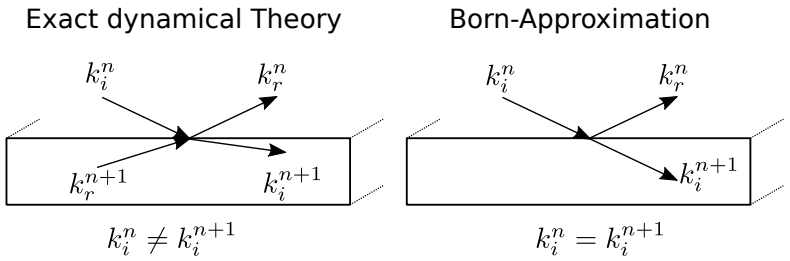

Figure 2.5: Illustration of the dynamical theory (exact) and the BA. The wave vector k_i^n and k_r^n the incidence and reflected wave from layer n, respectively.

In the context of the inversion of the reflection, i. e. retrieving the scattering potential from the reflection, the transmission coefficient does not need to be measured. The transmisson coefficient is related to the reflection: The modulus is computed by $|T(k)| = \sqrt{1 - |R(k)|^2}$ and the phase of the transmission can be computed by methods of complex analysis [33].

2.4 Born-Approximation

The above calculations are exact but not appropriate for making the transformation from real to reciprocal space transparent. For a better understanding of the reflection and reflectivity the (kinematic) Born-Approximation (BA) can be used. The gist of the BA is that the reflection can be expressed as the Fourier transform of the SLD.

The BA assumes that the solution ψ of the wave equation is not substantially distorted from the plane wave (2.1). In particular, the BA assumes the following [27]

1. No multiple reflections
2. The effects of refraction are neglected
3. The reflection is proportional to the variation in the SLD

The reflection is then computed by replacing ψ with the undistorted plane wave e^{-ikx} in the integral (1). The reflection is then just a Fourier transform of the SLD

$$R(q) = \frac{4\pi}{iq} \int_{-\infty}^{\infty} \rho(z) e^{-iqz} \mathrm{d}z = \frac{4\pi}{iq} \mathcal{F}[\rho](q), \tag{2.35}$$

where $q = 2k$ is the wave vector transfer, see equation (2.24).

The assumptions for the BA are valid for large q values. However, as $q \to 0$ the solution of the wave equation is substantially distorted from the free form by multiple reflections inside the sample or by total reflection at the top surface. Thus, for q being close to the critical wave vector transfer q_c, the BA fails to approximate the true reflection. In particular, the reflection diverges to infinity at $q = 0$ in the BA, whereas the true reflection is always bounded by one.

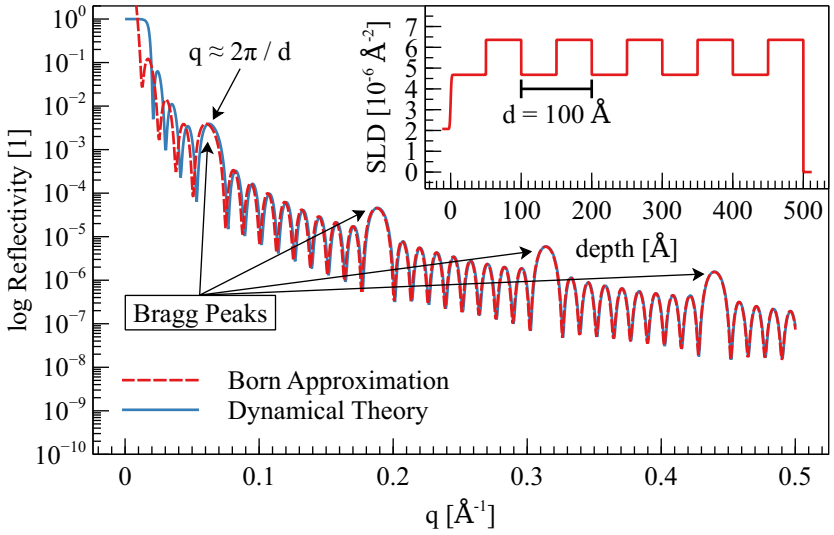

Figure 2.6: Comparison of the reflectivity computed using the BA and the exact dynamical theory of Si/[Au(50 Å)/Pt(50 Å)]$_5$/air. The inset shows the SLD of the multilayer sample used for the calculation of the reflectivity.

Figure 2.6 depicts the reflectivity computed by the BA and computed by the exact dynamical theory for an exemplary multilayer system. At small q, the assumption of an undistorted plane wave in the BA is violated, resulting in a significant mismatch of both curves. For large q, the BA is a good approximation to the dynamical theory.

If the SLD is continuously differentiable one can easily see by integration by parts that the reflection is only due to variations in the SLD. The derivative $\rho'(z)$ completely determines the reflection

$$R(q) = \frac{-4\pi}{q^2} \int_{-\infty}^{\infty} \rho'(z) e^{-iqz} \mathrm{d}z \tag{2.36}$$

and the reflectivity is expressed as

$$|R(q)|^2 = \frac{16\pi^2}{q^4} \left|\mathcal{F}[\rho'](q)\right|^2, \tag{2.37}$$

where $\mathcal{F}$ denotes the Fourier transform operator. For $q_c \ll q$ the reflectivity asymptotically decays as $\sim 1/q^4$ for a continuously differentiable SLD. If the SLD is even smoother, i. e. k times continuously differentiable, the reflectivity decays as $\sim 1/q^{2k+2}$ for $q \to \infty$.

2.4.1 Estimation of the Layer Thickness

Reflectometry can determine the thickness of individual layers inside a sample. The reflection may exhibit oscillations, called Kiessig fringes [34, 35], which correspond to

the thickness L of a layer inside the sample by

$$\Delta q = \frac{2\pi}{L}. \tag{2.38}$$

This relation between the period Δq and the layer thickness L can easily be shown using the BA. For this purpose consider the case of a single layer on a substrate:

$$\rho(z) = \begin{cases} \rho_0, & z \leq 0 \\ \rho_1, & 0 < z \leq L \\ 0, & \text{otherwise} \end{cases} \tag{2.39}$$

where $L > 0$ is the thickness of the top layer and ρ_0, ρ_1 are the SLDs of the substrate and the top layer, respectively. The SLD can be equivalently expressed by

$$\rho(z) = \rho_1 \Theta(L - z) - (\rho_1 - \rho_0)\Theta(-z), \tag{2.40}$$

where Θ denotes the Heaviside function.

The Fourier transform of the Heaviside function Θ does in principle not exist, however, by taking the average one can show that $\mathcal{F}[\Theta(z)](q) = \frac{1}{iq}$. Here, a δ-distribution at $z = 0$, which is responsible for the correct offset in the ordinate of the transform, is ignored since it is not influencing the following calculations. The reflection R is

$$R(q) = 4\pi \left(\rho_1 \frac{e^{iLq}}{q^2} - \frac{\rho_1 - \rho_0}{q^2} \right). \tag{2.41}$$

The oscillations by the first term are caused by the top layer and the frequency corresponds to the layer thickness L and equation (2.38) holds.

2.4.2 Bragg Peaks from Multilayer Repetitions

If the SLD contains repetitive features, the reflectivity exhibits Bragg peaks which originate from constructive interference. The Bragg equation [36]

$$2d \sin\theta = n\lambda \tag{2.42}$$

relates the thickness of a bilayer d to the angle θ and wavelength λ for the Bragg order $n \in \mathbb{N}$. In terms of the wave vector transfer, the Bragg equation can be expressed as

$$q = \frac{2\pi n}{d}. \tag{2.43}$$

Hence, the Bragg peaks for neutron and x-ray reflectivity are always at the same q value in the BA. However, some of the possible Bragg peaks will vanish due to destructive interference. figure 2.6 shows an example of such a situation with a repetitive multilayer structure with length scale $d = 100\,\text{Å}$. Only for $q = \frac{2\pi(2n+1)}{d} \approx (2n+1)0.0628\,\text{Å}^{-1}$ there is constructive interference, resulting in Bragg peaks.

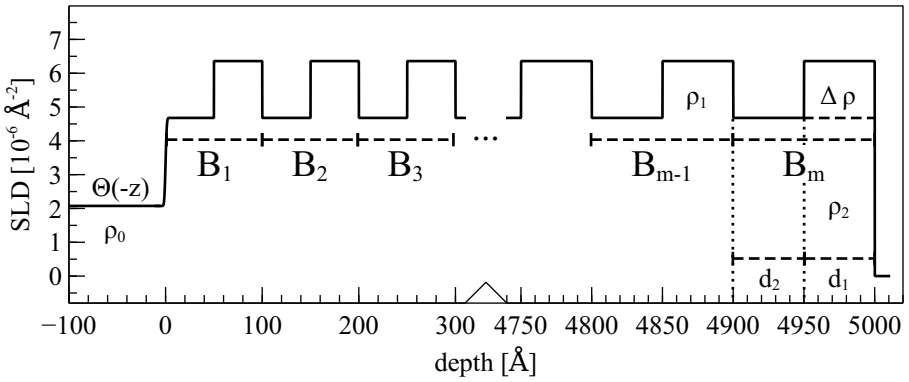

Figure 2.7: Schematic illustration of a SLD for a sample with m bilayers on a substrate. Each bilayer consists of two layers with thicknesses d_1 and d_2, and is represented by the bilayer function B. B_j is the function which is shifted by $j(d_1 + d_2)$ to the right.

To understand this feature in more detail consider the following sample SLD ρ with $m \in \mathbb{N}$ repetitive bilayers B

$$\rho(z) = (\rho_0 - \rho_2)\Theta(-z) + \sum_{j=1}^{m} B_j(z) + \rho_2\Theta(md - z), \tag{2.44}$$

where $B_j(z) = \Delta\rho\Theta(jd - z) - \Delta\rho\Theta(jd - d_1 - z)$ is a single bilayer representation shifted by $jd = j(d_1 + d_2)$ to the right with d_1, d_2 being the thicknesses and ρ_1, ρ_2 being the SLDs of the first and second layer of the bilayer. The difference $\Delta\rho = \rho_1 - \rho_2$ describes a jump from the first to the second layer inside the bilayer. The value ρ_0 is the SLD of the substrate.

The definition represents the repetitive structure quite well: The sample has three components where the second component corresponds to m bilayers. The first and third component are nuisance terms which are included for completeness. The first term corresponds to the jump from the bilayer to the substrate $\rho_2 \to \rho_0$. The third term is the jump from air to the bilayer $0 = \rho_{\text{air}} \to \rho_2$. More precisely, the jump is $\rho_{\text{air}} \to \rho_1$, hidden in the summation term of the bilayer. This subtlety allows "nice" ρ to be formulated: The sample consists of just a single layer of thickness md and the bilayer is merely a variation on top of the single layer. Figure 2.7 illustrates the sample description.

To calculate the reflection in the BA the Fourier transform of each component of the SLD is required. Recall that the Fourier transform of the Heaviside function is $\mathcal{F}[\Theta(z)](q) = \frac{1}{iq}$. The Fourier transform of a single bilayer is $\mathcal{F}[B_j](q) = -\frac{1}{iq}\Delta\rho e^{ijdq} + \frac{1}{iq}\Delta\rho e^{iq(jd-d_1)}$ by the translation[2] and scaling[3] property of Fourier transforms. Multi-

[2] $\mathcal{F}(f(z-d))(q) = e^{-idq}\mathcal{F}(f(z))(q)$
[3] $\mathcal{F}(f(-z))(q) = \mathcal{F}(f(z))(-q)$

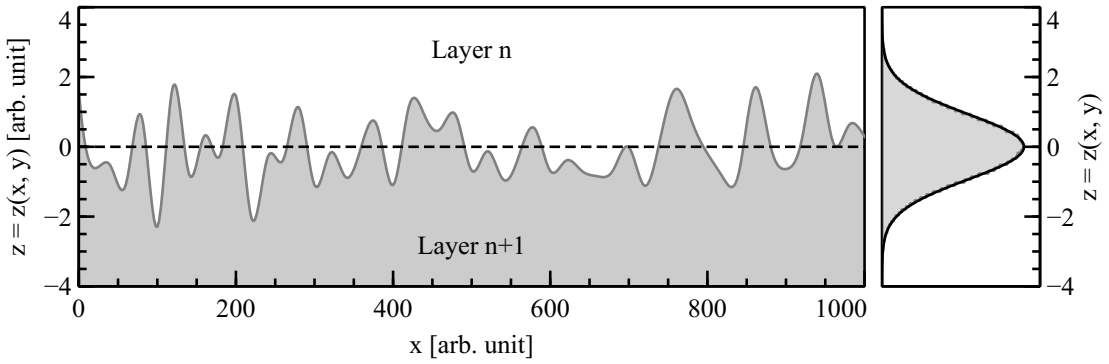

Figure 2.8: Rough interface with height variation $z(x, y)$ around $z = 0$. The right figure shows the histogram of the height variation and its height density $\mathcal{H}$ (red curve).

plying the reflection with q^2 results in

$$\frac{q^2}{4\pi} R(q) = \Delta\rho(1 - e^{-id_1 q}) \sum_{j=1}^{m} e^{ijdq} \tag{2.45a}$$

$$+ (\rho_0 - \rho_1) + \rho_2 e^{imdq}. \tag{2.45b}$$

The second term (2.45b) corresponds to the scattering from the substrate and from the total film thickness md. The first term (2.45a) contains the Bragg peak oscillations. The leading factor $(1 - e^{-id_1 q})$ describes the scattering from the structure of the bilayer, i. e. the scattering inside a bilayer. This factor is responsible for the elimination of Bragg peaks if $d_1 q = 2\pi n$ for a $n \in \mathbb{N}$. The sum in (2.45a) expresses the interference of the m bilayers as a whole and generates all possible Bragg peaks as it is periodic with period $dq = 2\pi n$. Due to the periodicity of both terms, the following condition has to be fulfilled for a Bragg peak at q of order $n \in \mathbb{N}$ to exist

$$q = \frac{2\pi n}{d} \quad \text{and} \quad q \neq \frac{2\pi n}{d_1}. \tag{2.46}$$

These conditions explain the Bragg peaks in figure 2.6: Every second Bragg peak is eliminated, since the bilayer consists of two layers with exactly the same thickness: $d = 100\,\text{Å}$ and $d_1 = d_2 = 50\,\text{Å}$.

2.4.3 Roughness

The surface and interfaces of thin films are not perfectly flat, but exhibit variations, aka roughness, which has to be taken into account in modeling reflectometry experiments. Due to its complexity, a complete and precise description of the geometrical aspect of an interface is typically unknown such that a statistical characterization, like the height distribution or correlation (see [37]) is usually used.

The influence of roughness in specular reflectometry is estimated by averaging the reflectivity $|R(q)|^2$ over the $x-y$ plane using a roughness degraded SLD substitute ρ_{rough}: At an virtual interface, arbitrarily chosen at $z = 0$, the quantity $z(x, y)$ is the height above the interface and $\mathcal{H}$ is its probability density (figure 2.8). The (local) convolution of $\mathcal{H}$ with the original SLD ρ is then used as ρ_{rough} which acts as an averaging.

The main parameter influencing the reflectivity is the root-mean-square (rms) roughness σ which is defined by the variance of the height density $\mathcal{H}$ [38]

$$\sigma^2 = \operatorname{Var} \mathcal{H} = \int_{\mathbb{R}} z^2 \mathcal{H}(z) \mathrm{d}z. \tag{2.47}$$

The roughness dampens the oscillations in the reflectivity. If the height density is assumed to be a normal distribution, the damping factor is called the Névot-Croce factor [39], which is in the BA given by [27]

$$e^{-\sigma^2 q^2/2}. \tag{2.48}$$

This factor resembles the Debye-Waller factor which describes the attenuation of intensity for elastic scattering in crystals by thermal motion [27, 40, 41]. The Névot-Corce factor is also evident when considering equation (2.36) with Gaussian functions $e^{-z^2/2\sigma_j^2}$ as ρ'. As the class of Gaussian functions is invariant under Fourier transforms, the reflection contains oscillations of the form $e^{iqd_j} e^{-\sigma_j^2 q^2/2}$ for each layer j.

2.5 Dynamical Theory

The BA is useful for a qualitative understanding of the reflectivity but fails to be precise enough for a quantitative calculation, especially for wave vector transfers q close to the total reflection edge (figure 2.6). Instead, the exact method to calculate the reflection is the Dynamical Theory. In this chapter, the Abelès matrix formalism [42] in reflectometry will be derived, which is crucial for deriving phase-sensitive PNR.

Another method to calculate the reflection is the Parratt algorithm [43]. This method relates the intensity of the reflected neutrons with the reflection from one layer below, creating a recursive relation. Both methods, the matrix and Parratt algorithm, yield the exact same reflection. However, the matrix method is used more often in practice for the following reasons: Parallelization of the Parratt algorithm is possible, but will likely not yield a speed-up in computation time as each recursion step cannot be computed independently of the previous one. In contrast, the matrix method is merely a multiplication of multiple 2×2 matrices where each matrix corresponds to a layer in the sample. Parallelization is possible [44], but it is usually not done as the time of distributing the work load exceeds the gain of parallelization[4]. One of the major benefits is the possibility to distribute the computation of the reflection for different sample models on a graph-

[4] Multiplication of two 2×2 matrices can be explicitly written out and the overhead of using a dedicated library like basic linear algebra subprograms (BLAS) slows down the computation. But for larger matrices a parallelization can yield a significant gain in computing speed.

ical processing unit (GPU) and simultaneously evaluate them. The recursive nature of the Parratt algorithm is problematic for GPUs as some frameworks (OpenCL[5]) do not support recursion and an efficient pipelining of the calculations cannot be achieved.

2.5.1 Matrix Method

The SLD is approximated by a step function, i. e. piecewise constant function, and each step corresponds to a slab (or layer). As shown in section 2.3.2, the solution of the wave equation (2.15) the superposition of a reflected and transmitted wave in a slab of constant SLD. Thus, the full solution is the sum of each particular solution in its slab:

$$\begin{aligned}\psi(k,x) &= \sum_{j=1}^{N} \psi_j(k,z)\chi_{S_j}(z) \\ &= \sum_{j=1}^{N} \left(r_j(k)e^{ikn(k,z)z} + t_j(k)e^{-ikn(k,z)z} \right) \chi_{S_j}(z)\end{aligned} \tag{2.49}$$

where r_j and t_j are the amplitudes of the reflected and transmitted wave, respectively, and χ_{S_j} denotes the indicator function on the slab S_j. The slabs $S_j = [z_j, z_{j-1})$ with $-\infty = z_N < z_{N-1} < \cdots < z_2 < z_0 < z_{-1} = \infty$ are chosen such that $\rho(z)$ and the refractive index $n(k,z) = \sqrt{1 - 4\pi\rho(z)/k^2}$ are constant for each slab S_j. The indicator function in equation (2.49) assures that only one ψ_j actually contributes to ψ for a specific depth z. The slabs S_j are chosen such that they exactly cover the whole space $\mathbb{R} = \dot{\bigcup}_{j=1}^{N} S_j$ and do not overlap $S_j \cap S_i = \emptyset$ for $i \neq j$. The ordering of the slabs starts with the top slab and ends with the substrate: S_0 corresponds to the air slab and S_N is the substrate slab. Figure 2.9 depicts the slab model.

The general shape of the solution is already known, only the amplitude r_j, t_j of the waves are missing. From a mathematical point of view, these amplitudes have to be appropriately chosen such that ψ is twice continuously differentiable in order for ψ to be a classical solution to the wave equation. This can be achieved by enforcing continuity of ψ and ψ' at the interfaces z_j. The continuity of ψ'' is automatically given by the continuity of ψ. The differentiability condition inside each slab is trivially fulfilled as ψ_j is simply the sum of exponential functions.

The physical reasoning for the continuity of ψ at the interfaces is the conservation of the number of neutrons (for non-absorbing materials) and the conservation of momentum requires the derivative to be continuous $\psi_j'(z_j) = \psi_{j+1}'(z_j)$ as well. These conditions relate the transmission and reflection amplitudes from slab j with the ones from slab $j+1$ and can be expressed in matrix form by

$$\begin{pmatrix} t_j \\ r_j \end{pmatrix} = \frac{1}{2n(z_j)} \begin{pmatrix} p_j e^{-ikm_j z_j} & -m_j e^{ikp_j z_j} \\ -m_j e^{-ikp_j z_j} & p_j e^{ikm_j z_j} \end{pmatrix} \begin{pmatrix} t_{j+1} \\ r_{j+1} \end{pmatrix} \tag{2.50}$$

[5] at least in versions prior 2.0

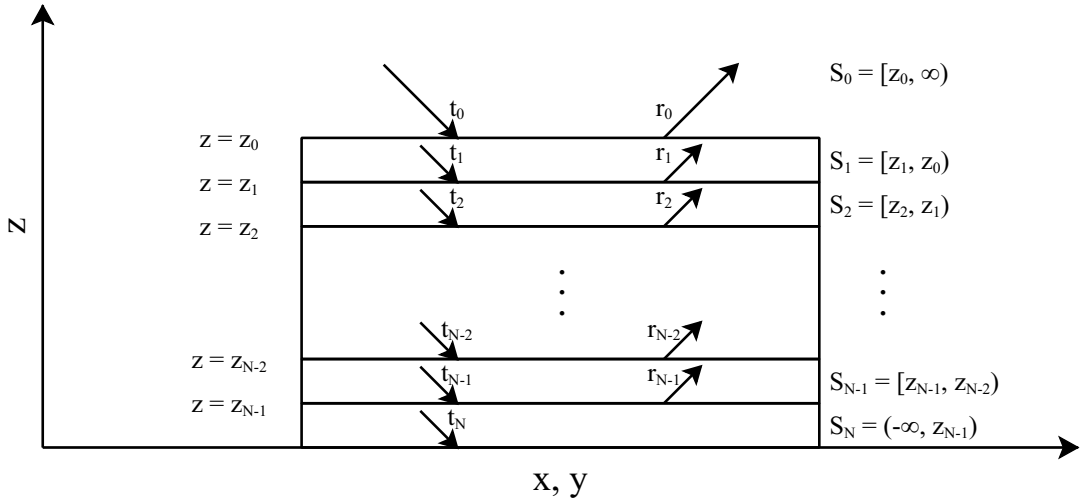

Figure 2.9: Schematic illustration of a slab model. t_j and r_j are the transmission and reflection amplitudes of a plane wave inside slab S_j. The substrate and incident medium correspond to the slab S_N and S_0, respectively.

with

$$m_j \coloneqq n(z_{j+1}) - n(z_j) \quad \text{and} \quad p_j \coloneqq n(z_{j+1}) + n(z_j). \tag{2.51}$$

The matrix (including the prefactor) appearing in equation (2.50) is denoted by T_{j+1} and called the *transfer matrix*. The transfer matrix T_{j+1} transforms the reflection and transmission from slab j to the next slab $j+1$ and successive application of the transfer matrices finally gives

$$\begin{pmatrix} t_0 \\ r_0 \end{pmatrix} = T_1 T_2 \cdots T_N \begin{pmatrix} t_N \\ r_N \end{pmatrix} = \begin{pmatrix} \mathcal{T}_{11} & \mathcal{T}_{12} \\ \mathcal{T}_{21} & \mathcal{T}_{22} \end{pmatrix} \begin{pmatrix} t_N \\ r_N \end{pmatrix}. \tag{2.52}$$

As the substrate is assumed to be infinitely thick, there will be no reflection back from the substrate itself, allowing to set the reflection $r_N = 0$. The reflection R is the ratio of the reflected to the incident amplitude and is calculated by

$$R = \frac{r_0}{t_0} = \frac{\mathcal{T}_{21}}{\mathcal{T}_{11}}. \tag{2.53}$$

To finish this paragraph, some remarks about the transfer matrix T_j and the numerical discretization have to be said which justify the selection of the step-wise approximation of the SLD:

1. Similar as in the BA, the transfer matrix is only sensitive to changes or variations in the SLD, which can be seen in the definition of m_j and p_j: If the SLD does not vary between two slabs, the transfer matrix T_j degenerates to the identity matrix as $m_j = 0$ and $p_j = 2n(z_j)$.

2. A refinement of the slabs, i. e. passing to a finer grid while the SLD approximation stays fixed, does not change the reflection since the additionally introduced transfer matrices are identity matrices. In other words the calculation of the reflection using the matrix method is independent of the selection of the slab grid (but depends on the SLD approximation).

3. The matrix method shown here can be understood as a numerical discretization of a continuous[6] matrix evolution [45]. With finer and finer approximations of the stepwise ρ^c to the exact ρ, the step solution ψ^c converges to the exact solution ψ of the wave equation. Similarly, the reflection computed by the matrix method converges to the exact reflection with finer grids. This will be elaborated in the next section.

2.5.2 Continuous Matrix Method for the Wave Function

Here, we will develop an alternative matrix method relating the wave function inside the sample with the wave function outside the sample, instead of relating the transmission and reflection amplitude inside the sample with the amplitudes outside the sample. The major advantage of the different approach is a "nicer" structure of the transfer matrix, that will later help establishing a relation to retrieve the phase information. In particular it will be shown later, that the unimodularity of the transfer matrix helps to reduce the number of required measurements to two for a phase retrieval [46]. To establish the improved matrix representation, denote the vector consisting of the wave function and its derivative by

$$\Psi(k,z) = \begin{pmatrix} \psi(k,z) \\ k^{-1}\partial_z\psi(k,z) \end{pmatrix}. \tag{2.54}$$

If there exists a transfer matrix $T(k,z)$ which transfers the wave function from outside the sample $z = L$ to some depth z inside the sample, it has to satisfy the following relation of the wave function and its derivative

$$\Psi(k,z) = \mathcal{T}(k,z)\Psi(k,L). \tag{2.55}$$

The transfer matrix is the central object of interest in this approach as it enables to directly compute the wave function. The transfer matrix itself satisfies a linear differential equation of first order. The differential equation stems from the wave equation (2.15) with the usual method of reducing a second order to a first order differential equation:

$$\partial_z\mathcal{T}(k,z) = \begin{pmatrix} 0 & k \\ \frac{4\pi\rho(z)}{k} - k & 0 \end{pmatrix} \mathcal{T}(k,z) \tag{2.56}$$

with the initial condition $\mathcal{T}(k,L) = \mathbb{1}_2$, assuring consistency of equation (2.55). The transfer matrix $\mathcal{T}$ is uniquely determined for each k by the differential equation as long

[6] Continuity in the sense that the transfer matrix depends on the spatial variable z and is continuous in z. It can thus predict the reflection and transmission at any depth z in the sample with arbitrary (non-stepwise) SLD

as ρ' is bounded[7] by the Picard–Lindelöf theorem. Plugging the asymptotic behavior of ψ (see equations (2.22) and (2.23)) into equation (2.55) one can solve for the reflection R. A subsequent rationalizing of the complex denominator (assuming a non-absorptive potential) results in the reflection coefficient being

$$R = e^{-2in_f L}\frac{(n_f^2 n_b^2 \mathcal{T}_{12}^2 + n_f^2 \mathcal{T}_{22}^2) - (n_b^2 \mathcal{T}_{11}^2 + \mathcal{T}_{21}^2) + 2i(n_f n_b^2 \mathcal{T}_{11}\mathcal{T}_{12} + n_f \mathcal{T}_{21}\mathcal{T}_{22})}{(n_f^2 n_b^2 \mathcal{T}_{12}^2 + n_f^2 \mathcal{T}_{22}^2) + (n_b^2 \mathcal{T}_{11}^2 + \mathcal{T}_{21}^2) + 2n_f n_b}, \quad (2.57)$$

where n_f and n_b are the refractive indices of the fronting and backing material, respectively. Notice that the formula stated here differs from the literature [45, 46] because (i) the exponential prefactor expresses a shifted (by $z \to z - L$) sample description and (ii) the time is reversed ($k \to -k$) which results in a change of the sign of the imaginary part (see section 2.3.4). The exponential prefactor vanishes when considering the squared modulus of the reflection as it has unit length and in phase reconstruction it only appears when using a shifted coordinate system. Hence, this prefactor is usually ignored.

The transfer matrix has a multiplicative property [45], similar to the matrix multiplication as in the previous section: Consider an arbitrary cut at $z = z_1 < L$ in the SLD

$$\rho(z) = \begin{cases} \rho_2(z), & z < z_1 \\ \rho_1(z), & z_1 \leq z \end{cases}. \quad (2.58)$$

The transfer matrix $\mathcal{T}_1$ for the fronting ρ_1 transfers the initial wave function to the inside in the film $\Psi(k, L - z_1) = \mathcal{T}_1(k, L - z_1)\Psi(k, L)$ and similarly, the transfer matrix $\mathcal{T}_2$ (with adjusted initial conditions) transfers the wave function deeper $z < z_1$ into the sample $\Psi(k, z) = \mathcal{T}_2(k, z)\Psi(k, L - z_1)$. The resulting wave function can then be expressed as the matrix multiplication of the two transfer matrices $\Psi(k, z) = \mathcal{T}_2(k, z)\mathcal{T}_1(k, L - z_1)\Psi(k, L)$ and because of the uniqueness of the transfer matrix, the multiplicative property follows

$$\mathcal{T}(k, z) = \mathcal{T}_2(k, z)\mathcal{T}_1(k, L - z_1). \quad (2.59)$$

This means that the transfer matrix for the whole film is just the product of transfer matrices of the parts. Neither the concrete shape of $\rho(z)$ nor the position of the cut at z_1 play a role in the deviation, and, consequently, the transfer matrix can be decomposed into a matrix multiplication based on *any* partitioning $\{z_i\}_{i=1}^N$ (with $z_i < z_j$ for $i > j$) of the SLD

$$\mathcal{T}(k, z) = \mathcal{T}_N(k, z)\mathcal{T}_{N-1}(k, z_{N-1} - z_N) \cdots \mathcal{T}_2(k, z_1 - z_2)\mathcal{T}_1(k, L - z_1). \quad (2.60)$$

The multiplicative property of the transfer matrix is of great importance. It can be used to approximate the exact reflection by the reflection of a series of slab profiles, enabling a relatively simple and fast algorithm for computing the reflection. Furthermore, the multiplicative property is the starting point in the deviation of the phase reconstruc-

[7] global Lipschitz-continuity is generally sufficient

tion algorithm, since any sample can be split into known and unknown segments, where each is represented by a transfer matrix.

As previous stated, the unimodularity (determinant is of unity) of the transfer matrix will help to reduce the required measurements for a phase retrieval. The unimodularity of the transfer matrix is an intrinsic property of the continuous transfer matrix itself and is not a property of a discrete representation.

Lemma 2. *Let $\mathcal{T}(k,z)$ be the solution of the transfer matrix evolution equation* (2.56) *with initial condition $\mathcal{T}(k,L) = \mathbb{1}_2$. Then the determinant of $\mathcal{T}(k,z)$ is independent of z and, in particular,* $\det \mathcal{T}(k,z) = 1$ *for all z.*

Proof. The statement of the lemma easily follows by taking a look at the derivative of the determinant

$$\partial_z \det \mathcal{T}(k,z) = \mathcal{T}_{11}'\mathcal{T}_{22} + \mathcal{T}_{11}\mathcal{T}_{22}' - (\mathcal{T}_{12}'\mathcal{T}_{21} + \mathcal{T}_{12}\mathcal{T}_{21}').$$

As the transfer matrix satisfies equation (2.56), it follows (suppressing the dependence of k and z for easier reading)

$$\partial_z \det \mathcal{T} = k\mathcal{T}_{21}\mathcal{T}_{22} + \left(\frac{4\pi\rho}{k} - k\right)\mathcal{T}_{11}\mathcal{T}_{12} - \left[k\mathcal{T}_{22}\mathcal{T}_{21} + \left(\frac{4\pi\rho}{k} - k\right)\mathcal{T}_{12}\mathcal{T}_{11}\right] = 0.$$

Thus the determinant of $\mathcal{T}$ is independent of z and the initial condition guarantees the unimodularity. □

2.5.2.1 Transfer Matrix for Step Profiles

An analytic expression for the transfer matrix is in general not possible. The transfer matrix is just a reformulation of the wave equation, and an analytic expression of the transfer matrix is equivalent to solve the wave equation for arbitrary scattering potentials. However, with a step function approximation of the SLD the transfer matrix can be exactly computed. To start, let the SLD be of the following step-like form

$$\rho(z) = \sum_{j=1}^{N} \rho_j \chi_{S_j}(z) \tag{2.61}$$

where $S_j = [z_j, z_{j-1})$ is again the interval of the slab j. The solution of the wave equation with a constant SLD is of exponential form (see section 2.3.2) and with the initial conditions, it follows that the transfer matrix of the j-th slab is

$$\mathcal{T}_j(k,z) = \begin{pmatrix} \cos kn_j z & n_j^{-1}\sin kn_j z \\ -n_j \sin kn_j z & \cos kn_j z \end{pmatrix} \quad \text{with} \quad n_j = \sqrt{1 - 4\pi\rho_j/k^2}, \tag{2.62}$$

where ρ_j is the SLD of the j-th slab. Again, notice that solving the "evolution" equation (2.56) for the transfer matrix is equivalent to solving the wave equation with the given constant SLD. Now, the complete transfer matrix is just by the multiplicative

property (2.60) the multiplication of the transfer matrices of each slab representation, and consequently, the full transfer matrix takes the form

$$\mathcal{T} = \prod_{j=N}^{1} \begin{pmatrix} \cos kn_j d_j & n_j^{-1} \sin kn_j d_j \\ -n_j \sin kn_j d_j & \cos kn_j d_j \end{pmatrix}, \tag{2.63}$$

where $d_j = z_{j-1} - z_j$ is the thickness of the j-th slab.

Notice that the order of multiplication has changed compared to equation (2.52). Here, the transfer matrix moves the wave function deeper into the sample (from the surface to the substrate), whereas the matrix method of section 2.5.1 moves the wave function in the opposite direction, i. e. a multiplication from the left corresponds to moving the wave function towards the samples surface.

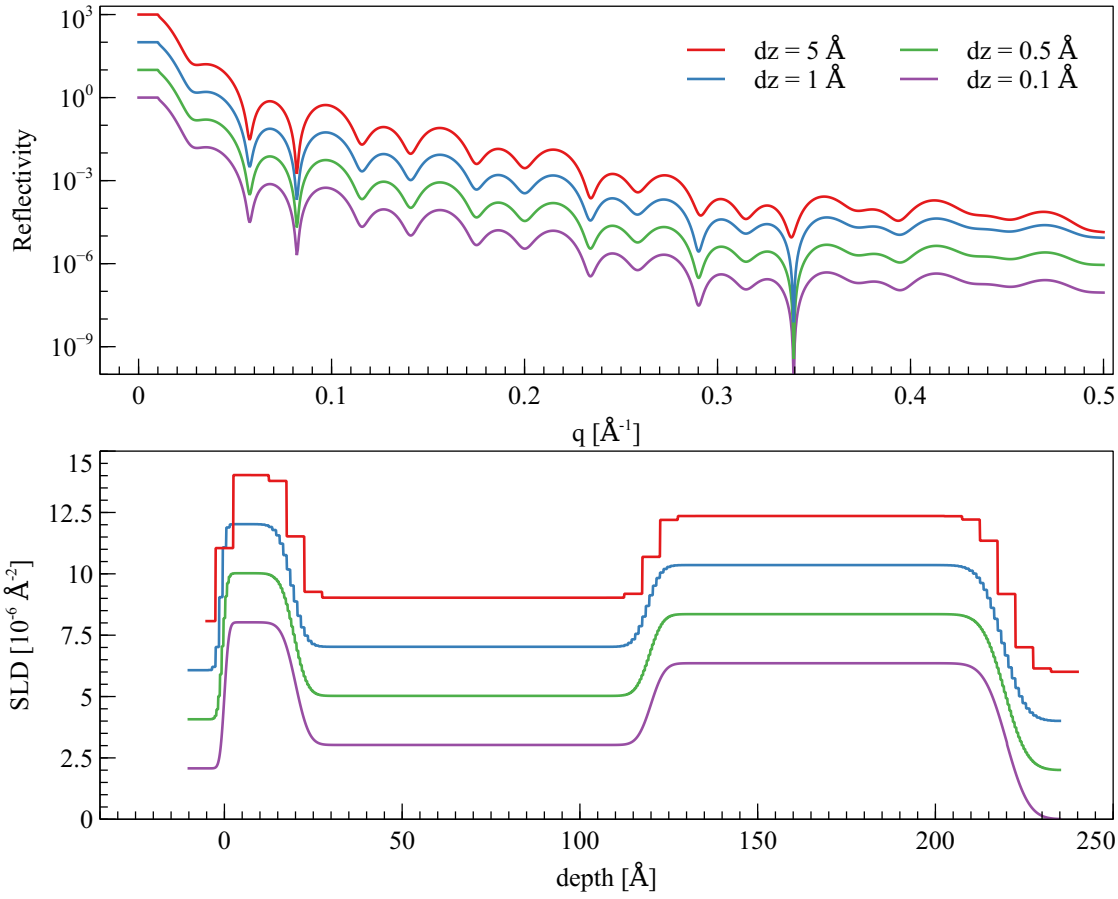

Figure 2.10: Influence of the discretization step size dz of the step profile approximation on the calculated reflectivity. The upper graph shows the reflectivities calculated by the step profile shown below. The reflectivities are shifted by one order of magnitude and the SLDs are vertically shifted by two units for reasons of clarity.

The step profile can be interpreted as a numerical approximation of the continuous profile. In the limit of finer discretizations of the step profile, the approximated transfer matrix converges to the continuous transfer matrix. The reflection can thus be approximated in equation (2.57) by replacing the continuous transfer matrix with the step-like approximation.

Figure 2.10 shows simulated reflectivities with various discretization step sizes. The SLD was generated from a Si/Fe(100 Å)/Cr(100 Å)/Pt(100 Å)/Air sample with step sizes $\mathrm{d}z = 5\,\text{Å}$, $1\,\text{Å}$, $0.5\,\text{Å}$ and $0.1\,\text{Å}$. Even the very coarse 5 Å grid yields good results compared with the finest grid $\mathrm{d}z = 0.1\,\text{Å}$. Only at the dips at $q = 0.34\,\text{Å}^{-1}$ and around $q = 0.5\,\text{Å}^{-1}$, a slight deviation can be observed. An even finer discretization than $\mathrm{d}z = 0.1\,\text{Å}$ does not yield any observable difference in the reflectivity. A reasonable choice of the discretization size is between 0.1 Å to 1 Å as atomic lattice constant are in the order of a few angstroms and the depth resolution is of comparative magnitude for PNR experiments.

2.5.2.2 Reversing the Sample

The continuous transfer matrix exhibits another remarkable property if the sample is reversed in space, i. e. $\rho(z) \to \rho(L - z)$. Namely, the diagonal entries of the transfer matrix are just interchanged while the off-diagonal entries are not affected [45].

In fact, this property can easily be proven by using the decomposition of the transfer matrix into multiple step transfer matrices. The reversed transfer matrix $\mathcal{T}^{\text{rev}}$ is simply the reversed matrix multiplication of the individual step transfer matrices

$$\mathcal{T} = \prod_{j=N}^{1} \mathcal{T}_j \quad \xleftrightarrow[\text{order}]{\text{inversion of}} \quad \mathcal{T}^{\text{rev}} = \prod_{j=1}^{N} \mathcal{T}_j. \tag{2.64}$$

The matrix multiplication is in general not commutative $\mathcal{T} \neq \mathcal{T}^{\text{rev}}$ but a switching of the diagonals can recover the equality. To prove that, first the notion of an interchanged matrix is required.

Definition 1 (Interchange of diagonal entries)**.** *Let $A \in \mathbb{R}^{2\times 2}$ be any matrix. The* interchanged *matrix $\overleftrightarrow{A}$ is the matrix with interchanged diagonal entries, i. e.*

$$A = \begin{pmatrix} a_{11} & a_{12} \\ a_{21} & a_{22} \end{pmatrix} \Rightarrow \overleftrightarrow{A} = \begin{pmatrix} a_{22} & a_{12} \\ a_{21} & a_{11} \end{pmatrix}. \tag{2.65}$$

The following lemma is the crucial feature of a transfer matrix to show the connection of $\mathcal{T}^{\text{rev}}$ with $\mathcal{T}$. It states that an inversion of order of a matrix multiplication of transfer matrices acts like an interchange of diagonal entries and vice versa.

Lemma 3. *Let $A, B \in \mathbb{R}^{2\times 2}$ be transfer matrices of the form in equation* (2.62)*. Then it follows that*

$$\overleftrightarrow{A \cdot B} = \overleftrightarrow{B} \cdot \overleftrightarrow{A} = B \cdot A.$$

Furthermore, for the product of $N \in \mathbb{N}$ transfer matrices $\mathcal{T}_j$, $j = 1, \dots, N$ it holds that

$$\overleftarrow{\prod_{j=1}^{N}} \mathcal{T}_j = \prod_{j=N}^{1} \mathcal{T}_j.$$

Proof. The claim follows from a simple computation of the matrix multiplication, while observing that any transfer matrix is invariant under interchanging diagonal entries, i. e. $\overleftrightarrow{A} = A$ or equivalently $a_{11} = a_{22}$. Then it follows that

$$\begin{aligned}
\overleftarrow{A \cdot B} &= \overleftarrow{\begin{pmatrix} a_{11} & a_{12} \\ a_{21} & a_{22} \end{pmatrix} \cdot \begin{pmatrix} b_{11} & b_{12} \\ b_{21} & b_{22} \end{pmatrix}} = \overleftarrow{\begin{pmatrix} a_{11}b_{11} + a_{12}b_{21} & a_{11}b_{12} + a_{12}b_{22} \\ a_{21}b_{11} + a_{22}b_{21} & a_{21}b_{12} + a_{22}b_{22} \end{pmatrix}} \\
&= \begin{pmatrix} a_{21}b_{12} + a_{22}b_{22} & a_{11}b_{12} + a_{12}b_{22} \\ a_{21}b_{11} + a_{22}b_{21} & a_{11}b_{11} + a_{12}b_{21} \end{pmatrix} = \begin{pmatrix} a_{21}b_{12} + a_{11}b_{11} & a_{11}b_{12} + a_{12}b_{22} \\ a_{21}b_{11} + a_{22}b_{21} & a_{22}b_{22} + a_{12}b_{21} \end{pmatrix} \\
&= B \cdot A = \overleftrightarrow{B} \cdot \overleftrightarrow{A},
\end{aligned}$$

where the equation with the star follows from $a_{11} = a_{22}$ and $b_{11} = b_{22}$.

The second claim follows by induction over N. In fact, the base case is shown above and the induction step is trivial. □

Now, by applying Lemma 3 on $\mathcal{T} = \prod_{j=N}^{1} \mathcal{T}_j$ and identifying $\mathcal{T}^{\text{rev}}$ with $\rho(L - z)$ one has the following corollary.

Corollary 1. *By reversing the sample, i. e. $\rho(z) \to \rho(L - z)$, only the diagonal entries of the corresponding transfer matrix are interchanged. It holds that*

$$\overleftrightarrow{\mathcal{T}^{rev}} = \mathcal{T}.$$

2.5.2.3 Extension of the Reflection

The theory established so far for the reflection and transmission coefficients only holds for $k \neq 0$. The case $k = 0$ is special as it does not describe a scattering of a neutron on a thin film. However, one can still continuously extend the reflection R and transmission T at $k = 0$ and the asymptotic behavior of the solution ψ changes its meaning.

Here, a vague argumentation of $R(0) = -1$ and $T(0) = 0$ is given. A rigorous proof, relying on a modified scattering matrix, can be found in [33]. The transfer matrix (see equation (2.63)) representation of a constant SLD is used for a single slab. A single transfer matrix, and thus the product of all matrices asymptotically behave as

$$\mathcal{T} \sim \begin{pmatrix} 1 & -ik \\ ik^{-1} & 1 \end{pmatrix} \quad \text{as} \quad k \to 0 \tag{2.66}$$

since $n(k) \sim ik^{-1}$, if all the involving constants are ignored as they do not change the limit and only make the deviation more tedious. Plugging the asymptotic transfer matrix into the reflection (2.57) with air as a fronting material ($n_f = 1$) yields the following

asymptotics

$$R(k) \sim \frac{1 + k^{-2} - 2k^{-1}}{1 - k^{-2} + 2ik^{-1}} \sim \frac{-1 + k}{1 + k^2} + \frac{-k + k^2}{1 + k^2} i \quad \text{as} \quad k \to 0. \tag{2.67}$$

It is now easy to see that $R(k) \to -1$, $\operatorname{Im} R(k) \to 0^-$ and similarly $T(k) \to 0$ as $k \to 0$. Notice that these limits are all independent of the sample. The asymptotic solutions behave now as $\psi \sim 0$ as $z \to \pm\infty$, meaning, that no scattering has occurred.

Alternatively, the limit of R can be shown by using the Fresnel formula [47]

$$R = \frac{\cos\theta_i - n\cos\theta_t}{\cos\theta_i + n\cos\theta_t} \to \frac{1 - n}{1 + n} \tag{2.68}$$

in the limit $\theta_i, \theta_t \to 0$.

3 Data Analysis Techniques for Reflectometry

Reflectometry measurements are traditionally analyzed by setting up a physical model and optimizing the parameters of the model such that a specified objective function[1] is minimized. This approach heavily depends on the selection of the physical model. Furthermore, the optimized parameters are usually not unique, in the sense that there might exist a different set of parameters which describes the reflectometry data equally well. Finally, as there does not exist an algorithm for finding a *global*[2] minimum for non-linear objective functions, and as the search space usually exhibits multiple local minima, the final solution depends on the initial guess of the researcher and the amount of computing time allocated for the algorithm to search for an optimum.

In contrast, a model-free approach by using the phase of the reflection determines the SLD of the sample uniquely [33], assuming that bound states (see section 3.2.1) do not exist. This method does not rely on any minimization algorithm to search for a minimum point nor does it require any *a priori* knowledge of the sample. Instead the data analysis is straightforward as shown in section 3.2 and section 3.3. However, the retrieval of the phase information is not trivial and requires significant effort. Furthermore the degradation of real PNR data by various effects like resolution, background or measurement noise has to be considered (section 3.4).

3.1 Data Fitting

In data fitting, the goal is to find a set of parameters Θ, which best describes the measured system. In the context of reflectometry, the measured system is the reflectivity[3] $R^2(q)$ as a function of wave vector transfer q. The physical model is constructed as a slab system (or layer system) of which each layer has a defined thickness and density (or more generally the SLD if the chemical composition is not precisely known). At each interface of two layers, a roughness or interdiffusion parameter can additionally be applied. The substrate and the incident media (typically air) of the sample are modeled with a semi-infinite thickness. The vector Θ contains all these information and it is the central object of interest.

[1] referred to as *cost* function, figure-of-merrit or goodness-of-fit

[2] Algorithms for finding local optimal points do exist, but usually do not guarantee a global minimum; only if additional constraints on the objective function or search space are given, e. g. strict convexity of the objective function.

[3] By abuse of notation, the reflectivity is denoted as R^2 instead of the correct $|R|^2$ to simplify the following formulas

The description of the system by means of the parameter vector Θ is quantitatively evaluated by an objective function f. The relation between the optimal parameter vector Θ and the objective function is

$$\Theta = \arg\min_{\theta} f(\theta), \tag{3.1}$$

where the objective function f measures the residuals of the theoretical model $\mathscr{R}^2$ to the measured reflectivity $(q_i, R^2(q_i))$. The choice of the objective function strongly influences the optimal Θ vector.

The objective function f is interpreted as a metric and should satisfy the following conditions in reflectometry experiments [48]:

1. f has a unique global minimum
2. f has few local minima and these local minima should be much higher compared to the global minimum
3. f is easy and fast to calculate
4. f is sensitive on a locale scale, but not on a global scale

The points (1) and (2) are self-explanatory: Multiple global minima do not yield a unique optimal parameter Θ and local minima can be hard to deal with by some optimization algorithms, e. g. Gauss-Newton method or gradient descent as they tend to be stuck at local minima. A detailed discussion is given in section 3.1.3. Point (3) guarantees a fast evaluation and thus allows a fast convergence to a minimum. The last condition makes the objective function more sensitive to changes in the relative magnitude, which is appropriate as reflectometry data spans multiple orders of magnitude.

A common choice for the objective function is the mean squared weighted error (MSWE)

$$\epsilon(\Theta) = \frac{1}{N} \sum_{i=1}^{N} \left(\frac{R^2(q_i) - \mathscr{R}^2[q_i; \Theta]}{\sigma_i} \right)^2, \tag{3.2}$$

where $\mathscr{R}^2$ is the theoretical model function, computing the reflectivity given the wave vector transfer q_i and the physical model parameter vector Θ, and σ_i being the measurement uncertainty of the reflectivity.

However, analyzing reflectivity data using MSWE with constant σ_i (i. e. ignoring measurement uncertainty) is less suited, since the reflectivity decays with $R^2(q) \sim 1/q^4$ or faster (see equation (2.37)), thus the MSWE is more sensitive to reflectivities at lower q values and pays less attention to reflectivities at higher q values, which violates point (4) of the list above. In practice the measurement uncertainty behaves as $\sigma_i \sim \frac{1}{q^2}$ and the MSWE decays as $\epsilon \sim \frac{1}{q^4}$. Hence, the sensitivity of the objective function is still not in good accordance with point (4).

If all measurements are equally likely (σ_i is constant), alternative objective functions which are more suited for the decay of the reflectivity is the mean squared logarithmic

Table 3.1: Fitted parameters corresponding to the fits shown in figure 3.1 of a Si/Pt/Fe/Au/air sample using different objective functions. The column "expectation" shows the nominal values of the thicknesses and the densities of the bulk material.

Layer	Parameter	MSWE	$\mathrm{MSE}_{\mathrm{sqrt}}$	$\mathrm{MSE}_{\log}$	expectation
Au	thickness [Å]	106	107	107	100
	density [g/cm^3]	19.00	19.10	19.02	19.32
	roughness [Å]	5.3	5.1	4.8	-
Fe	thickness [Å]	50	50	49	50
	density [g/cm^3]	7.94	8.00	8.25	7.87
	roughness [Å]	4.2	5.1	3.8	-
Pt	thickness [Å]	103	102	102	100
	density [g/cm^3]	21.02	20.84	21.60	21.45
	roughness [Å]	2.0	2.7	3.2	-
Si (Sub)	density [g/cm^3]	2.47	2.19	2.19	2.34
	roughness [Å]	6.4	3.1	3.9	-

error ($\mathrm{MSE}_{\log}$) defined as

$$\epsilon(\Theta) = \frac{1}{N}\sum_{i=1}^{N}\left|\log R^2(q_i) - \log \mathscr{R}^2[q_i;\Theta]\right|^2, \tag{3.3}$$

and the mean squared root error ($\mathrm{MSE}_{\mathrm{sqrt}}$) defined as

$$\epsilon(\Theta) = \frac{1}{N}\sum_{i=1}^{N}\left|\sqrt{R^2(q_i)} - \sqrt{\mathscr{R}^2[q_i;\Theta]}\right|^2. \tag{3.4}$$

These objective functions ($\mathrm{MSE}_{\log}$ and $\mathrm{MSE}_{\mathrm{sqrt}}$) weight residuals for high q stronger than MSWE, satisfying point (4) of the list above.

To illustrate the influence of the objective functions on the optimal parameter a Si/Pt/Fe/Au thin film was analyzed with x-ray reflectometry. Figure 3.1 compares the optimal fits of the corresponding objective function MSWE, the $\mathrm{MSE}_{\mathrm{sqrt}}$ and $\mathrm{MSE}_{\log}$. As it can be seen, the worst fit by eye is achieved when using the MSWE objective function with constant σ_i, and the best fit is obtained with the $\mathrm{MSE}_{\log}$ objective function. The MSWE is least sensitive to the residuals for high q less into account and thus the fitting algorithm fails to select parameters which improve the resemblance of the fit and the data in this region. In comparison, $\mathrm{MSE}_{\log}$ is asymptotically $\sim |\log q|^2$ for $q \to \infty$ and thus weights the residual for high q stronger than MSWE. The resulting fitted parameters are shown in table 3.1. The thickness is consistent for the three objective functions, however, the roughness of the interface and density can vary by up to $\approx 200\%$ (roughness of the Si substrate in table 3.1) and $\approx 10\%$, respectively.

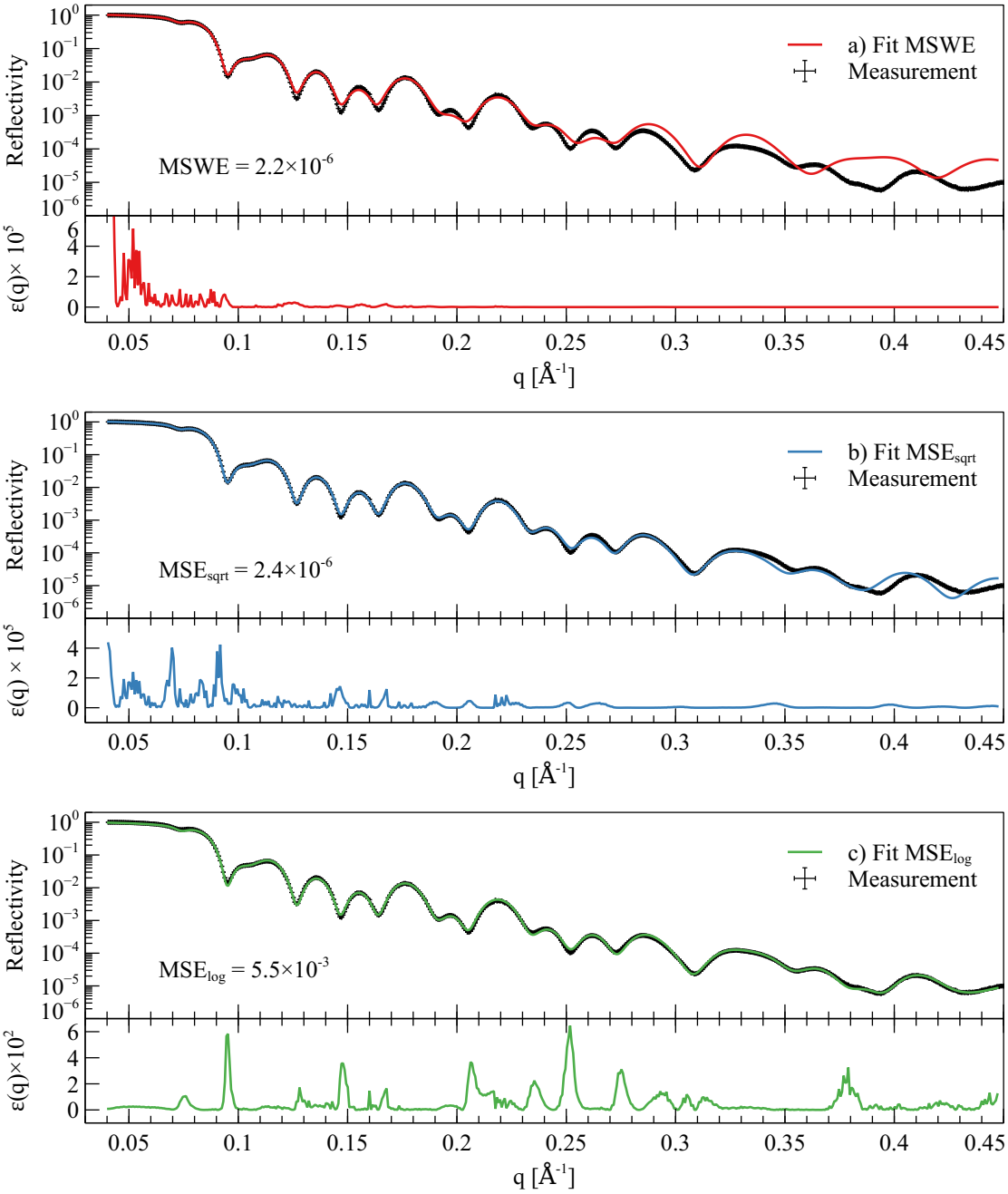

Figure 3.1: Comparison of optimal fits to the same x-ray reflectivity measurement of a Si/Pt(100 Å)/Fe(50 Å)/Au(100 Å)/air sample using different objective functions obtained from the software GenX [49]. For each group of graphs, the upper graph depicts the optimal fit with the objective function being a) MSWE with constant σ_i b) MSE_{sqrt} and c) MSE_{log}. The lower graph shows the individual contributions to the objective function $\varepsilon(q)$, i. e. the addend in the sum definition of the objective function.

3.1.1 Bayesian Analysis

The method mentioned above of minimizing the MSWE yields an optimal parameter vector Θ but reveals no information of the statistical properties of Θ, e. g. the credible interval, variance and correlation among components. Furthermore, *a priori* knowledge, e. g. about the thickness of a specific layer from previous experiments (not necessarily from PNR), are not expressed in equations (3.2) and (3.3).

To deal with these peculiarities, the notion of probability has to be interpreted differently. Here, the probability is interpreted in the Bayesian point of view and it has to be differentiated from the (classical) Frequentist interpretation. The Bayesian interpretation expresses the probability as the belief or reasonable expectation of knowledge. In the Frequentist interpretation, however, probability is the relative frequency of an event happening in the limit of many trials. In the Frequentist interpretation, it is not possible to assign a probability to an unobserved parameter Θ as the parameters are considered fixed in the first place before experiments are performed [50].

In the Bayesian interpretation, every parameter has an associated probability density function (PDF), which is based on the *a priori* knowledge, thus called the *prior* distribution. If no specific information of a parameter Θ is known but the bounds $a \leq \Theta \leq b$, the prior PDF can be set as a uniform distribution $p_{\mathcal{U}(a,b)}(x) = \frac{1}{b-a}\chi_{[a,b]}(x)$. However, if a parameter Θ was measured before in the form of $\Theta = \mu \pm \sigma$, a suitable prior is a normal distribution $\mathcal{N}(\mu, \sigma^2)$ with the density function $p(x) = \frac{1}{\sqrt{2\pi\sigma^2}} \exp\left(-\frac{1}{2}\frac{(x-\mu)^2}{\sigma^2}\right)$ [51].

Choosing an adequate prior helps finding a more reliable estimate of the true parameter. Besides this, the prior will not influence the estimate of the parameter in the limit of infinitely many experiments. Thus, the prior can be viewed as a better initial guess of the true parameter and its error bounds.

The credible interval of an unobserved parameter Θ is the interval such that Θ is located therein with a particular probability. In other words, it expresses the probability of finding the parameter between the lower and upper bounds. Similar to uncertainties in measurements, the credible interval is a measure indicating how sensitive and accurate the unobserved parameter was inferred from the data.

To calculate the credible interval, the PDF of Θ given the measured data has to be known, referred to as *posterior* PDF. It can be calculated with Bayes Theorem for probability density functions

$$p(\Theta \mid R^2, I) = \frac{p(R^2 \mid \Theta, I)p(\Theta \mid I)}{p(R^2 \mid I)}. \tag{3.5}$$

The left hand side is the *posterior* PDF which is the PDF of the parameters Θ given the measured reflectivities R^2, i. e. the likelihood of the parameters to describe the measured reflectivity. The variable I denotes the *a priori* knowledge of the experimenter, e. g. contextual information of the measurement device, previous measurements, and other experiences. It expresses the fact that the probability depends on the knowledge of the experimenter as well and is usually left out in the formula. Again, the notion

of probability in the Bayesian point of view expresses the degree of reasonable likeliness or plausibility.

The terms on the right hand side of equation (3.5) are

1. $p(R^2 \mid \Theta, I)$ which is the *likelihood* function, expressing how likely the measured reflectivity R^2 is under the assumption that the physical parameters are Θ;

2. $p(\Theta \mid I)$ which is the *prior* function, expressing the *a priori* belief of the parameters Θ;

3. $p(R^2 \mid I)$ that is a normalization constant. It expresses the belief of measuring the reflectivity R^2.

From a more intuitive point of view, Bayes Theorem simply states how the belief of a parameter should be updated (posterior probability) after a measurement (likelihood probability) has been conducted and how previous measurements (prior probability) influence the new belief. For example, repeated measurements of the same sample with x-rays and neutrons can be used to make the parameter estimation more precise.

The most likely parameter is assumed to be a good estimate to the true parameter of the system. That maximum likelihood estimator (MLE) is defined as

$$\hat{\Theta}_{\mathrm{MLE}} = \arg\max_{\Theta} p(\Theta \mid R^2, I) = \arg\max_{\Theta} p(R^2 \mid \Theta, I) p(\Theta \mid I), \tag{3.6}$$

where the normalization constant $p(R^2 \mid I)$ is irrelevant for estimating the MLE as it only scales the posterior by a positive constant, independently of Θ.

The probability of counting $n \in \mathbb{N}$ reflected neutrons in a fixed time interval with a known intensity $\lambda = \mathrm{Int}(q)$ is modeled by the discrete Poisson distribution $\mathrm{Pois}_{\mathrm{Int}(q)}(n)$ with the PDF

$$\mathrm{Pois}_{\lambda}(n) = \frac{\lambda^n e^{-\lambda}}{n!}. \tag{3.7}$$

It is well known that the Poisson distribution can be approximated by the normal distribution with $\mu = \mathrm{Int}(q)$ and $\sigma^2 = \mathrm{Int}(q)$ if the intensity is sufficiently large[4]. After dividing the reflected intensity $\mathrm{Int}(q)$ by the incident intensity I_0, the likelihood function for the reflectivity at a single q_i is given by

$$p(R^2(q_i) \mid \Theta, I) = \frac{1}{\sqrt{2\pi \mathscr{R}^2(q_i;\Theta)}} \exp\left(-\frac{1}{2} \frac{\left(R^2(q_i) - \mathscr{R}^2(q_i;\Theta)\right)^2}{\mathscr{R}^2(q_i;\Theta)} \right). \tag{3.8}$$

[4]Intensities larger than 100 counts are usually sufficient for the normal distribution to be a good approximation to the Poisson distribution.

Assuming that the reflectivity measurement at different q_i are independent, the likelihood function of R^2 is simply the product of all likelihood functions of R_i^2

$$\begin{aligned} p(R^2 \mid \Theta, I) &= \prod_{i=1}^{N} p(R^2(q_i) \mid \Theta, I) \sim e^{-\frac{1}{2}\chi^2} \quad \text{with} \\ \chi^2 &= \sum_{i=1}^{N} \frac{(R^2(q_i) - \mathscr{R}^2(q_i;\Theta))^2}{\mathscr{R}^2(q_i;\Theta)}. \end{aligned} \tag{3.9}$$

The notation here for χ^2 expresses the fact that the quantity χ^2 converges to a chi-squared distribution if the reflectivities are normally distributed, i. e. the error is normally distributed. If this is the case, χ^2 is chi-squared distributed with $(N - d - 1)$ degrees of freedom where d is the number of independent population parameters [52]. Thus, to evaluate the goodness-of-fit the reduced chi-squared quantity $\chi^2_{\text{red}} = \frac{1}{N-d-1}\chi^2$ is considered, in order for the expectation value to be $\mathrm{E}[\chi^2_{\text{red}}] = 1$. In general, if $\chi^2_{\text{red}} > 1$ either the model does not capture the data (the model is insufficient) or the errors are underestimated. On the other hand, if $\chi^2_{\text{red}} < 1$ the model is overfitting the data or the errors are overestimated [53].

Taking the logarithm of a function does not change the location at which the maximum is attained, and because of the duality[5] of maxima and minima, the MLE is

$$\begin{aligned} \hat{\Theta}_{\text{MLE}} &= \arg\max_{\Theta} e^{-\frac{1}{2}\chi^2(R^2;\Theta)} p(\Theta \mid I) \\ &= \arg\min_{\Theta} \frac{1}{2}\chi^2(R^2;\Theta) - \log p(\Theta \mid I). \end{aligned} \tag{3.10}$$

The Bayesian approach thus justifies the selection of the MSWE as an objective function for data fitting: If the prior distribution is merely a uniform distribution (no prior knowledge available) and the errors in measuring the data is approximately normally distributed, the MLE is the minimum of χ^2 and is a minimizer of MSWE.

3.1.2 Estimation of Parameter Uncertainty

This allows the uncertainty in the parameter Θ to be estimated as the posterior distribution together with the MLE are in principle possible to compute. For a fixed $\gamma \in (0, 1)$ the $\gamma \cdot 100\%$-credible interval $[a, b]$ of a parameter Θ is defined by $a, b \in \mathbb{R}$ that fulfill [54]

$$P(\Theta \in [a, b] \mid R^2) = \int_a^b p(\Theta \mid R^2, I)\mathrm{d}\Theta = \gamma. \tag{3.11}$$

The definition states that the unobserved parameter Θ lies in the $\gamma{\cdot}100\%$-credible interval with a probability of γ. Note that this definition is crucially different from the confidence interval. Contrarily, the confidence interval is defined such that if the experiment is arbitrarily often repeated then the unobserved parameter lies in the confidence interval

[5] meaning $\arg\max_x f(x) = \arg\min_x -f(x)$

in $\gamma \cdot 100\%$ of all trials. The subtle difference is that the Bayesian approach treats the bounds of the credible interval fixed and the estimated parameter as a random variable. On the contrary, the Frequentist approach treats the bounds as random variables and the parameter as fixed. The Bayesian approach answers the question "What is the probability of Θ being located in the credible interval given the data?" whereas the Frequentist approach answers the question "How often does the confidence interval given the data contain the true parameter Θ?". In specific cases the credible interval and confidence interval coincide, but in general they do not [55].

The difficulty of calculating the credible interval is the high-dimensionality of the integration space. Each layer in the sample adds three additional fitting parameters to the theoretical model and twenty or more parameters are not uncommon for fitting reflectivity data. The integral in equation (3.11) cannot be given in closed form and hence a numerical quadrature of the integral has to be used. Numerical integration schemes like Newton-Cotes [56] with equally spaced evaluation grid-points or the Gaussian quadrature are useful for lower dimensional integrals [57]. Higher dimensional integrals can be reduced to repeated integration of one-dimensional integrals by Fubini's theorem, but the number of function evaluations grows exponentially with the dimension which renders this approach unpractical.

To overcome the problem of high dimensional integrals, a randomized approach using Markov Chains can be used. Instead of evaluating the integrand on a uniform or pre-defined grid, e. g. the zeros of orthogonal polynomials for Gaussian quadrature, the integrand is evaluated at random grid-points such that the grid is more dense where the integrand has larger contribution to the overall integral [58].

A common algorithm for computing the grid points, i. e. sampling from a PDF, and the integral, i. e. the expectation value, is the Metropolis-Hastings (MH) algorithm; the markov chain monte carlo (MCMC) method. Its idea is to generate candidates which will be accepted with probability α given by [59]

$$\alpha = \min\left\{\frac{p(\Theta_{\text{new candidate}} \mid R^2)}{p(\Theta_{\text{old candidate}} \mid R^2)}, 1\right\}. \tag{3.12}$$

Hence, if the new candidate has a higher probability density than the previous sample, it will always be accepted whereas a candidate with a lower probability density might be rejected. The distribution of accepted candidates will converge in the limit to the desired probability distribution.

The advantage of dealing with the *ratio* of the PDF is that normalization constants of the PDF can be ignored, i. e. the PDF does not need to be a proper probability density[6] but can be any arbitrary non-negative function whose integral exists and is finite. The lack of needing the normalization constant is especially advantageous in light of Bayes Theorem (see equation (3.5)) as the denominator, which is another high dimensional integral, can be neglected.

[6] the integral of the density does not need to be equal to one

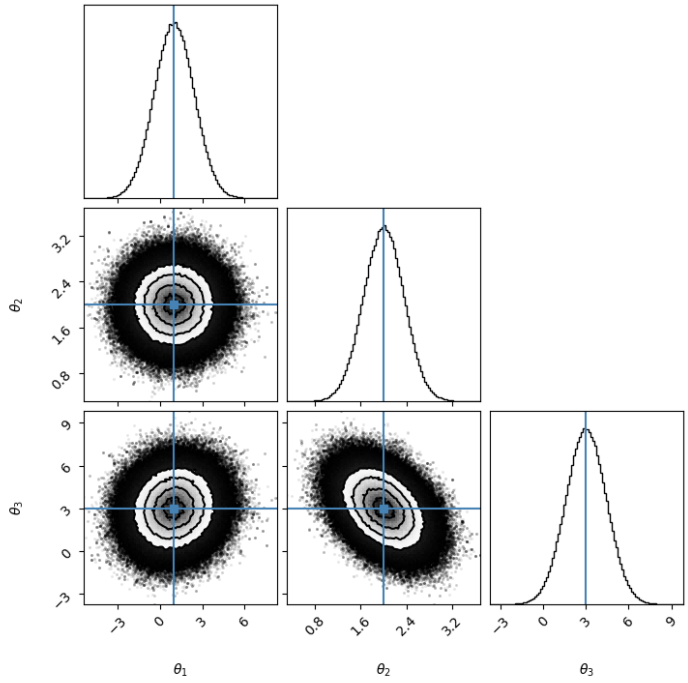

Figure 3.2: Visualization of a three-dimensional normal distribution $\theta \sim \mathcal{N}_3(\mu, \Sigma)$ with mean $\mu = (1, 2, 3)^\mathsf{T}$, variances $\sigma^2 = (2, 0.125, 2)^\mathsf{T}$ and covariances $\sigma_{13} = 0.2$, $\sigma_{23} = -0.2$. The covariance matrix Σ is completely determined by σ_{ij}. The diagonal graphs show the one-dimensional projection of the marginal distribution θ_i. The graphs at row i and column j depict the two-dimensional projection of the joint probability distribution $\theta_{i,j}$ which reveals covariances. The blue lines correspond to the true mean value μ of the projections. Plotting is performed with the corner library [60].

Having an independent and identically distributed sample $(X_n)_{n=1}^N$ drawn from a PDF $p(x)$, the law of large numbers guarantees that

$$\frac{1}{N}\sum_{n=1}^{N} f(X_n) \to \int_{\mathbb{R}^d} f(x)p(x)\mathrm{d}x = E[f(X)] \quad \text{as} \quad N \to \infty. \tag{3.13}$$

By taking Bayes Theorem, one can now estimate the integral of the credible interval with the help of MCMC

$$\int p(\Theta \mid R^2, I)\mathrm{d}\Theta = \int p(R^2 \mid \Theta, I)\frac{p(\Theta \mid I)}{p(R^2 \mid I)}\mathrm{d}\Theta \approx \frac{1}{N}\sum_{n=1}^{N} p(R^2 \mid \Theta_n, I), \tag{3.14}$$

where Θ_n is a sample drawn from the distribution $p(\Theta \mid I)$, ignoring the denominator $p(R^2 \mid I)$ as it is only a scaling factor, and the MH sampler is invariant under scaling the PDF.

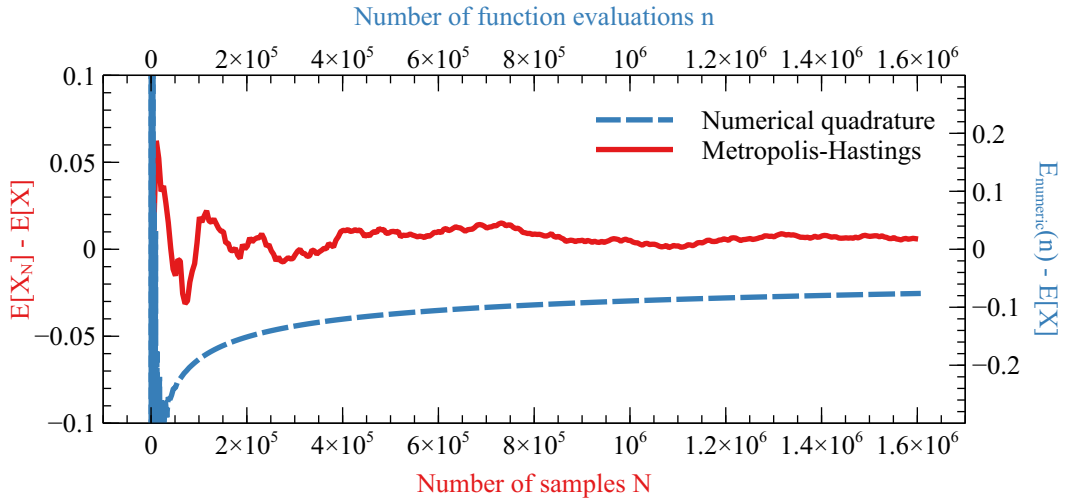

Figure 3.3: Evolution of the computed expectation value $E[X_N]$ as a function of number of samples N and $E_{\text{numeric}}(n)$ as a function of function evaluations of the PDF. The expectation value $E[X_N]$ is calculated using the MH algorithm, whereas E_{numeric} is computed using the trapezoidal integration rule. The expectation value is computed with respect to the marginal distribution of the third component of figure 3.2.

An example consisting of 1.6×10^6 samples drawn from a three-dimensional normal distribution is shown in figure 3.2. The one-dimensional marginal distributions (integration along all the remaining axes) of the sample show a good match to a one-dimensional normal distribution and the two-dimensional contour plot shows no obvious discrepancy from the exact two-dimensional normal distribution. The samples have been drawn using the software library emcee [61] and visualized with the library corner [60].

Figure 3.3 compares the integral approximation of equation (3.13) with a traditional trapezoidal integration scheme. The samples from figure 3.2 were used to approximate the expectation value of the sampling distribution itself, i. e. $E[X]$ with $X \sim \mathcal{N}(3, 2)$ and taking $f(x) = x$. The trapezoidal integration was implemented by a successive integration over $[-10, 10]^3$. The discretization step size was fixed but arbitrary in each integration. Notice that taking a grid with $n = 10$ points requires n^3 function evaluations in the numerical scheme.

3.1.3 Choice of Optimization Algorithms

In the Bayesian approach with normally distributed measurement uncertainty, the optimal model description is obtained by the MLE given in equation (3.10). An analytical solution to the non-linear minimization problem is not possible to find, thus a minimization algorithm has to be utilized.

Traditional (deterministic) minimization algorithms like the gradient descent, Gauss-Newton method or Levenberg–Marquardt guarantee a fast convergence [56, 62, 63] to a minimum under suitable prerequisites, e. g. convexity of the objective function. However,

no assurance can be given whether the minimum is local or global. Furthermore, the current candidates of these algorithms tend to run into local minima (even with different initial conditions) and cannot evade from this point.

To escape from a local minima, a step in a non-optimal direction (in the sense of the derivative) has to be taken which is not allowed for gradient based minimization algorithms. A Monte-Carlo algorithm randomly selects directions, and some of the new directions might improve the objective function as the algorithm steps across a hill. Examples of such algorithms are the differential evolution (DE) and the simulated annealing algorithm. These algorithms are heuristic which means that there is no mathematical proof for finding a global optimum or even terminate after a finite number of steps. However, these algorithms are particularly useful when dealing with high-dimensional problems with many local minima. Especially for fitting the reflectivity data, which typically exhibits a lot of local minima, heuristic algorithms proved to perform better than the classical algorithms.

An example of an ill-behaved objective function for reflectivity data is depicted in figure 3.4. It shows the evolution of the objective function by ($\mathrm{MSE}_{\log}$ was used) varying a single parameter and fixing all the others. The global optimum is clearly visible, but the objective function reveals multiple local optima when projecting on a single parameter. Especially for deterministic algorithms, the local minima close to the global minimum is highly problematic as even a good initial guess does not necessarily result in a convergence to the global minimum.

Differential Evolution

In the following the DE, and genetic algorithms in general are discussed. A thorough discussion can be found in [64–66].

Algorithm 1 (Differential Evolution)**.** *Let $X_0 \subset \mathbb{R}^d$ be the initial population consisting of $N \in \mathbb{N}, N \geq 4$ candidate solutions and let f be the objective function which should be minimized. Denote by X_G the current population of generation G. The next population X_{G+1} is calculated in the following four steps for each parameter $x \in X_G$:*

1. *Mutation: A mutated parameter is calculated. Select randomly three pairwise distinct parameters $x_1, x_2, x_3 \in X_G$ from the current generation. The mutation is achieved by adding a weighted difference $F > 0$ of x_1 with x_2 to the third one x_3:*

$$x_{mutated} = x_3 + F(x_1 - x_2). \tag{3.15}$$

2. *Update: A trial parameter x_{trial} is constructed. The old parameter x is taken and its components x_i are randomly updated by $x_{mutated,i}$ with the* crossover *probability $CR \in [0, 1]$. At least one component (e. g. the d-th one) must be updated:*

$$x_{trial,i} = \begin{cases} x_{mutated,i}, & \text{with probability } CR \text{ or } i = d \\ x_i, & \text{otherwise} \end{cases} \tag{3.16}$$

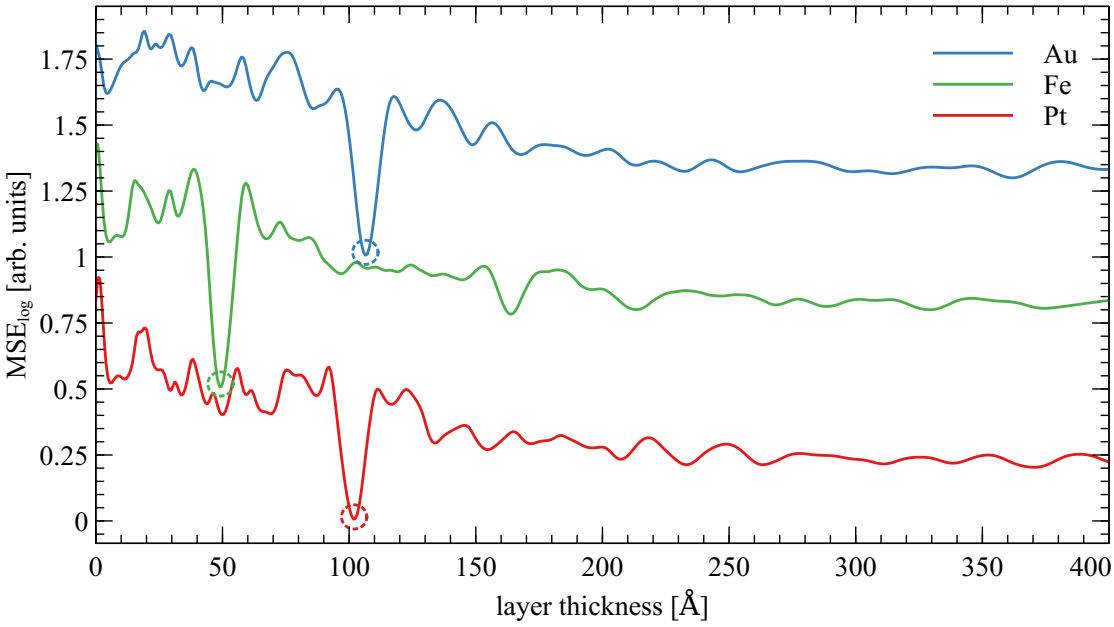

Figure 3.4: Evolution of the MSE_{log} objective function by fixing all parameters except one. The varying parameter is the thickness of a) Au b) Fe (shifted by 0.5) and c) Pt (shifted by 1.0) while the remaining parameters stay fixed. The scanning of the layer thickness parameter is performed in the (global) optimum with the same model and data shown in figure 3.1c). The (global) optimum is at $d_{Au} \approx 100\,Å$, $d_{Fe} \approx 50\,Å$ and $d_{Pt} \approx 100\,Å$ (circles).

3. *Selection: The current generation X_G will be updated. If the trial parameter x_{trial} improves the objective function, then it will be added to X_{G+1} otherwise the old parameter x will be kept:*

$$X_{G+1} \leftarrow \begin{cases} x_{trial}, & f(x_{trial}) < f(x) \\ x, & f(x) \leq f(x_{trial}). \end{cases} \tag{3.17}$$

4. *Repeat: Repeat the process until a fixed number of iterations is reached or the objective function attained a certain threshold.*

The main virtue of the DE algorithm are the simplicity and usability. It can easily be parallelized and intuitively one expects the algorithm to find a solution. In the third step, the generation will be updated only if the new candidate improves the objective function. The randomization in the second step and the generation of new candidates in the first step should explore the search space sufficiently well. Still, as DE is a heuristic algorithm, there is no guarantee that a global minimum is ever found. Nonetheless, the reflectivity fitting software GenX uses DE as the minimization algorithm [49], which proved to be a robust algorithm.

The selection of the initial condition and the parameters N, F and CR is still subject to research [66]. However, there are some rules of thumbs one can use to achieve a reasonable result as the selection influences the convergence and the candidate solution of the DE algorithm:

As an initial population a uniform distribution in the search space can be taken. If a guess x_0 of the minimizer of the objective function is known, the initial population can be sampled from a normal distribution centered at x_0, too. The spread of the sampling distribution, however, should encompass the possible global minimum.

The selection of the parameters N, F, CR is not straightforward and they can also be optimized with respect to the objective function. Nonetheless, using $F \in (0, 1)$ (e. g. $F = 0.2$), $0 \leq CR \leq 0.2$ and $N = 30$ are good guesses in most cases [66].

Another reflectivity fitting software *Refl1D* uses a combination of the DE and the MH algorithm [67–69], referred to as differential evolution adaptive metropolis (DREAM) [70]. The algorithm is capable of searching for a global minimizer of the objective function while at the same time drawing samples from the posterior PDF. The objective function and the posterior PDF are the same functions in this case. The major advantage is, that not only a minimum is searched, but at the same time a statistical analysis is performed.

3.1.4 Application: Pt/Fe/Au Thin Film

To see the statistical analysis using the DE and MH algorithm in action, a thin film of Pt(100 Å)/Fe(50 Å)/Au(100 Å) was grown by DC magnetron sputtering in an ultrahigh vacuum chamber [71, 72] on a $2 \times 2\,\mathrm{cm}^2$ Si substrate at a base pressure of 1.5×10^{-7} mbar. After completion of the deposition, the reflectivity of the sample was measured *ex situ*

on a two-circle x-ray diffractometer (D5000, Siemens GmbH) with parallel beam optics and $Cu_{K\alpha}$ ($\lambda = 1.5419\,\text{Å}$) source in a θ-2θ scattering geometry.

The sample is modeled by a composition of $Si/SiO_2/SiPt/Pt/Fe/Au/air$ which includes a natural oxidized Si layer and a PtSi interdiffusion layer. Other sample models by adding interdiffusion layers like PtFe or FeAu did not result in any improvement in the objective function MSWE or resulted in unreasonable densities larger than $25\,\text{g/cm}^3$. There is no *a priori* knowledge taken into account and the objective function is the usual chi-squared or MSWE.

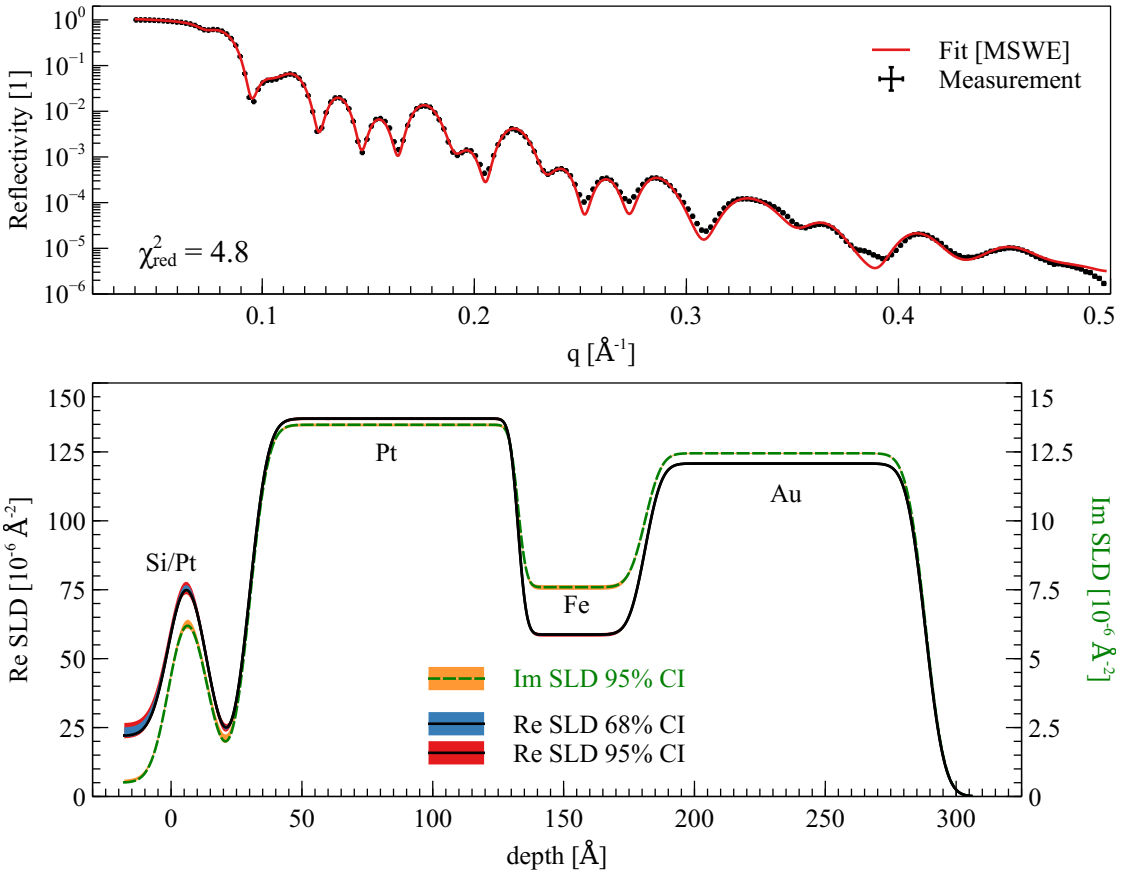

Figure 3.5: The top graph depicts the measurement of the Si/Pt/Fe/Au/air sample (see figure 3.1) and the best fit obtained by the fitting software *Refl1D* [68]. The bottom graph shows the SLD used for the fitting. It is noted that the absorptive (imaginary) part of the SLD is one order of magnitude smaller than the real part. The colored regions correspond the 68% or 95% credible interval of the SLD.

Figure 3.5 shows the best fit to the measured reflectivity (top) and in the bottom graph the best SLD together with 68% and 95% credible intervals (shaded area) is shown. The reflectivity is well fitted, but at larger q-values some mismatches are visible due to the decay of MSWE (see section 3.1). The best fit of the SLD is shown as the

Table 3.2: Maximum likelihood parameters obtained from the fitted model. The uncertainties describe the 68% credible interval which corresponds to the $1-\sigma$ uncertainty if the parameter is normally distributed.

Layer	thickness d [Å]	density ρ [g/cm^3]	(rms) roughness σ [Å]
Au	107.1 ± 0.1	18.70 ± 0.03	5.7 ± 0.1
Fe	48.6 ± 0.1	7.78 ± 0.06	5.0 ± 0.1
Pt	102.8 ± 0.1	21.39 ± 0.04	2.6 ± 0.1
PtSi	13.0 ± 0.7	15.23 ± 1.00	7.0 ± 0.5
SiO_2	16.8 ± 0.3	0.50 ± 0.32	5.7 ± 0.1
Si	∞	2.56 ± 0.36	5.8 ± 0.2

black solid (real part) and green dashed (imaginary part) line. The imaginary part of the SLD is approximately one order of magnitude smaller than the real part. The credible intervals display possible variations of the SLD based on a slab model which express the uncertainty in the best fit and which should ideally be narrow. The credible intervals are hardly distinguishable at depths above 25 Å, however, at the substrate or the SiPt interdiffusion layer they are visible. The uncertainties in the retrieved parameters are unusual low with the exception of the bottom layers (Si, SiO_2 and PtSi), see table 3.2, which explains the small credible intervals in the top layers.

Parameters in reflectivity models are usually substantially correlated. A corner plot shows the correlation between these parameters. The correlation in the case of the Si/Pt/Fe/Au sample is shown in figure 3.6. Each sector in the corner plot shows the correlation of two variables. The correlation is estimated by sampling from the posterior PDF using the DREAM algorithm. The range of the horizontal and vertical axis of each sector are selected by the minimal and maximal occurrence of the corresponding parameters from the drawn samples.

For example, the red box in figure 3.6 shows the correlation between the parameters σ_{Au} and σ_{Pt}. A correlation can be understood as a functional dependence of the parameters and in this example a negative linear correlation is visible which means that a smaller roughness in the Au interface is compensated in the fit by a higher roughness in the Pt interface. The distinct high intensity point reveals a low uncertainty (or variance) of both roughnesses.

A negative linear correlation is common for the thickness of layers, for example d_{Au} and d_{Fe} (green box) or $d_{\mathrm{SiO_2}}$ and d_{PtSi} show this behavior. The reason for the negative correlation is the fact that the total film thickness can reliably be estimated from the data. Thus, if the thickness d_i of layer i increases, the thickness d_j of layer j decreases in order for the sum $d_i + d_j$ to stay constant.

The blue boxes in figure 3.6 show the correlations of ρ_{Si} with all other parameters. It reveals that ρ_{Si} is uncorrelated with the other parameters as varying the density of Si has virtually no influence on the other parameters. This leads to a high uncertainty in ρ_{Si} (see table 3.2). For highly correlated parameters, the determination of the true

parameter becomes less accurate. The correlation plot is thus crucial to understand the accuracy of the inferred parameters.

Figure 3.7 shows the histogram of the sampled parameters. The histogram is used to derive credible intervals of the individual parameters. It also shows the modality of the marginalized distribution from which for example one can determine whether the normal distribution is a suitable approximation of the marginalized distribution. This is important when specifying the uncertainty of a parameter as the $1-\sigma$ uncertainty should only be used when the normal distribution can approximate the marginalized distribution of the parameters. Otherwise, the credible interval is more accurate. For example, the marginalized parameters $\rho_{SiO_2}, \rho_{Si}, I_{bkgrd}$ and resolution cannot be approximated by a normal distribution, as shown in figure 3.7.

For evaluating the convergence of the DREAM algorithm, a history plot of the log likelihood function can be used, see figure 3.8. At the start of the algorithm, the negative log likelihood function should decrease[7] until it reaches a minimum. The algorithm then explores the likelihood around the minimum. A linear fit of the likelihood function with respect to the drawn samples should ideally show a slope of zero, indicating a convergence of the DREAM algorithm. A non-zero slope suggests that the algorithm is still searching for an optimum and has not yet explored the search space sufficiently well.

Furthermore, to ensure that the DREAM algorithm has sufficiently well explored the likelihood function, a trace plot of the individual parameters can be examined. A trace plot depicts the evolution of the Markov chains with respect to a single parameter. A well explored parameter space should have an erratic behavior of the Markov chains as shown in the inset in figure 3.8. In addition, the Markov chains should be well mixed in the sense that the individual traces cross each other, in order to fully explore the parameter space.

[7] The maximum of the likelihood function is attained at the minimum of the negative log likelihood function

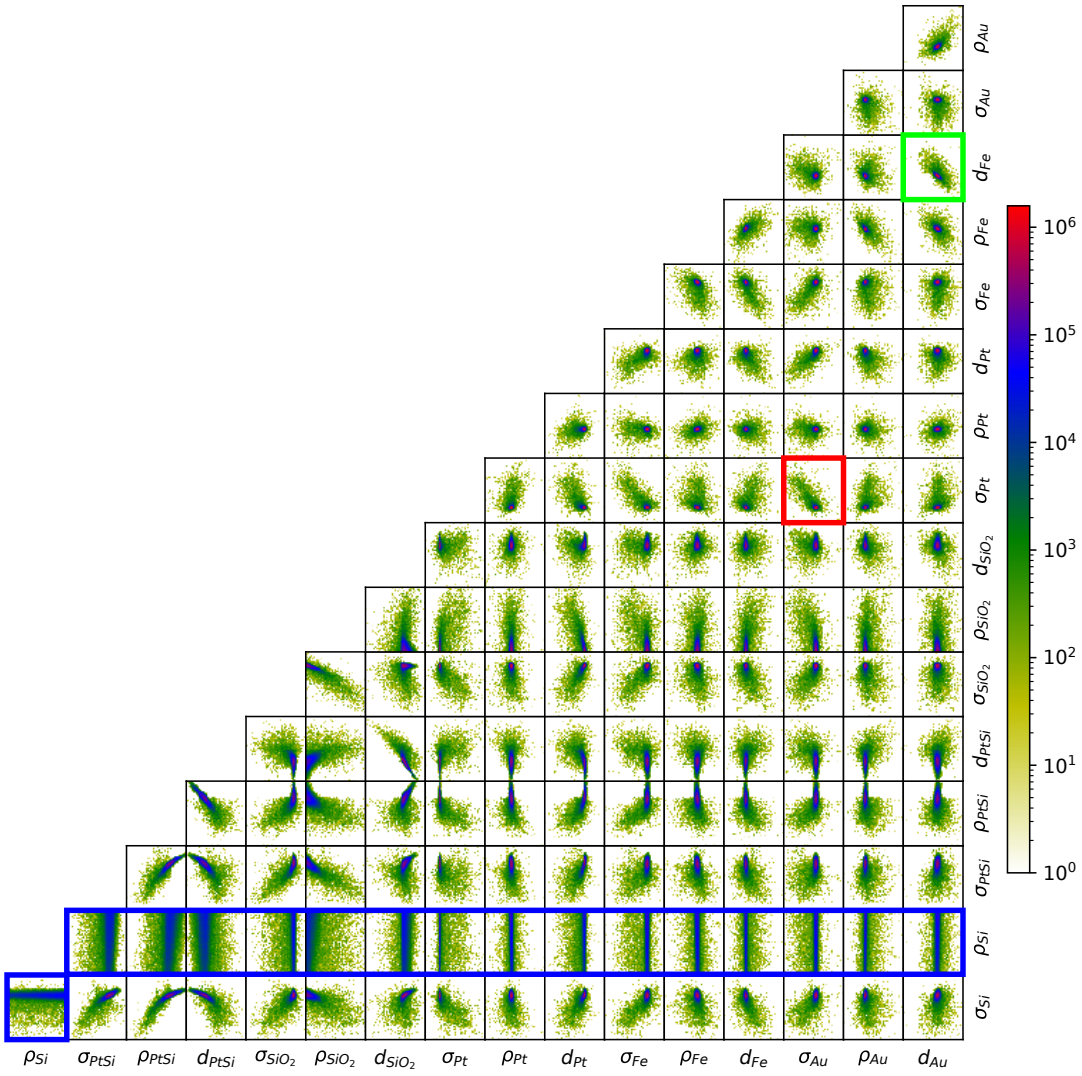

Figure 3.6: Correlation or "corner" plot of the fitted parameters (I_0, I_{bkgrd}, resolution are excluded for clarity). The color bar depicts the intensity of the two-dimensional projection of the drawn samples. The red box shows the correlation of σ_{Au} with σ_{Pt}, the green box shows d_{Au} with d_{Fe} and the blue boxes show the correlations of ρ_{Si} with all other parameters.

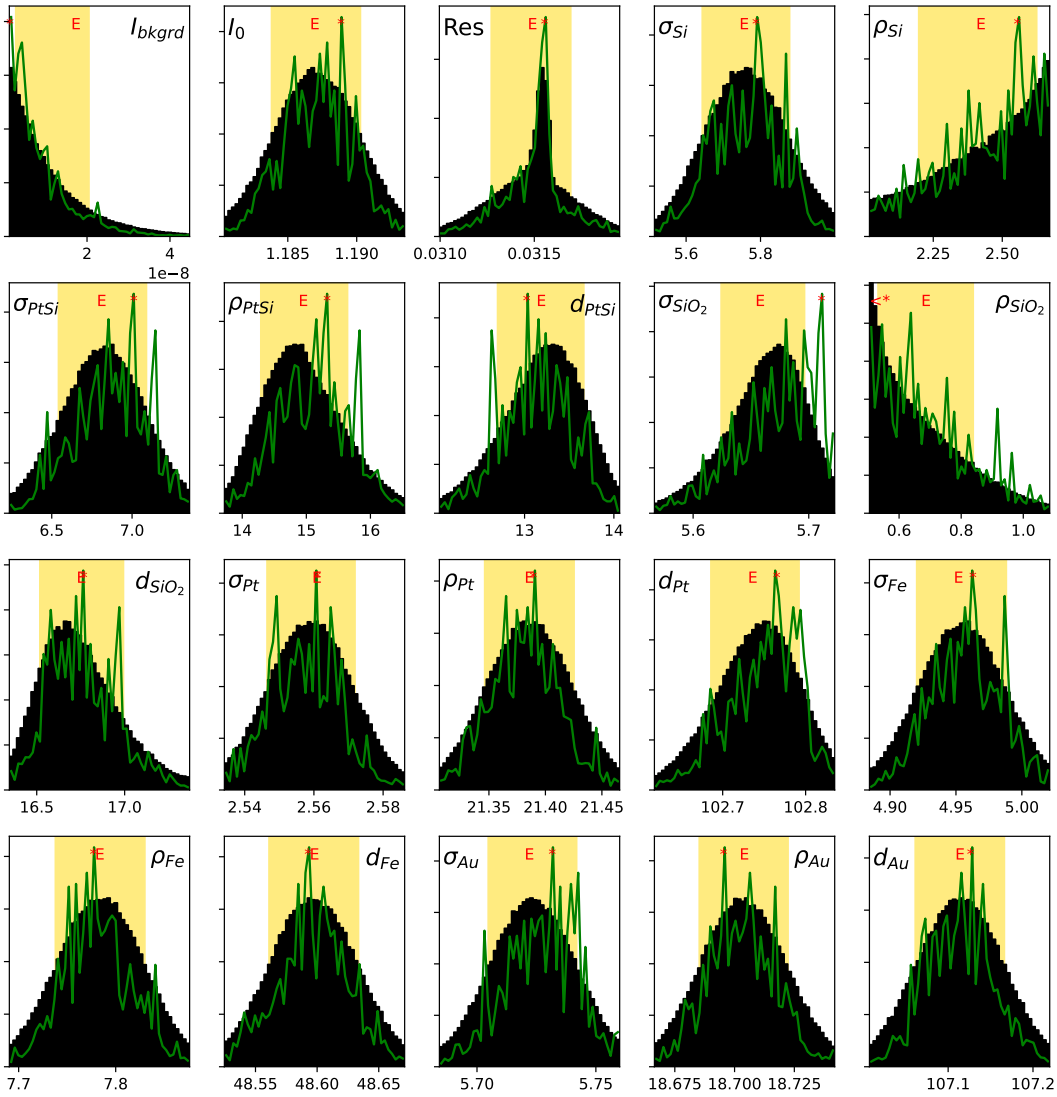

Figure 3.7: Histograms of the projected parameters. The range of the abscissa is the 95% credible interval and the yellow shaded area corresponds to the 68% credible interval. The red "E" and "∗" show the expectation value and the best fit of the marginalized parameter, respectively. The green curve shows the logarithmic maximum likelihood estimator of the marginalized parameter. The variable ρ denotes the density in g/cm^3, σ is the roughness/interdiffusion in Å and d denotes the layer thickness in Å. I_0 is the scaling of the intensity and I_{bkgrd} the background signal. The parameter "Res" is an additive factor for the angular divergence (given as FWHM in degree) for fitting the q resolution.

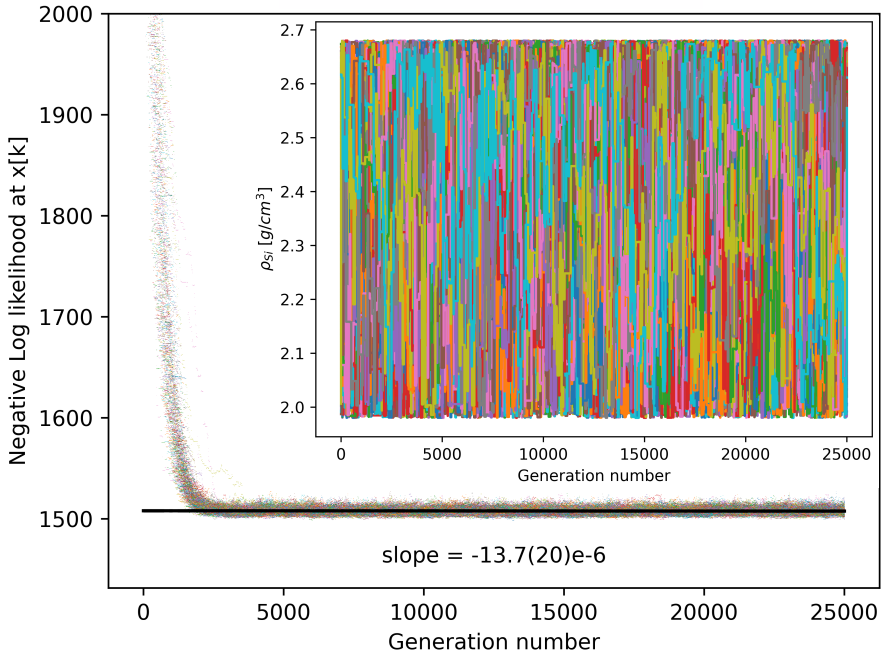

Figure 3.8: Convergence plot of the DREAM algorithm. The abscissa shows the generation number as in the DE algorithm. The ordinate is the negative log likelihood which is minimized. The black curve is a linear fit of the negative log likelihood distribution at the drawn samples. The inset depicts the traces of all populations of the DREAM algorithm of the Si substrate density. A mixing of the traces indicate a good sampling from the posterior distribution.

3.2 Inversion of the Reflection

In this section the theory of inverse scattering in one dimension is briefly presented. The theory asserts the existence of the inverse operator $\mathcal{R}^{-1}$ which computes the scattering potential V from a given reflection function R and the bound states information. An explicit algorithm for computing the inverse scattering potential is given by the Gel'fand-Levitan-Marchenko (GLM) method.

3.2.1 Bound States

In general the reflection R alone is not sufficient to uniquely determine the scattering potential due to bound states. Informally speaking, a bound state represents the situation whenever the wave function of a neutron is contained in a bounded region of space. That means the neutron cannot "escape" from the scattering potential and the neutron is bound to the scattering potential. This state is in a sense the opposite of a scattering state when the neutron is either transmitted or reflected.

To understand why a bound state is relevant in scattering theory, one has to consider the spectral theorem. It states that a special class of operators, i. e. self-adjoint bounded linear operators, can be expressed based on its eigenvalues and eigenvectors [73]. In scattering theory the linear operator is the Hamiltonian $H = V - \partial_z^2$. All positive $k^2 > 0$ are eigenvalues of the Hamiltonian and the corresponding eigenfunctions are exactly the solutions of the wave equation (2.15)

$$H\psi = k^2\psi, \tag{3.18}$$

which are linked to the reflection R and transmission T coefficient by equation (2.22) and equation (2.23).

If a negative eigenvalue $-\beta^2, \beta > 0$ of the Hamiltonian H exists, the corresponding eigenfunction $\psi(z, i\beta)$ is called a *bound state* of H [31, 33, 74] which satisfies

$$H(z)\psi(z, i\beta) = -\beta^2\psi(z, i\beta). \tag{3.19}$$

These negative eigenvalues differ substantially from the positive eigenvalues as only finitely many (and thus isolated) bound states can exist [31]. Every bound state with energy $-\beta^2$ is closely correlated with the transmission coefficient T. As a matter of fact, every bound state corresponds to a simple pole in T at $k = i\beta$ with residuum (normalization constant) [33]

$$\operatorname{res}_{k=i\beta} T(k) = i\left(\int_{-\infty}^{\infty} \psi_{i\beta}^{+}(z)\psi_{i\beta}^{-}(z)\right)^{-1} \sim i\left\|\psi_{i\beta}^{+}\right\|_{L^2}^{-2}, \tag{3.20}$$

where $\psi_k^{\pm}$ are the solutions of equation (2.30), i. e. the wave equation solutions.

The modulus of the transmission $|T|$ is determined by R using the conservation of probability equation (2.34). By applying tools from complex analysis [33] it is possible to construct the phase of T from the reflection R, without the simple poles of T. Hence,

not only the position of the poles $k = i\beta_j$, or equivalently the energy $-\beta^2$, but also the residuum $\operatorname{res}_{k=i\beta_j} T$ is required to fully determine the transmission T from the reflection R.

Both, the energy $-\beta^2$ and residuum, depend on the scattering potential and cannot be determined beforehand. In particular, one can construct scattering potentials V which have a bound state with any energy $\beta > 0$ and any normalization constant c. For a given scattering potential V one can construct a new potential V^* with bound state β^* and normalization constant $c^* = \frac{2\beta^*}{\alpha} T(i\beta^*)$ with any $\alpha > 0$ by the Darboux-transformation [31]

$$V^*(z) = V(z) - 2\frac{\mathrm{d}^2}{\mathrm{d}z^2} \log g_\alpha(z), \tag{3.21}$$

where $g_\alpha(z) = \psi^+_{i\beta^*}(z) + \alpha\psi^-_{i\beta^*}(z)$. The reflection R^* and transmission T^* of the new potential V^* are

$$\begin{aligned} R^*(k) &= -\frac{k + i\beta^*}{k - i\beta^*} R(k), \\ T^*(k) &= \frac{k + i\beta^*}{k - i\beta^*} T(k). \end{aligned} \tag{3.22}$$

Similarly, a bound state β^* can be removed from a scattering potential by reversing the procedure, i. e. by setting

$$V(z) = V^*(z) - 2\frac{\mathrm{d}^2}{\mathrm{d}z^2} \log \psi^{+*}_{i\beta^*}(z). \tag{3.23}$$

Thus, it is desirable that the scattering potential has no bound states such that the reflection R determines both the transmission T and, hence, the scattering potential V uniquely [31, 75]. A simple, but useful condition for excluding bound states in neutron reflectometry is the requirement $V > 0$ [76], or more generally $\int V \mathrm{d}z > 0$ [77].

Bound states cannot exist if elements with a negative scattering length are excluded. In neutron scattering, most of the elements have a positive scattering length and only a few are the exception such as H, Li, Ti, V and Mn in their natural abundance, as well as some specific isotopes like B^{10}, Ca^{43} and Cr^{50} and a few more [78]. Hence, if these elements or isotopes are completely excluded, bound states cannot exist. This strict requirement, however, might be hard to realize in practice, especially for the isotopes. Alternatively, if the sample does not contain a significant concentration of these exceptional elements or isotopes such that $V > 0$, bound states are already excluded.

3.2.2 Uniqueness and Inversion

The uniqueness of the reflection is the main reason for phase-sensitive neutron reflectometry. It guarantees that the gain in the phase information is sufficient (modulo bound states) to recover the scattering potential uniquely. In section 3.3.1 it will be shown that one can easily construct differing scattering potentials with the same reflectivity.

Theorem 1 (Uniqueness [31, 79]). *The scattering potential $V \in L^1$ with finite first absolute moment $\int |zV(z)|\mathrm{d}z = \|zV(z)\|_{L^1} < \infty$ is uniquely determined by its reflection coefficient R, bound states $-\beta_n^2 < \ldots < -\beta_1^2$ and normalization constants $c_j = \|\psi^+_{i\beta_j}\|^2_{L^2}$.*

In particular, if there are no bound states, the scattering potential V is uniquely determined by the reflection R.

The proof of the uniqueness for bound states can be reduced to the case with no bound states by removing them as described in section 3.2.1. The proof for no bound states is rather technical and can be found in [79].

The uniqueness is an important key to phase-sensitive reflectometry, however, an explicit computational method for determining the associated scattering potential to a given reflection is crucial as well. The GLM integral equation enables the scattering potential to be directly calculated.

Algorithm 2 (Gel'fand-Levitan-Marchenko Method [80, 81]). *Let R be the reflection coefficient with bound states $-\beta_n^2 < \ldots < -\beta_1^2$ and normalization constants $c_j = \|\psi^+_{i\beta_j}\|^2_{L^2}$. Compute the Fourier transform of the reflection*

$$\hat{g}(z) = \frac{1}{\pi}\int_{-\infty}^{\infty} R(k)e^{2ikz}\mathrm{d}k \tag{3.24}$$

and set

$$g(z) = \hat{g}(z) + 2\sum_{j=1}^{n} c_j e^{-2\beta_j z}. \tag{3.25}$$

Compute the unique solution $K(x, y)$ of the Marchenko equation

$$K(x,z) + g(x+z) + \int_0^{\infty} g(x+z+\xi)K(x,\xi)\mathrm{d}\xi = 0, \quad z > 0. \tag{3.26}$$

The scattering potential is recovered by

$$V(z) = -\frac{\mathrm{d}}{\mathrm{d}z}K(z, 0^+). \tag{3.27}$$

The remarkable feature of the GLM method is the reduction from the highly nonlinear operator $\mathcal{R}^{-1}$ to a *linear* integral equation, which can easily be solved by a direct discretization approach (see section 3.2.3).

In the literature [76, 81, 82] there exists a variety of equivalent GLM integral equations, which are dealing with the reflection "from the right" (mirrored scattering potential). The algorithm 2, stated here, deals with the reflection "from the left", which is depicted in figure 2.3a). These variations, however, affect the inverted potential only by mirroring and shifting it, and are thus easily reversible.

Another important property of the GLM method is the fact that only the Fourier transform of the reflection is required. This property is presumable the most useful feature in application as the real or imaginary part alone are sufficient to determine the Fourier transform: The reflection is symmetric with respect to complex conjugation (see

section 2.3.4) and thus the Fourier transform is completely real

$$\hat{g}(t) = \frac{1}{\pi} \operatorname{Re} \int_0^\infty R(k) e^{2ikt} \mathrm{d}k. \tag{3.28}$$

Furthermore, the scattering potential can always be shifted such that $z = 0$ denotes the distinction between non-scattering medium and sample which ensures that the Fourier transform is causal and hence $\hat{g}(t) = 0$ for any $t \leq 0$. It immediately follows that

$$\hat{g}(t) = \frac{2}{\pi} \int_0^\infty \operatorname{Re} R(k) \cos(2kt) \mathrm{d}k = \frac{2}{\pi} \int_0^\infty \operatorname{Im} R(k) \sin(2kt) \mathrm{d}k. \tag{3.29}$$

The consequence is that one needs only the real or imaginary part of the reflection to recover the scattering potential, and in particular, this reduces the number of required measurements to retrieve the phase information from three to two (see section 3.3.2.1).

3.2.3 Numerical Implementation

There are multiple implementations of a GLM solver available with computational complexity of $\mathcal{O}(N^3)$ or faster [76, 83, 84] with N being the number of discretization points which is proportional to the number of z values where the potential $V(z)$ is evaluated. A direct discretization approach has a complexity of $\mathcal{O}(N^4)$, however, with an approximation trick it can be realized in $\mathcal{O}(N^3)$.

As there are only limited implementations freely available, which, additionally, behaved badly with truncated reflection data, a new implementation was developed using a direct discretization scheme. As the GLM method is extensively used later in this work, e. g. in section 3.3.3, the implementation was further optimized to a computational complexity of $\mathcal{O}(N^3)$ which is comparable with the implementations in the literature [76]. The details of the implementation are shown in appendix B.3 and only a rough overview is given here.

The GLM integral equation is discretized on a uniform grid for each $z \in \mathbb{R}$ which yields a linear equation in the unknown kernel $\vec{K}(z) \in \mathbb{R}^{N+1}$

$$\Omega(z) \cdot \vec{K}(z) = -G(z), \tag{3.30}$$

where the vector $G(z) \in \mathbb{R}^{N+1}$ only contains the Fourier transform of the reflection, $\vec{K}(z)$ is the discretization of the kernel $K(z, \cdot)$ in the second variable and $\Omega(z) \in \mathbb{R}^{(N+1)\times(N+1)}$ is the discretization scheme of the integral term using the trapezoidal rule in the GLM equation (3.26).

By exploiting the structure of the discretization scheme $\Omega(z)$, one can relate $\Omega(z_1)$ with $\Omega(z)$ for any $z_1 < z$. Similarly, the LU decomposition of $\Omega(z) = L(z)U(z)$ is used to approximate the LU decomposition of $\Omega(z_1) = L(z_1)U(z_1)$. Hence, one needs to perform only one LU decomposition of $\Omega(z)$ and the LU decompositions of $\Omega(z_1)$ are approximated from $L(z)$ and $U(z)$. As one LU decomposition has computational complexity $\mathcal{O}(N^3)$ and the approximated LU decompositions are easily derived with negligible computational effort, it is possible to compute $K(z, 0^+)$ for all z on a grid

with N points in $\mathcal{O}(N^3)$. Finally, the scattering potential V is determined by a finite difference approximation.

The implementation of the direct discretization algorithm is freely available [85]. It is written in the Python programming language [86] utilizing the numpy [87] and scipy [88] package for the LU decomposition and matrix inversion. This implementation is used for any reflection inversion in this work.

3.3 Phase Information

An alternative and more sophisticated approach to analyze reflectivity data is by taking the phase information of the reflection into account. The phase information $\phi(q)$ is the angle of the reflection $R(q)$ in the complex plane with respect to the real axis

$$R(q) = |R(q)|e^{i\phi(q)}. \tag{3.31}$$

Knowing the phase information ϕ and the reflectivity $|R|$ is thus equivalent to knowing the reflection R.

The advantage of the phase-sensitive approach is that the retrieved SLD profile will be *unique* (see section 3.2.2) under some mild requirements, like only non-absorptive materials can be used and no bound states (see section 3.2.1) exist [31, 76]. In contrast to the fitting approach of section 3.1, the fitting method can only determine *consistent* models but cannot give an exact model.

Also, the SLD reconstructed from phase-sensitive PNR is computed solely on the available data. On the one hand, if the reflection is known only for a limited q-range, the reconstructed SLD will reflect the limited knowledge. The fitting approach, on the other hand, deceives the researcher with a too accurate SLD, i. e. small layer structures are ignored.

The major difficulty for phase-sensitive PNR is the retrieval of the phase information. As only the reflectivity $|R(q)|^2$ is measured, the phase-information is generally lost and has to be retrieved.

3.3.1 Phase Problem

In traditional reflectometry experiments, only the squared modulus of the reflection is measured and the phase ϕ is lost. The phase information, however, contains valuable information for the reconstruction of the scattering potential. The loss of the phase information and thus the loss of the uniqueness between the reflectivity and the scattering potential is known as the *phase problem*.

There are multiple examples how the loss of the phase causes an ambiguity in the scattering potential. For example consider a compactly supported and continuous scattering potential V with co-domain being a subset of the real numbers. By mirroring the potential V at the y axis, a new potential $\hat{V}$ is generated, which in general does not coincide with the first one. The reflections of these potentials do not coincide as well $\mathcal{R}[V] \neq \mathcal{R}[\hat{V}]$, however, the reflectivities are equal $\mathscr{R}^2[V] = \mathscr{R}^2[\hat{V}]$ [46]. Another example, however of academic nature, has already been shown in section 2.5.1 when deriving the reflection using the matrix method. A shifting by L units of the potential is achieved by multiplying the reflection with e^{iqL}. This obviously does not change the reflectivity as the factor e^{iqL} has unit modulus, but the resulting scattering potential "changed" in the sense that it has been shifted.

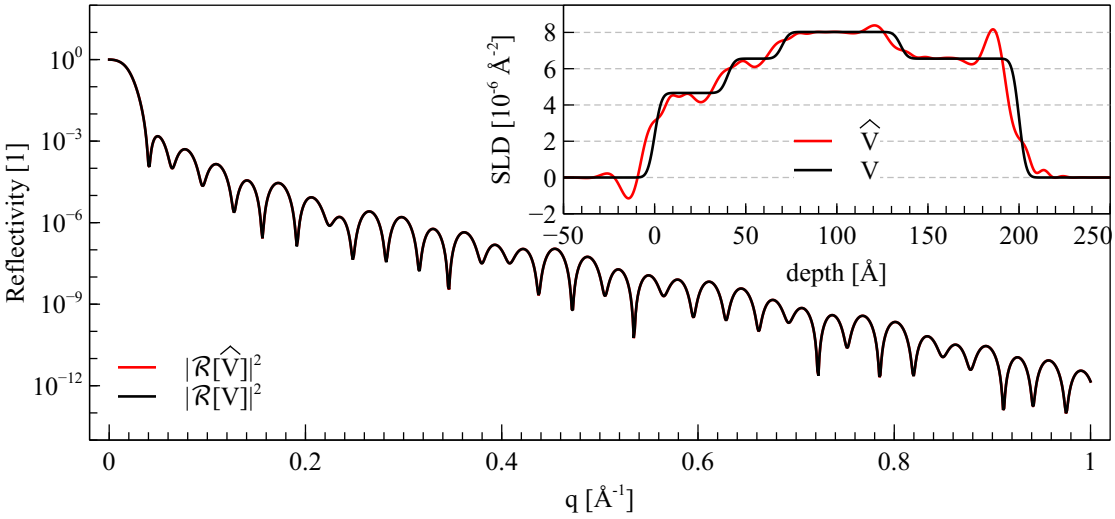

Figure 3.9: Equivalent potentials which yield the same reflectivity. The derived (red curve) potential is generated by taking a phase modifier function $\phi(q) = {}^{2}/_{q}\sin^4(3q)$ and applying equation (3.32) with $\mathcal{R} = \mathcal{F}$ and $\mathcal{R}^{-1} = \mathcal{F}^{-1}$.

Besides these academic examples, there exist a manifold of scattering potentials with the same reflectivity. Take any scattering potential V and compute

$$\hat{V} := \mathcal{R}^{-1}[\mathcal{R}[V]e^{-i\phi}], \tag{3.32}$$

where $\mathcal{R}^{-1}$ is the inverse reflection operator[8], which calculates based on a reflection a matching scattering potential, and ϕ is any continuous and odd ($\phi(-q) = -\phi(q)$) function. The phase ϕ has to be odd in order for the new scattering potential $\hat{V}$ to be real valued as it has to satisfy the symmetry relation $R(-k) = \overline{R(k)}$, see section 2.3.4. Calculating the reflectivity of both scattering potentials yields

$$\mathscr{R}^2[\hat{V}] = \left|\mathcal{R} \circ \mathcal{R}^{-1}[\mathcal{R}[V]e^{-i\phi}]\right|^2 = \left|\mathcal{R}[V]e^{-i\phi}\right|^2 = \mathscr{R}^2[V], \tag{3.33}$$

which, in fact, shows that $\hat{V}$ and V produce the same reflectivity.

Surprisingly, it seems that the reflection operator in the dynamical theory can be replaced by the BA reflection operator. In particular, choosing $\mathcal{R} = \mathcal{F}$ and its inverse, i. e. using simply the Fourier transform and skipping the ${}^{1}/_{q}$ prefactor, works as well and bypasses the computational expensive inversion algorithm in the dynamical theory. Figure 3.9 shows a scattering potential $\hat{V}$ which produces the same reflectivity as V with $\mathcal{R} = \mathcal{F}$.

It is important to notice that there is virtually no restriction on the phase function ϕ, except that it has to be continuous and odd. Thus, arbitrarily many scattering potentials exist with the exact same reflectivity.

[8]The existence of the inverse reflection operator is postponed to section 3.2

As a last method to generate equivalent potentials is to use the *Darboux transformation* [31, 33]. The transformation is used to remove or add bound states to the differential operator corresponding to the wave equation (more details in section 3.2.1). The transformation for adding a bound state $-\beta^2$ is

$$R^*(k) = -\frac{k+i\beta}{k-i\beta}R(k). \tag{3.34}$$

This transformation does not change the reflectivity, i. e. $|R(k)|^2 = |R^*(k)|^2$, but it changes the scattering potential to

$$V^*(z) = V(z) - 2\frac{\mathrm{d}^2}{\mathrm{d}z^2}\log g_\alpha(z), \tag{3.35}$$

where $g_\alpha(z) = \psi^+_{i\beta}(z) + \alpha\psi^-_{i\beta}(z)$ and $\psi^\pm$ are the asymptotic solutions of equation (2.30) and $\alpha > 0$ is an arbitrary constant [31].

3.3.2 Retrieval of the Phase Information

The retrieval of the phase information from the reflectivity is the most difficult task in the process of phase-sensitive PNR. Multiple methods to retrieve the phase information in neutron and x-ray reflectometry have been proposed and the most promising methods are presented here.

The usage of an ordinary differential equation relates the phase of the reflection with the dwell time (viz. the time the neutron "spends" inside the sample) [89]. The solution of the differential equation can be used to determine the phase and thus the reflection. The problem therein is the measurement of the dwell time as the measurement is only correct to first order in the absorption [90].

Another idea is to use the Kramers-Kronig relation [91–93]. A logarithmic dispersion relation is established to associate the phase with the reflectivity $\mathscr{R}^2[\rho] \sim |\mathcal{F}[\rho']|^2$ in the BA by [91]

$$\phi(q) = \frac{2q}{\pi}\int_0^\infty \frac{\log(|\mathcal{F}[\rho'](\zeta)|/|\mathcal{F}[\rho'](q)|)}{q^2-\zeta^2}\mathrm{d}\zeta. \tag{3.36}$$

The method seems to be promising at first glance, however, the logarithmic dispersion relation is a global method, requiring the knowledge of the reflectivity over the whole q range to determine the phase. The method was therefore not further investigated.

The most prominent method for phase reconstruction is the reference layer method [46, 94]. The idea is to constrain the phase with multiple reflectivity measurement of the same sample while varying known regions in the sample until the phase can uniquely be determined.

In the reference layer method one can vary the SLD by

1. using buried or fronting layers [95, 96];

2. changing the magnetization of the sample [97, 98];

3. varying the sample's surroundings [99].

Other approaches with the reference layer method use specific materials which exhibit resonance effects for wavelengths close to absorption edges. Known parts of the SLD can be varied while the remaining part stays constant. These variations in the SLD lead to a variation in the reflectivity which are used to constrain the phase. The resonance method is mainly used for x-rays [100] and rarely for neutrons as only few materials exhibits resonance effects when using neutrons as a probe. However, progress in neutron reflectometry using rare earths as suitable resonance materials [101] has been made recently and experiments have been performed [102–104].

For *in situ* PNR the most suited phase retrieval approach is the reference layer method with varying fronting layers. Additional layers can easily be deposited on top of the sample while the sample stays aligned in the neutron beam, thus, enabling a variation in the top reference layer.

3.3.2.1 Reference Layer Method

The reference layer method uses a known part of the SLD to constrain the phase information of the reflection. The basic property which allows this approach is the multiplicative property of the transfer matrix. As shown in section 2.5.2 the transfer matrix can be split into two transfer matrices at any z inside the sample, see equation (2.60). For the fronting reference layer method, the splitting of the SLD is performed such that the transfer matrix is decomposed into a *known* and *unknown* transfer matrix. The known matrix corresponds to the top layer

$$\mathcal{T}(k) = \mathcal{T}_{\mathrm{U}}(k)\mathcal{T}_{\mathrm{K}}(k). \tag{3.37}$$

If one has four known transfer matrices $\mathcal{T}_{\mathrm{K},i}(k)$ and measure their response on $\mathcal{T}_i$, it is clear that one can completely determine the unknown matrix and the reflection. In fact, as the goal is rather the reflection than the transfer matrix, already three measurements are sufficient: Recall that the reflection can be understood as a function of the transfer matrix. If one ignores the shifting of the potential by the exponential factor in equation (2.57), the reflection is expressed in the form

$$\begin{aligned} R(\mathcal{T}) &= \frac{(n_f^2 n_b^2 \mathcal{T}_{12}^2 + n_f^2 \mathcal{T}_{22}^2) - (n_b^2 \mathcal{T}_{11}^2 + \mathcal{T}_{21}^2) + 2i(n_f n_b^2 \mathcal{T}_{11}\mathcal{T}_{12} + n_f \mathcal{T}_{21}\mathcal{T}_{22})}{(n_f^2 n_b^2 \mathcal{T}_{12}^2 + n_f^2 \mathcal{T}_{22}^2) + (n_b^2 \mathcal{T}_{11}^2 + \mathcal{T}_{21}^2) + 2n_f n_b} \\ &= -\frac{\alpha^{fb} - \beta^{fb} - 2i\gamma^{fb}}{\alpha^{fb} + \beta^{fb} + 2} = -\frac{\alpha^{fb} - \beta^{fb} \mp 2i\sqrt{\alpha^{fb}\beta^{fb} - 1}}{\alpha^{fb} + \beta^{fb} + 2}, \end{aligned} \tag{3.38}$$

where the unimodularity (Lemma 2) of the transfer matrix $(\gamma^{fb})^2 = \alpha^{fb}\beta^{fb} - \det^2 \mathcal{T} = \alpha^{fb}\beta^{fb} - 1$ was used and the quantities α^{fb}, β^{fb} and γ^{fb} are introduced for easier reading,

which are defined as

$$\begin{aligned}\alpha^{fb} &= n_f^{-1} n_b \mathcal{T}_{11}^2 + n_f^{-1} n_b^{-1} \mathcal{T}_{21}^2 \\ \beta^{fb} &= n_f n_b \mathcal{T}_{12}^2 + n_f n_b^{-1} \mathcal{T}_{22}^2 \\ \gamma^{fb} &= n_b \mathcal{T}_{11} \mathcal{T}_{12} + n_b^{-1} \mathcal{T}_{21} \mathcal{T}_{22}.\end{aligned} \tag{3.39}$$

The indices f, b denote the fronting and backing surrounding of the sample and n_f denotes the refractive index of the fronting material which is usually vacuum or air. Here, the point is that the reflection is determined by three parameters, and hence, only three variations of the reference have to be performed. The connection between the measured reflectivity and these parameters is easily established by

$$\Sigma \coloneqq 2 n_f n_b \frac{1 + |R|^2}{1 - |R|^2} = n_f n_b (\alpha^{fb} + \beta^{fb}), \tag{3.40}$$

where the unimodularity property was used again.

Now, the matrix decomposition for the reflection is used to solve for the unknown parameters α, β and γ in terms of the known matrix elements of $\mathcal{T}_\mathrm{K}$. As this is a rather tedious algebraic procedure it is moved to appendix B.1 and only the result is presented here. The following result does only hold as long as the transfer matrix $\mathcal{T}$ is real valued, meaning, only a non-absorptive SLD yields the relation

$$\Sigma = 2 n_f n_b \frac{1 + |R(\mathcal{T}_\mathrm{U} \mathcal{T}_\mathrm{K})|^2}{1 - |R(\mathcal{T}_\mathrm{U} \mathcal{T}_\mathrm{K})|^2} = c_\mathrm{K} \cdot \begin{pmatrix} \alpha \\ \beta \\ \gamma \end{pmatrix}_\mathrm{U}^{bb}. \tag{3.41}$$

The subscript K and U denotes the correspondence of the known and unknown transfer matrix, respectively, and the superscript corresponds to the fronting and backing material. The superscript and subscript is applied on all components of the vector. For example, $\alpha_\mathrm{U}^{bb} = \mathcal{T}_{11,U}^2 + n_b^{-2} \mathcal{T}_{21,U}^2$. The row vector $c_\mathrm{K} \in \mathbb{R}^{1\times 3}$ denotes a "constrain" of the reflection; it depends only on the known transfer matrix and the fronting material.

The rather surprising feature of this equation is that the measured reflectivity can be decomposed into a linear equation involving a vector c_K which depends on the known transfer matrix and the unknown parameter vector.

Consequently, a combination of three different transfer matrices $\mathcal{T}_i = \mathcal{T}_\mathrm{U} \mathcal{T}_{\mathrm{K},i}$ with corresponding reflectivities $|R_i|^2$ uniquely determines the unknown vector

$$\Theta_\mathrm{U}^{bb} \coloneqq \begin{pmatrix} \alpha \\ \beta \\ \gamma \end{pmatrix}_\mathrm{U}^{bb} = C_\mathrm{K}^{-1} \Sigma, \tag{3.42}$$

where $C_\mathrm{K} = (c_{\mathrm{K},i})_{i=1,2,3}$ is the constraint matrix and $\Sigma = (\Sigma_i)_{i=1,2,3}^\mathsf{T}$ is the transformed reflectivity vector.

Some care has to be taken when interpreting the retrieved reflection R_ret associated with the parameter vector Θ_U^{bb}. The retrieved reflection corresponds to the sample with the fronting reference layer removed and the fronting refractive index is replaced by the

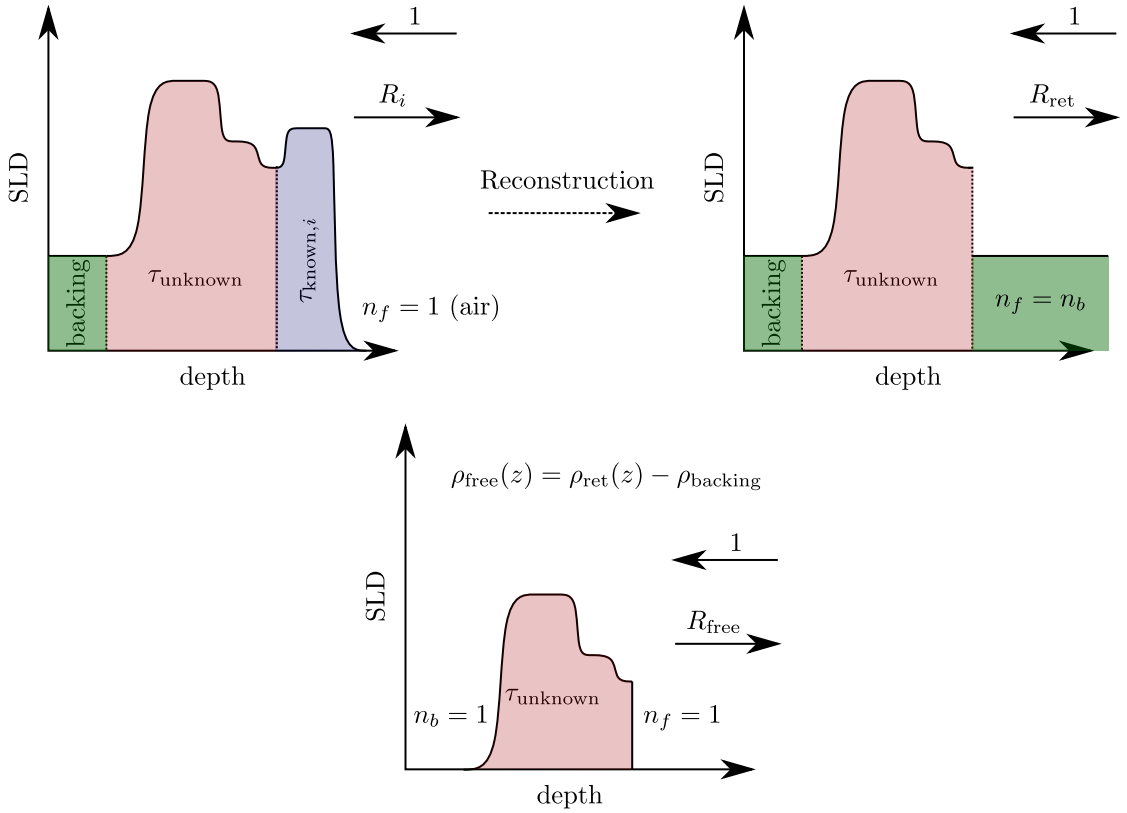

Figure 3.10: Illustration of the reference layer method and the potential corresponding to the retrieved reflection. The reconstructed potential corresponds to the unknown sample but with the fronting and backing being equal. An equivalent potential of a free film can be calculated by subtracting the backing SLD ρ_{backing}.

backing refractive index. Hence, the retrieved reflection R_{ret} differs from the reflection of the unknown sample $R(\mathcal{T}_{\text{U}})$ and, of course, also from the reflection of the sample with the reference layer attached on top $R(\mathcal{T}_i)$:

$$R_{\text{ret}} = R(\Theta_{\text{U}}^{bb}) = R(\mathcal{T}_{\text{U}})\big|_{n_f \leftarrow n_b} \neq R(\mathcal{T}_{\text{U}}) \neq R(\mathcal{T}_i). \tag{3.43}$$

The SLD of the unknown sample can then be calculated by a free standing film as the fronting and backing material is known. Figure 3.10 illustrates the situation, relating the reflection of the measured samples with the retrieved reflection and the reflection of a free-standing film.

The reference layers can have an arbitrary structure. They neither need to have the same thickness nor density. They can be made up of multiple different layers if desired or simply be a single layer. In particular, mono-layers can be used as reference layers, however, numerical errors and measurement uncertainty can impede the retrieval.

It is noted that the matrix C_{K} might not be invertible, however, this rarely happens in practice and if the matrix is not invertible it happens only at isolated k values. Still,

the condition number of the constraint matrix in a neighborhood of a singular k_s value is high, resulting in larger numerical errors of the inverted reflection in a neighborhood of k_s. The condition number of a matrix A is a bound on how inaccurate the solution x to $Ax = b$ will be if b is only approximated. The condition number is the maximum of the relative error in x to the relative error in b. Higher condition numbers yield a worse solution x, whereas low condition numbers guarantee a good approximate solution x. As a rule of thumb, a condition number of 10^d indicates that the solution x of the equation $Ax = b$ has lost d digits of precision [105]. Alternatively, high condition numbers signalize an almost singular matrix.

Figure 3.11 shows a phase reconstruction using three reflectivity measurements. The deviation of the retrieved reflection from the exact reflection at for example $q \approx 1.2\,\text{Å}^{-1}$ is primarily caused by the bad condition number of the constraint matrix which indicates that the constraint matrix is nearly singular, or equivalently, the constraints of the reference layers are almost redundant. This problem can be overcome by taking more than three reflectivities and associated reference layers into consideration. However, some attention has to be paid on the influence of measurement uncertainty, see section 3.4.1.

Interestingly, the real part of the reflection can be "easier" reconstructed as the imaginary part. The imaginary part in equation (3.38) in principle depends on α, β and γ[9], whereas the real part only needs the information of α and β. This subtle fact can be exploited to reconstruct the real part only with the knowledge of two reflectivities measurements instead of three. In section 3.2 it was shown that the real or imaginary part alone are sufficient to invert the reflection and obtain the desired scattering potential.

3.3.3 Retrieval at the Total Reflection Edge

The reference layer method can uniquely retrieve the reflection and phase information locally of the unknown sample. Yet, the reference layer method is unable to retrieve the phase at the total reflection edge where $|R(q)|^2 = 1$, because the involved quantity $\Sigma \sim \frac{1+|R(q)|^2}{1-|R(q)|^2}$ is undefined.

The regime of total reflection is usually quite small; for example a sample with a Si substrate has a critical wave vector $q_c \approx 0.01\,\text{Å}^{-1}$ which can be estimated with equation (2.28). Even though the regime is small, the reflection therein influences on the reconstructed potential drastically. Figure 3.12 shows the influence of the low q reflection on the reconstructed potential. It is therefore crucial to retrieve the reflection at the total reflection edge.

Tricks like flipping the sample upside down and measuring the reflectivity through the substrate are not feasible for the phase retrieval. Flipping the sample removes the total reflection edge q_c, however, it also introduces a shift in the wave vector transfer which is exactly equal to q_c. Hence the effective wave vector transfer becomes $q^2_{\text{flipped}} = \left(\frac{4\pi}{\lambda}\sin\theta\right)^2 + 16\pi\rho_{\text{Substrate}}$ [45] and a retrieval below is not possible as $q_c \leq q_{\text{flipped}}$.

Earlier works [95, 97] circumvented this problem by extrapolating the reflection from the last retrievable q value to $q = 0$ as the reflection at $q = 0$ is always known to

[9] Actually, α and β together with the sign are sufficient due to unimodularity: $\gamma = \pm\sqrt{\alpha\beta - 1}$

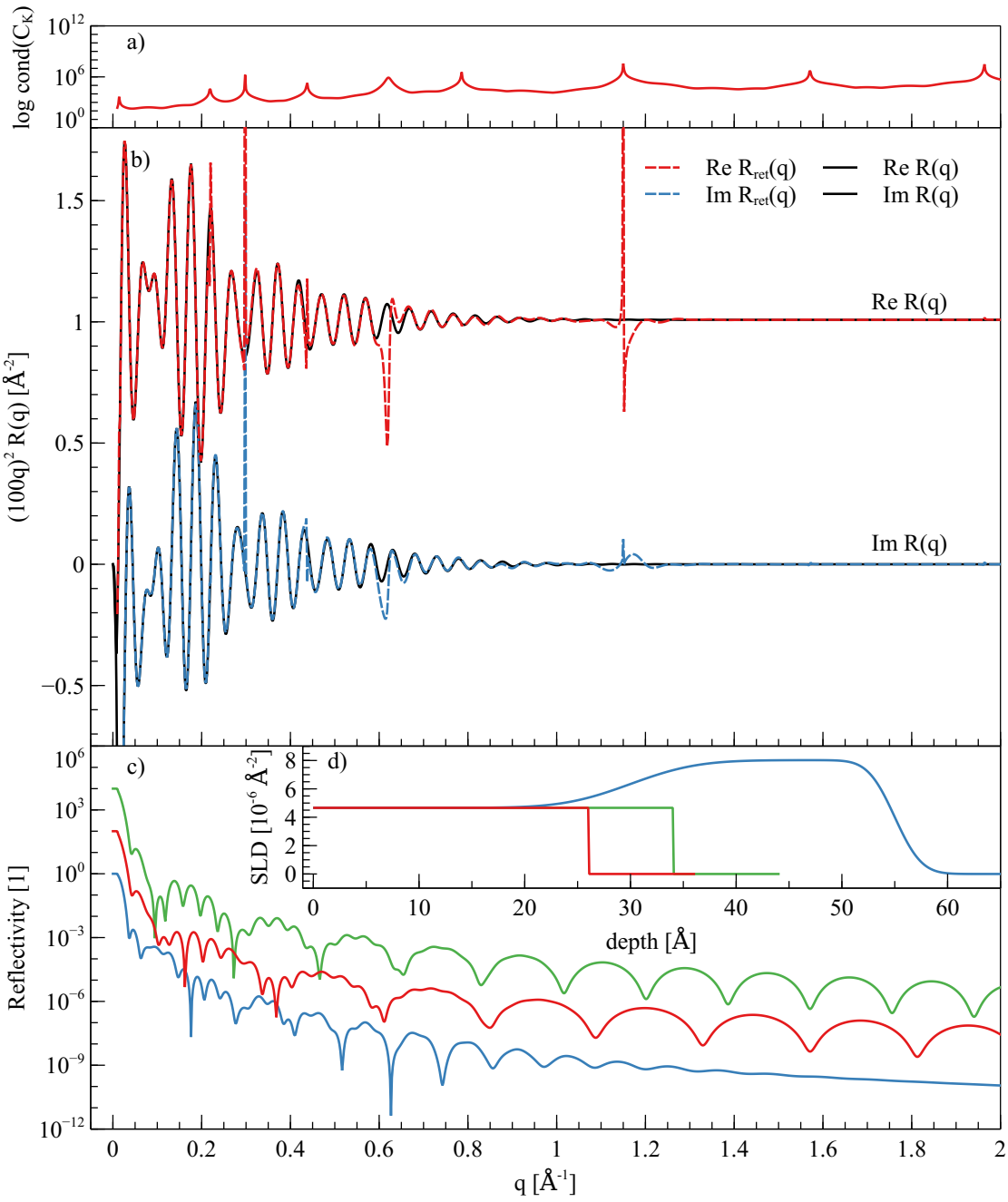

Figure 3.11: Reconstruction of the reflection of three reflectivity measurements. a) The condition number of the constraint matrix. b) The scaled, retrieved reflection (dashed) and the exact reflection (solid curve, black). c) The reflectivities of the unknown sample with three different reference layers which are depicted in the inset d) The bad phase retrieval is correlated with the condition number of the constraint matrix, indicating a linear dependence of the reference layers.

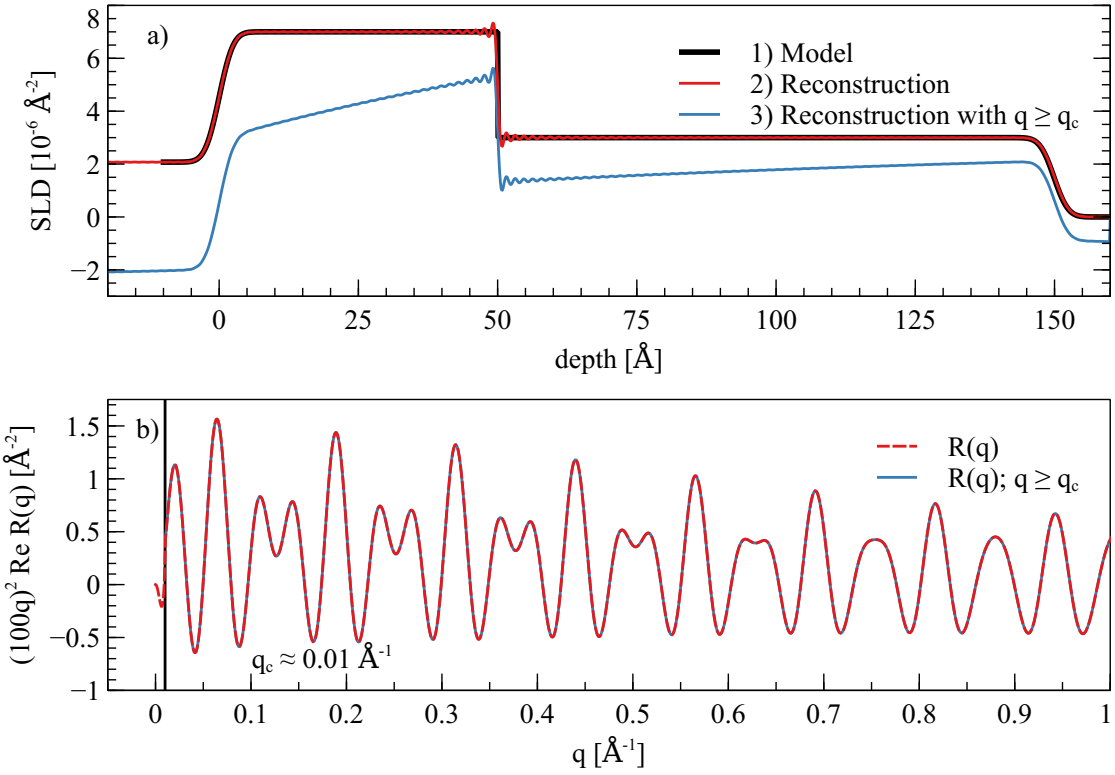

Figure 3.12: Influence of the low q truncated reflection onto the reconstructed SLD. a) The reconstructed potentials. 1) Corresponds to the exact model 2) is the inverted SLD using the reflection $R(q)$ for $0 \leq q \leq 4\,\text{Å}^{-1}$ 3) is the inverted SLD using $R(q)$ for $q_c \leq q \leq 4\,\text{Å}^{-1}$. b) The exact reflection of the model SLD based on a Si/Fe(50 Å)/Cu(100 Å)/air sample. The black vertical line indicates the critical edge q_c which is determined by the Si SLD.

be $R(0) = -1$, see section 2.5.2.3. Indeed, an extrapolation is possible, however, this requires a slab model of the sample which should be avoided in a model-free approach.

In fact, there is phase retrieval technique which additionally measures the polarization of the reflected neutrons to determine the phase of the reflection, even in the regime of total reflection [106, 107]. Assuming suitable conditions, the reflection below the critical edge can be numerically approximated using only the retrieved reflection [108]. The algorithm is presented in the following.

3.3.3.1 Fixed-point Algorithm

If the scattering potential[10] of the sample is known, it is obviously possible to calculate the reflection, in particular in the regime of total reflection. However, the scattering potential is unknown, but it may be possible to guess a scattering potential which is approximately equal to the true scattering potential. The reflection is then simply calculated from the approximated sample and the true reflection below the critical edge is replaced by the approximated reflection with an additional interpolation between $R(0) = -1$ to $R(q_c)$. This procedure has been common practice [95, 99] since the time the reference layer method has been developed.

The numerical algorithm to retrieve the phase information is based on the idea of approximating the scattering potential, however, the guessed scattering potential is replaced by the inverted reflection ignoring the fact that the reflection is not known in the regime of total reflection. The process (guessing a scattering potential and calculating the reflection) is repeated until a termination criterion is met.

Before the algorithm is exactly defined, some advantages of this ansatz need to be pointed out:

1. The algorithm can be run with no additional information except an estimate of the film thickness. The film thickness, in turn, is estimated from the measured reflectivity.

2. The algorithm can be expressed as a fixed-point iteration. It is relatively easy to show the convergence to a unique solution in the BA.

3. The termination criteria can be set for example such that the improvement from consecutive iterations is below a given threshold. The true scattering potential corresponds to a fixed point of the iteration, making the above termination criteria a reasonable choice.

4. The rate of convergence for this fixed-point iterations is linear. Thus, the fixed-point algorithm converges quickly. It is noted that the rate of convergence is called *linear* if the ratio of consecutive iterations x_k converges:

$$\lim_{k\to\infty} \frac{|x_{k+1} - x_\infty|}{|x_k - x_\infty|} = \mu \quad \text{with} \quad \mu \in (0, 1).$$

   More intuitively, one could say that the algorithm exponentially fast decays to the fixed point with respect to the iteration number. For example, $x_k = 1/2^k$ has a linear rate of convergence to $x_\infty = 0$ with $\mu = 1/2$.

The *direct problem* in scattering theory is the challenge to calculate the reflection R given a scattering potential V. The *indirect problem* is the inverse operation, namely,

[10] This section uses the scattering potential V as the sample description instead of the SLD ρ and uses the wave number k instead of the wave vector transfer q. Recall that $V = 4\pi\rho$ in the wave equation (2.15) and $2k = q$ by equation (2.24).

calculate the scattering potential V based on the reflection R. In section 3.2 the requirements for the inversion are discussed. The direct and indirect problem are denoted by $\mathcal{D}$ and $\mathcal{I}$, respectively, and in the BA there exist explicit formulas. The direct problem was already discussed in section 2.4, however, here the formula is stated for the scattering potential instead of the SLD

$$\begin{aligned} \mathcal{D}_{\mathrm{BA}} = \mathcal{R}_{\mathrm{BA}}[V](k) &= \frac{1}{ik}\int_{\mathbb{R}} V(z)e^{-ikz}\mathrm{d}z, \quad k \neq 0 \\ \mathcal{I}_{\mathrm{BA}} = \mathcal{R}_{\mathrm{BA}}^{-1}[R](z) &= \frac{i}{2\pi}\int_{\mathbb{R}} kR(k)e^{ikz}\mathrm{d}k. \end{aligned} \tag{3.44}$$

In practice one can never retrieve the reflection up to $k \to \infty$ and hence some degradation operators, which are the truncation and projection operator, need to be introduced. To ensure convergence of the algorithm, a constraint operator is required as well.

The truncation operator $\mathcal{T}_\kappa^K$ acts on any function $f\colon \mathbb{R} \to \mathbb{C}$ by

$$\mathcal{T}_\kappa^K[f](k) = \begin{cases} f(k) & \text{if } \kappa \leq |k| \leq K, \\ 0 & \text{otherwise.} \end{cases} \tag{3.45}$$

In the context of reflectometry, the truncation operator will be applied on the reflection function. Its purpose is to cut off the reflection where the reflection could not be reconstructed. This region is defined by the total reflection edge and the maximal measured k value. It is noted that the truncation operator uses the region $\kappa \leq |k| \leq K$. In fact the reflection is retrieved only for positive k values, but because of the symmetry relation $R(-k) = \overline{R(k)}$ (see section 2.3.4) is extended to negative k values, which is taken care of in the definition of the truncation operator.

The projection operator $\mathcal{P}_R$ acts on any function f by selecting either the function f or R to evaluate, based on the maximal measured k value. It is defined as

$$\mathcal{P}_R^K[f](k) = \begin{cases} f(k) & \text{if } 0 \leq |k| \leq K, \\ R(k) & \text{otherwise.} \end{cases} \tag{3.46}$$

This operator guarantees that the fixed-point algorithm will always use the retrieved (or measured) reflection R instead of an approximative reflection whenever the retrieved reflection is available.

And finally, the constraint operator $\mathcal{C}$ is introduced. As this operator highly depends on the available *a priori* knowledge of the potential V, there is no general definition. However, if, for example, the film thickness L of the sample is known, a suitable choice of the constraint operator is

$$\mathcal{C}[V](x) = \chi_{[0,L]}(x)V(x), \tag{3.47}$$

where $\chi_{[0,L]}(x)$ denotes the indicator function. Note that the retrieved reflection corresponds to a free-standing film, and the potential is thus indeed zero on $[0, L]^{\mathsf{c}}$. However, other choices of the constraint operator are possible as well, e. g. if the reflection does not

correspond to a free-standing film but has a substrate V_{sub}, or the scattering potential inside the film on $[a,b] \subset [0,L]$ is known to be V_{known}

$$\mathcal{C}[V](x) = \chi_{(-\infty,0)}(x)V_{\mathrm{sub}} + \chi_{[0,L]\setminus[a,b]}(x)V(x) + \chi_{[a,b]}(x)V_{\mathrm{known}}(x). \tag{3.48}$$

Similarly, a non-vacuum fronting can be implemented as well. The crucial point in the constraint operator is that the unknown part of the sample has a bounded support.

Definition of the Fixed-point Algorithm Assume that the reflection $R_{\mathrm{ret}} = \mathcal{R}[V]$ is retrieved for $k_c \leq |k| \leq K$ with a theoretically exact potential $V \in L^1([0,L])$. In terms of the recently introduced operators, only $\mathcal{T}_{k_c}^{K}[R_{\mathrm{ret}}]$ is known. Because of the incomplete knowledge of R_{ret}, the ideal operators $\mathcal{R}$ and $\mathcal{R}^{-1}$ are replaced by

$$\begin{aligned} \mathcal{R} \to \mathcal{D} &\coloneqq \mathcal{T}_0^K \circ \mathcal{P}_{R_{\mathrm{ret}}}^{k_c} \circ \mathcal{R}, \\ \mathcal{R}^{-1} \to \mathcal{I} &\coloneqq \mathcal{C} \circ \mathcal{R}^{-1}, \end{aligned} \tag{3.49}$$

with $\mathcal{D}$ and $\mathcal{I}$ being the direct and indirect problem, respectively. The fixed-point algorithm $\mathcal{A}$ is defined as

$$\begin{aligned} \mathcal{A} &\coloneqq \mathcal{I} \circ \mathcal{D}, \\ V_{n+1} &\coloneqq \mathcal{I}[R_n], \\ R_{n+1} &\coloneqq \mathcal{D}[V_{n+1}], \end{aligned} \tag{3.50}$$

with the initial scattering potential $V_0 \coloneqq \left(\mathcal{I} \circ \mathcal{T}_{k_c}^{K}\right)[R_{\mathrm{ret}}]$.

For an in-depth explanation of the fixed-point iteration, it is useful to state the algorithm in a single formula

$$\mathcal{A}[V_n] = V_{n+1} = \mathcal{C} \circ \mathcal{R}^{-1} \circ \mathcal{T}_0^K \circ \mathcal{P}_{R_{\mathrm{ret}}}^{k_c} \circ \mathcal{R} \tag{3.51}$$

The process of the fixed-point algorithm is described in the following and the first step is illustrated in figure 3.13:

Initialization: The initial reflection R_0 is constructed from the retrieved reflection R_{ret} by setting the unknown values to zero using $\mathcal{T}_{k_c}^{K}$. The initial scattering potential V_0 is computed from the initial reflection R_0 by $V_0 = \mathcal{I}[R_0]$.

1. An intermediate reflection $\hat{R}$ is calculated from V_n by $\mathcal{R}$.
2. The reflection $\hat{R}$ above $|k| > k_c$ is discarded and replaced with the retrieved reflection R_{ret} by applying the operator $\mathcal{P}_{R_{\mathrm{ret}}}^{k_c}$. The reflection above $|k| > K$ is also discarded by $\mathcal{T}_0^K$ and the reflection obtained by the operations is denoted R_{n+1}.
3. An intermediate potential $\hat{V}$ is computed from the reflection R_{n+1} using $\mathcal{R}^{-1}$.
4. The intermediate scattering potential $\hat{V}$ has in general an unbounded support because the high $|k| > K$ and low $|k| < k_c$ frequency oscillations of R_{n+1} are truncated. The potential V_{n+1} is computed by the constraint operator $V_{n+1} = \mathcal{C}[\hat{V}]$ and has bounded support.

5. The procedure is repeated until the change in the reflections $R_{n+1} - R_n$ is sufficiently small.

The fixed-point algorithm originates from the properties of the Fourier transform which map the reflection in the reciprocal space to the scattering potential in the real space in the BA. Large features in the potential correspond to low frequencies and small features are transformed to high frequencies by a Fourier transform. Thus, the knowledge of the thickness, which is, in principle, a large feature, affects primarily the low frequencies of the reflection. This is the reason why one expects that the algorithm is able to retrieve the reflection.

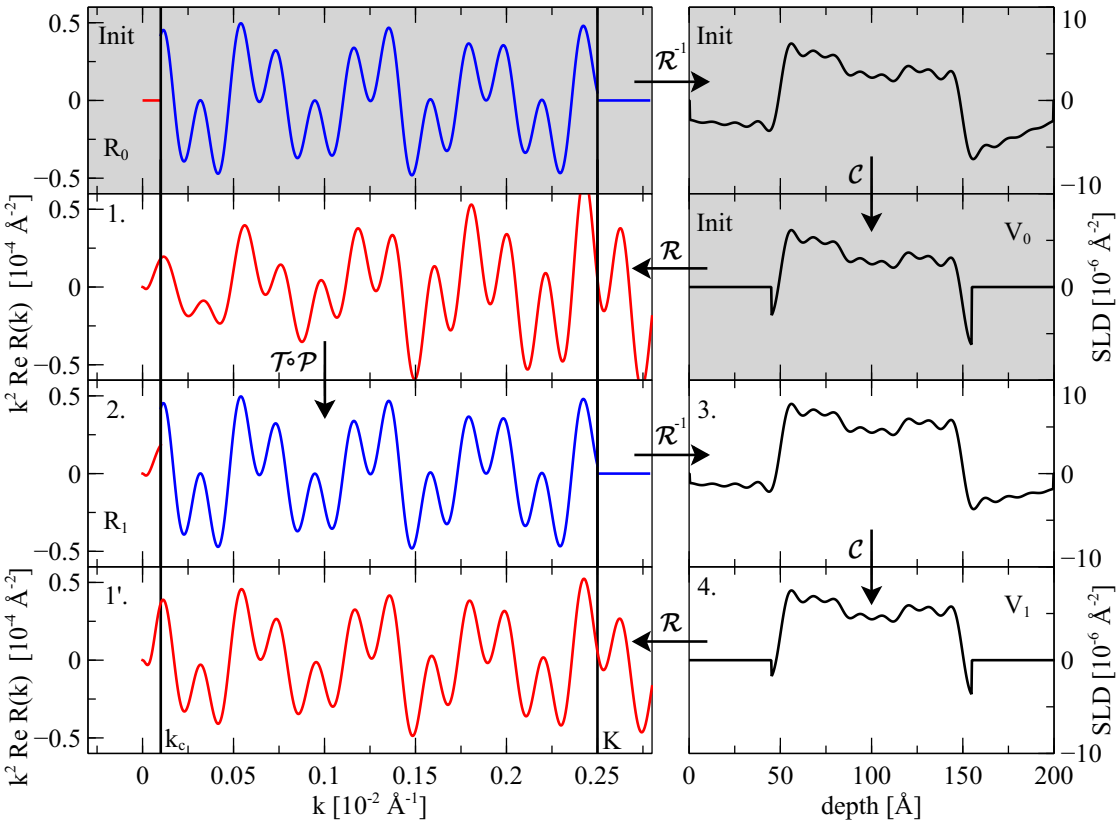

Figure 3.13: Illustration of the first iteration of the fixed-point algorithm (3.50). The left column shows the real part of the scaled reflection for $k \geq 0$, the right column shows the potentials. The labels in the top left corner correspond to the steps described in the text. The graph 1'. shows the algorithm in the second iteration. The gray shaded graphs show the steps performed in the initialization step.

The fixed-point algorithm is defined as a mapping $\mathcal{A}\colon V \mapsto V'$, however, an analogous fixed-point algorithm $\mathcal{A}' := \mathcal{D} \circ \mathcal{I}\colon R \mapsto R'$ is possible as well. The initial reflection is then $\mathcal{T}_{k_c}^{K} R_{\mathrm{ret}}$.

The choice of the initial reflection or initial potential is, in fact, not crucial. In principle, any initial reflection can be used, however, a reflection which is closer to

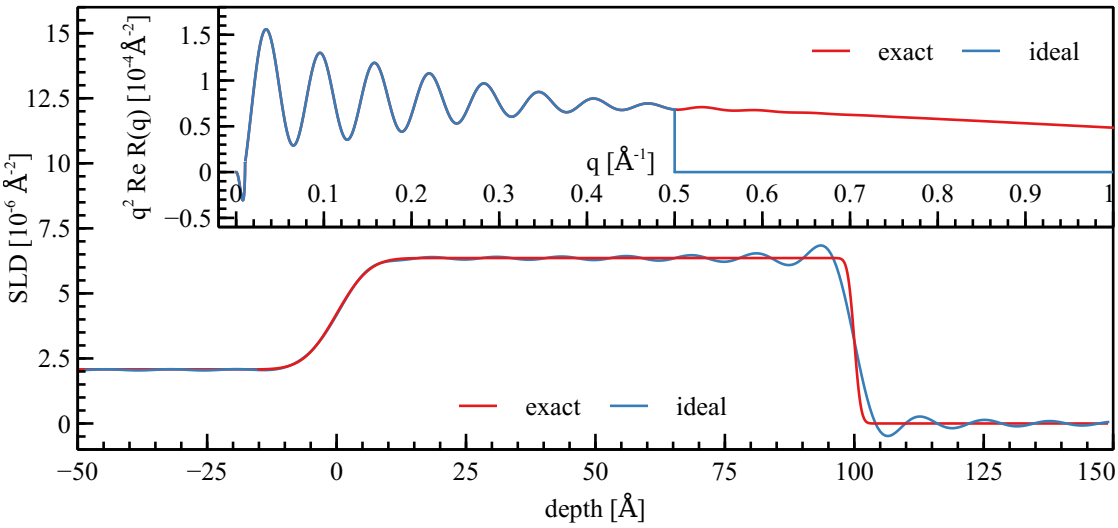

Figure 3.14: Distinction of the ideal to the exact notion. The ideal R^* and exact R reflection is shown in the top graph and the ideal V^* and exact V scattering potential is shown below.

the fixed point decreases the number of iterations. Here, the absence of additional information of the scattering potential prevents an improvement of the initially guessed reflection.

The reflection $\mathcal{T}_0^K \circ \mathcal{R}[V]$ is called *ideal* since it matches the true reflection of the true scattering potential V up to the truncation in high k values. The *exact* reflection $\mathcal{R}[V]$ is the theoretically true reflection, which does not suffer from the truncation at $|k| > K$:

$$R_{\text{ideal}} = \mathcal{T}_0^K \circ R_{\text{exact}}. \tag{3.52}$$

Likewise $\mathcal{A}[V]$ is the *ideal* scattering potential as it is the best possible retrieved scattering potential with k truncated reflection and V is *exact*. It is noted that $\mathcal{A}[V] \neq V$, however, the equation holds in the limit $K \to \infty$. The distinction between the *ideal* and *exact* scattering potential and reflection is shown in figure 3.14.

It is noted that the ideal and exact reflection are both not a fixed point of the algorithm $\mathcal{A}'$ and thus, the fixed point iteration cannot converge to either one. The reason is the truncation operator $\mathcal{T}_0^K$. In fact

$$\begin{aligned} \mathcal{A}'[\mathcal{T}_0^K \circ \mathcal{R}[V]] =& \mathcal{T}_0^K \circ \mathcal{P}_{R_{\text{ret}}}^{k_c} \circ \mathcal{R} \circ \mathcal{C} \circ \mathcal{R}^{-1}[\mathcal{T}_0^K \circ \mathcal{R}[V]] \\ \neq& \mathcal{T}_0^K \circ \mathcal{P}_{R_{\text{ret}}}^{k_c} \circ \mathcal{R} \circ \mathcal{C} \circ \mathcal{R}^{-1}[\mathcal{R}[V]] = \mathcal{T}_0^K \circ \mathcal{R}[V], \end{aligned} \tag{3.53}$$

and analogously, $R[V]$ is not a fixed point of algorithm $\mathcal{A}$. However, in the limit $K \to \infty$, the exact potential V is a fixed point of the iteration $\mathcal{A}$, because $\mathcal{T}_0^K = \text{id}$ as $K \to \infty$; likewise $\mathcal{R}[V]$ is a fixed point of $\mathcal{A}'$ as $K \to \infty$.

Corollary 2 relates the fixed point potential of $\mathcal{A}$ to the ideal potential in the BA. In particular, having retrieved the reflection $R(k)$ for a sufficiently large range of wave

numbers k, the fixed point potential is an approximation to the ideal potential, and thus it is an approximation to the exact potential as well.

Corollary 2 (From [108]). *Let $k_c L < \pi$ and consider the constraint operator $\mathcal{C}[U](x) = \chi_{[0,L]}(x)U(x)$. Then algorithm $\mathcal{A}$ (3.50) converges and it has a unique fixed point $V^* \in L^1([0,L])$ for any initial potential. Furthermore, if the exact potential V is n-times continuously differentiable for $n \geq 2$ and the support of V is a subset of $(0,L)$, the following estimate holds*

$$\|V^* - \mathcal{A}[V]\|_{L^1([0,L])} \leq \frac{k_c L^2 K^{1-n}}{\pi(\pi - k_c L)(1-n)} \left\|V^{(n)}\right\|_{L^1([0,L])}.$$

In particular, the fixed point $V^* = V$ almost everywhere in L^1 in the limit $K \to \infty$.

The condition $k_c L < \pi$ ensures that the scattering potential does not contain large features which influence the reflection for $|k| \leq k_c$. It is possible to loosen this assumption if additional constraints are imposed on a set of measure (or "size") l; the condition in Corollary 2 relaxes to $k_c(L - l) < \pi$. Additional constraints simply reduce the total thickness by the "amount" of constraints. For example, if the scattering potential is known on $[a,b]$ and the constraint is implemented as in equation (3.48), the assumption relaxes to $k_c(L - (b-a)) < \pi$.

3.3.3.2 Numerical Experiments

The algorithm is tested on two different realistic potentials. It usually converges in less than 100 iterations, however, this strongly depends on the selection of k_c and L, i. e. the smaller $k_c L - \pi < 0$ the faster the convergence to the fixed-point.

As choice of the stopping criteria the L^1 or supremum norm is suitable, where the supremum norm usually is stronger in the sense that it achieves a more precise retrieval at the cost of additional iterations. In the following the supremum norm[11] is used, which is defined as

$$\|R_{n+1} - R_n\|_\infty = \max_{0 \leq k \leq k_c} |R_{n+1}(k) - R_n(k)|. \tag{3.54}$$

As the stopping criteria, the condition $\|R_{n+1} - R_n\|_\infty < \varepsilon$ is taken with the tolerance $\varepsilon = 10^{-8}$. The accuracy of the retrieval is measured with the metric of total relative error which is defined as

$$\mathrm{Acc}(R^*) = \frac{1}{N} \sum_{0 \leq k \leq k_c} \left| \frac{R^*(k) - R(k)}{R(k)} \right|, \tag{3.55}$$

where N is the number of elements in the sum, R^* and R are the reflection of the fixed-point and the exact reflection, respectively. The number N is assumed to be finite as the reflection is retrieved at discrete points in k space.

[11] Actually the maximum norm is used, however, as the Fourier transform of an L^1 function is continuous and the domain is compact, the supremum is attained; thus the supremum norm is equivalent to the maximum norm.

A k-spacing of $\Delta k = 5 \times 10^{-3}\,\text{Å}^{-1}$ is used in the following examples. The fixed-point algorithm is performed in the dynamical theory and not in the BA.

Random Scattering Potential A free-standing scattering potential V with a thickness of $L \approx 330\,\text{Å}$ was generated by randomly choosing the thickness, roughness and SLD for a random number of layers. The reflection $R(k)$ is simulated from V in the range $8.5 \times 10^{-3}\,\text{Å}^{-1} = k_c \leq |k| \leq K = 0.25\,\text{Å}^{-1}$. The reflection $R(k)$ for $|k| \leq k_c$ is retrieved by the fixed-point iteration, where the film thickness was assumed to be 330 Å. The prerequisites of Corollary 2 are thus fulfilled. Figure 3.15 shows selected iterations of the fixed-point algorithm $\mathcal{A}$. The algorithm terminated after 66 iterations with an accuracy of $\text{Acc}(R^*) = 2.5 \times 10^{-4}$.

In practice, the solution R^* has to be verified by comparing with the measured reflectivity. They should coincide, but the K truncation prevents a perfect match in general. Figure 3.15 (bottom) shows exactly this behavior. The exact reflectivity does not coincide with $|R_{66}|^2$ at high q values.

Even higher values of k_c lead to a convergence of the algorithm. In fact, the algorithm $\mathcal{A}$ with same configuration but using a higher critical edge $k_c = 1.3 \times 10^{-2}\,\text{Å}^{-1}$ converges anyway but many more iterations ≥ 5000 are required. The accuracy decreases to 1.8×10^{-2}, which is is still acceptable, see figure 3.16. The condition $k_c L < \pi$ in Corollary 2 is violated by roughly 37%, i. e. $k_c L \approx 1.37\pi$, but the algorithm still converged. This suggests that the condition is not necessary, but rather sufficient for the retrieval.

The algorithm $\mathcal{A}$ retrieves a continuous reflection without any additional constraints. The condition $R(0) = -1$ (see section 2.5.2.3) is inherently given by the direct problem $\mathcal{D}$ (see figure 3.15 middle). It is noted that the reflectivity in figure 3.15 (bottom) appears to have a total reflection edge, but this is not the case since the scattering potential is free-standing. The deception is caused by the fact that the scattering potential V has a high average SLD and it is relatively thick.

Thin Layer The next example is an air/Au(40 Å)/Cu(30 Å)/Fe(45 Å)/Cu(40 Å)/air free-standing film. The fixed-point algorithm is tested again on simulated data. The SLD profile is generated with the *refl1d* software [68] using randomly selected rms roughnesses in the range 3.7 Å to 8.2 Å. The total film thickness is $L \approx 150\,\text{Å}$. The reflection $R(k)$ is simulated for $k_c = 0.01\,\text{Å}^{-1} \leq |k| \leq K = 0.1\,\text{Å}^{-1}$

Figure 3.17 depicts selected iterations of the fixed-point iteration. A critical edge $k_c = 10^{-2}\,\text{Å}^{-1}$ is used which is reasonable compared to $k_c \approx 5 \times 10^{-3}\,\text{Å}^{-1}$ for a silicon substrate.

The algorithm uses only a total film thickness of 200 Å as the single constraint. After 47 iterations the algorithm converged with an accuracy of 2.0×10^{-3}. The fixed-point $V^* = V_{47}$ perfectly resembles the structure of the ideal potential.

The rate of convergence seems to decrease rapidly with increasing k_c, but surprisingly, K does not seem to have any influence on the number of iterations for convergence, see figure 3.18. It shows the number of iterations until convergence and the accuracy as a

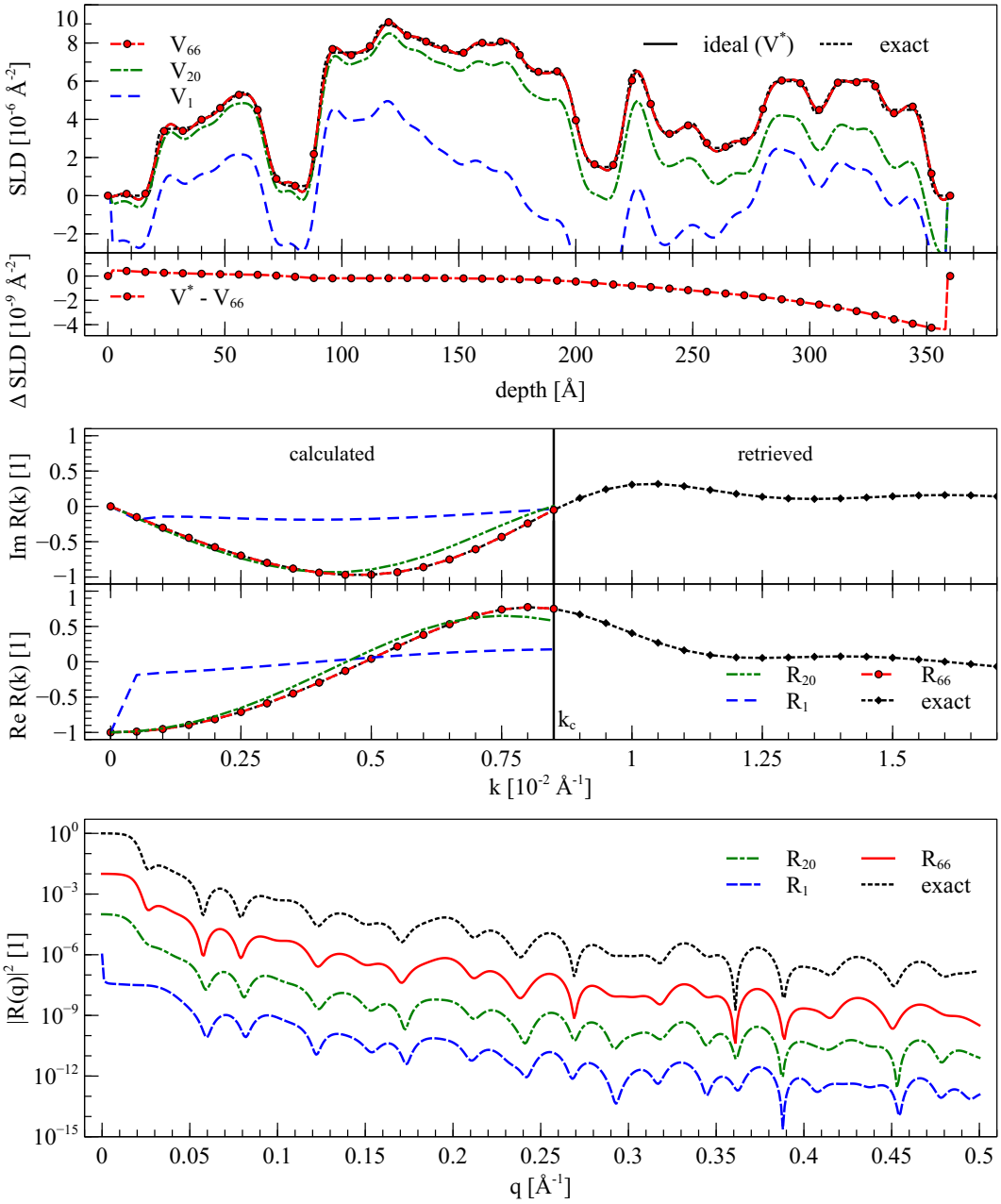

Figure 3.15: Fixed-point algorithm of $\mathcal{A}$ applied on a randomly generated potential. The reflection $R(k)$ was simulated for $k_c = 8.5 \times 10^{-2}\,\text{Å}^{-1} \leq k \leq K = 0.25\,\text{Å}^{-1}$. (Top) Iterations 1, 10, 20, 66 of the fixed-point algorithm together with the exact V and ideal $\mathcal{A}[V]$ potential, respectively. The difference of the fixed point $V^* = V_{66}$ to the ideal potential is shown below. (Middle) Real and imaginary part of the reflection computed from the potentials shown above. The left side is calculated by the fixed-point algorithm whereas the right side is simulated. (Bottom) Reflectivities of the scattering potential shown above. The reflectivity curves are shifted by two orders of magnitude for clarity.

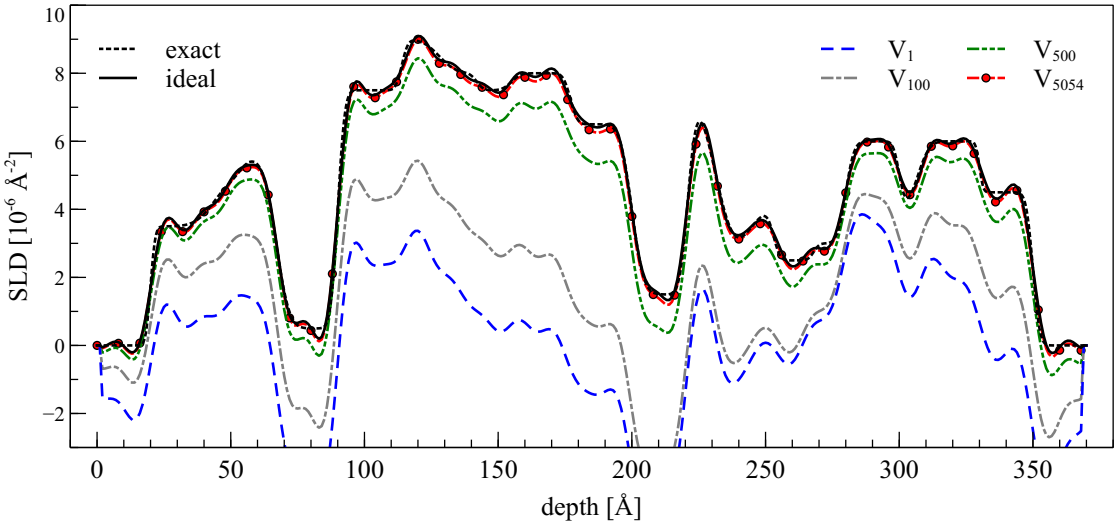

Figure 3.16: Application of the fixed-point algorithm as in figure 3.15 but using $k_c = 1.3 \times 10^{-2}\,\text{Å}^{-1}$.

function of k_c and K, respectively. In addition, the rate of convergence decreases as the assumed film thickness increases.

3.4 Effects of Degraded Reflection

The scattering potential is inverted by using the retrieved reflection data, which in turn is determined by the reflectivity of the same unknown sample but with different reference layers. Mathematically, the reflection R is retrieved by the operator Ret which takes $N \in \mathbb{N}$, $N \geq 3$ measured reflectivities $|R_i|^2$ and associated reference layers L_i and calculates the reflection based on the reference layer method

$$R = \text{Ret}\left[\left(|R_i|^2, L_i\right)_{i=1}^{N}\right]. \tag{3.56}$$

To obtain the scattering potential, the reflection is inverted which is expressed by

$$V = \mathcal{I}[R]. \tag{3.57}$$

Every physical measurement is subject to a measurement error ε. In context of neutron reflectometry, the true reflectivity $|R_i|^2$ cannot be measured but only estimated from the observed reflectivity which is

$$|\hat{R}_i|^2 = |R_i|^2 + \varepsilon_i, \tag{3.58}$$

where the error $\varepsilon_i \sim \mathcal{N}(0, \sigma_i^2)$ is assumed to be normally distributed at $\mu = 0$ with variance σ_i^2. Hence, neither the true reflection nor the true scattering potential are accessible but only the estimated reflection and the estimated scattering potential can

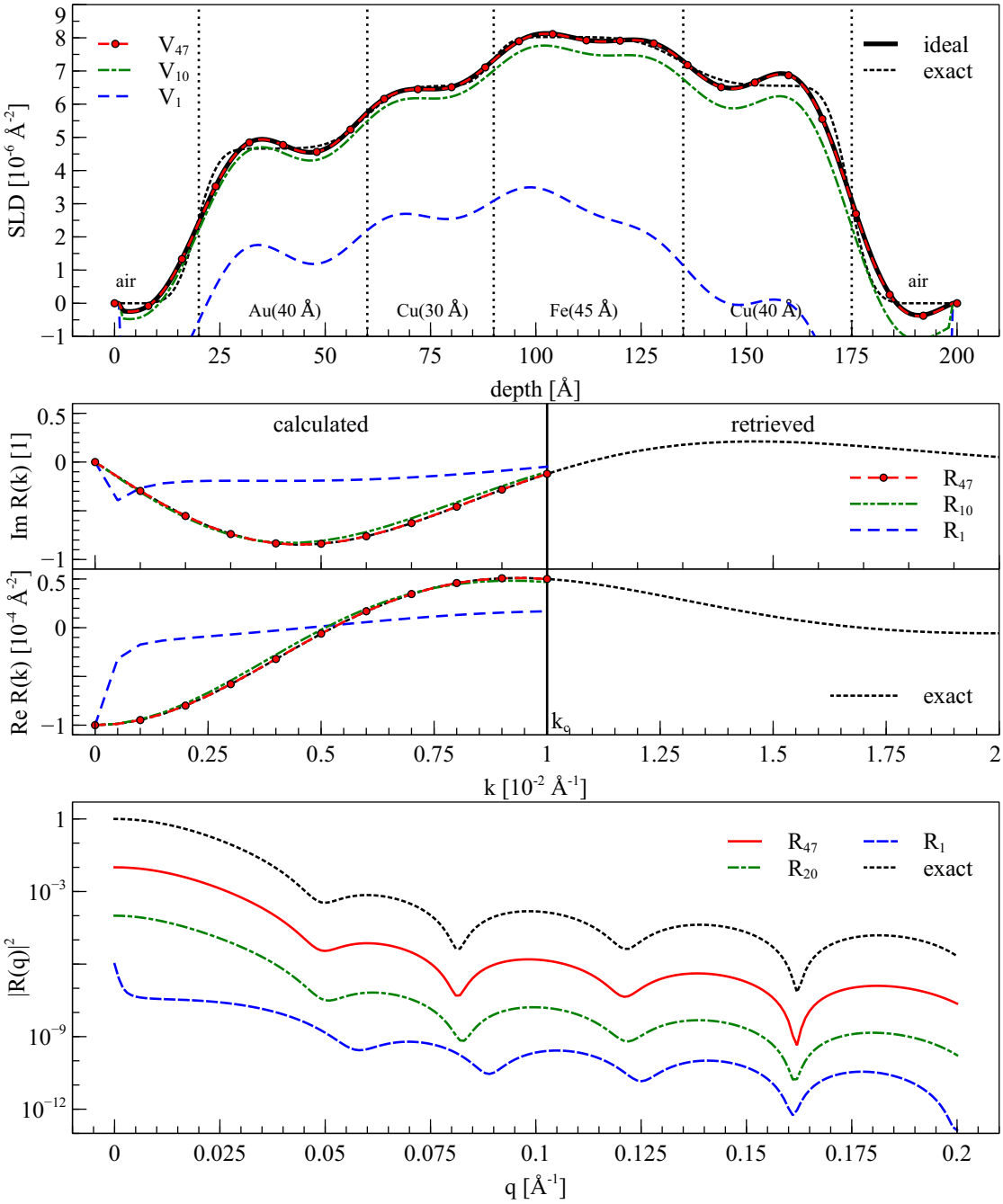

Figure 3.17: Reconstruction of the 150 Å thin multilayer system. (Top) Selected iterations of the scattering potential. (Middle) Retrieved reflection (real & imaginary part) below the critical edge. (Bottom) Reflectivities of the scattering potential shown above together with the exact reflectivity $\mathcal{R}[V]$.

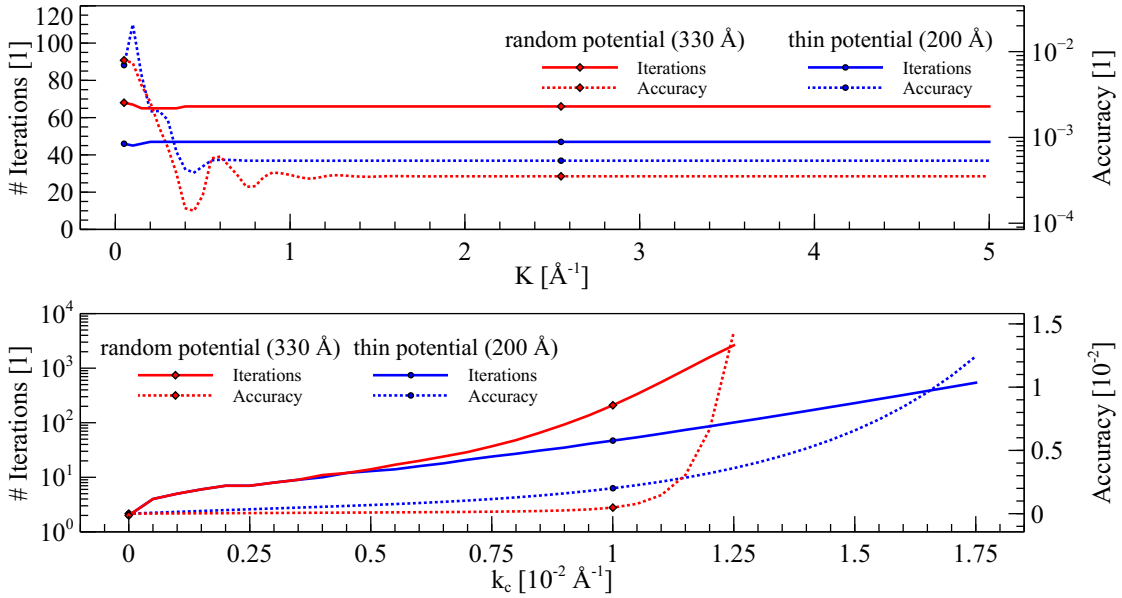

Figure 3.18: Influence of the number of iterations for convergence of $\mathcal{A}$ and of the accuracy while varying K (top) and k_c (bottom), respectively. The respective parameters for the fixed-point iteration did not change from those in figure 3.15 and figure 3.17.

be determined

$$\hat{R} = \mathrm{Ret}\left[\left(|\hat{R}_i|^2, L_i\right)_{i=1}^{N}\right], \quad \hat{V} = \mathcal{I}[\hat{R}]. \tag{3.59}$$

In the following sections the influence of random and systematic errors on the reflection and inverted scattering potential are discussed. On the one hand, random errors are always present in measurements and they vary from one observation to another. Systematic errors, on the other hand, occur always with the same value if the experiment is repeated in the exact same way [109].

3.4.1 Random Measurement Error

To incorporate more than three measurements into the reference layer method, the linear equation (3.41) is generalized to a (weighted) linear least squares problem. The measurement uncertainty can be included in this ansatz:

$$\chi^2(\Theta) = \sum_{i=1}^{N} \left(\frac{C_{\mathrm{K},i} \cdot \Theta - \Sigma_i}{\sigma_{\Sigma_i}} \right)^2. \tag{3.60}$$

The χ^2-minimizing reflection parameter $\hat{\Theta}$ is used as an estimate of the true parameter Θ_{U}^{bb}. The minimizer of χ^2 can be analytically computed by the linear least squares method. In this ansatz, σ_{Σ_i} is the standard deviation of Σ_i which is calculated from the uncertainty of the reflectivity σ_i by $\sigma_{\Sigma_i} = \frac{2}{(1-|R_i|^2)^2}\sigma_i$.

Unfortunately, the minimizer $\hat{\Theta}$ is *biased*, i. e. $E[\hat{\Theta}] \neq \Theta_{\mathrm{U}}^{bb}$, as the error in Σ has a non-zero expectation: To correctly derive the error one has to consider the reflected intensity I_{r} instead of the reflectivity since the error in the intensity is modeled as a (discrete) Poisson distribution and the error in the reflectivity is a (continuous) normal distribution. The expectation value exists only in the discrete case; the continuous case fails to yield a finite value as the integration is carried out over a pole of order 1. The measurable quantity Σ in equation (3.60) is calculated by $\Sigma = \frac{I_0+I_{\mathrm{r}}}{I_0-I_{\mathrm{r}}}$ where I_0 is the incident intensity such that $|R|^2 = {}^{I_{\mathrm{r}}}/_{I_0}$. The expectation of the error is (see appendix B.2 for the deviation)

$$E[\varepsilon_\Sigma] = \frac{1}{\mathrm{CDF}_{\mathrm{Pois}(I_{\mathrm{r}})}(I_0-1)} \sum_{j=0}^{I_0-1} \frac{I_{\mathrm{r}}^j e^{-I_{\mathrm{r}}}}{j!} \left(\frac{2I_0(j-I_{\mathrm{r}})}{(I_0-j)(I_0-I_{\mathrm{r}})} \right), \tag{3.61}$$

where $\mathrm{CDF}_{\mathrm{Pois}(I_{\mathrm{r}})}$ is the cumulative distribution function (CDF) of the Poisson distribution. The normalization term which includes the CDF is required because the reflected counts k cannot exceed the incident intensity $j < I_0$. The incident intensity I_0 acts here as the uncertainty or standard deviation parameter $\sigma_{|R|^2} = {}^1/\sqrt{I_0}$ when passing to the continuous case. The first term in the sum corresponds to the probability of measuring j counts if the mean is I_{r} assuming a Poisson distribution. The second term in the brackets is the distortion from the non-linearity caused by $\Sigma = \Sigma(I_{\mathrm{r}})$.

On the one hand, if the uncertainty in $\sigma_{|R|^2}$ is sufficiently small, the minimizer $\hat{\Theta}$ is usually overestimated for small reflectivities, i. e. $E[\varepsilon_\Sigma] > 0$. On the other hand, if the reflectivity is sufficiently close to the total reflection edge, the expected error $E[\varepsilon_\Sigma]$ is negative resulting in an underestimation of $\hat{\Theta}$. The reason for this behavior is that the symmetric error $\varepsilon_{I_{\mathrm{r}}}$ is asymmetrically cut as $|R(k)|^2 + \varepsilon$ has to be bounded by 1. See figure 3.19 for the cases of overestimation and underestimation. An overestimation and underestimation is indicated if the relative error is above zero and below zero, respectively.

The overestimation and underestimation is only problematic if the reflectivity is too close to the regime of total reflection, and usually both effects can be neglected for lower reflectivities or, equivalently, higher k values. For high reflectivities the practical approach is to increase the counting time in order to increase the accuracy of the reflectivity. Alternatively, an approximation of the expectation value might be subtracted from the estimated $\hat{\Sigma}$. However, as the true reflected intensity I_{r} is not precisely known, the expectation value can only be approximated and an improved $\hat{\Theta}$ can be achieved by replacing $\hat{\Sigma}$ with $\hat{\Sigma} - E[\varepsilon_\Sigma]$.

Figure 3.19 shows the relative error of $E[\hat{\Sigma}]$ as a function of reflectivity. The samples are drawn from a Poisson distribution instead of a normal distribution, because the normal distribution cannot be used as an approximation to the Poisson distribution for low intensities or rates. For high uncertainties or, equivalently, low maximal intensities, the estimated $\hat{\Sigma}$ can considerable deviate from the true Σ. With increasing incident intensity, the peak of the relative error is shifted closer to $|R|^2 = 1$. An incident intensity of 10^6 to 10^7 counts is not uncommon for reflectivity experiments, thus, only the reflection

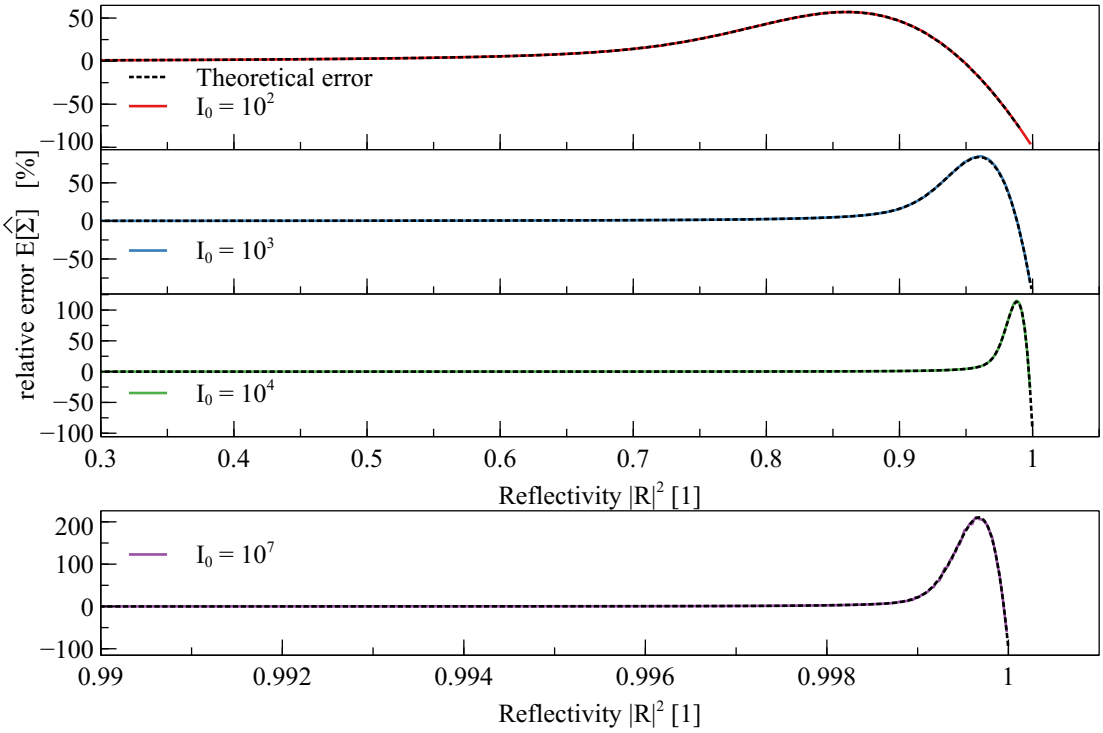

Figure 3.19: Relative error $\frac{E[\hat{\Sigma}]-\Sigma}{\Sigma}$ as a function of the reflectivity with varying incident intensities I_0 which influence the relative uncertainty of the reflectivity. $\hat{\Sigma}$ is drawn from a Poisson distribution with rate $\lambda = I_0|R|^2$ (not confuse with wavelength) using 10^6 samples. The dotted curves indicates the theoretical error calculated by equation (3.61), the solid lines are the randomly drawn samples. Both curves agree because of consistency. A relative error above zero indicates an overestimation of $\hat{\Sigma}$ whereas an underestimation happens if the relative error is below the horizontal line. Any deviation from zero corresponds to a bias of the estimator $\hat{\Sigma}$.

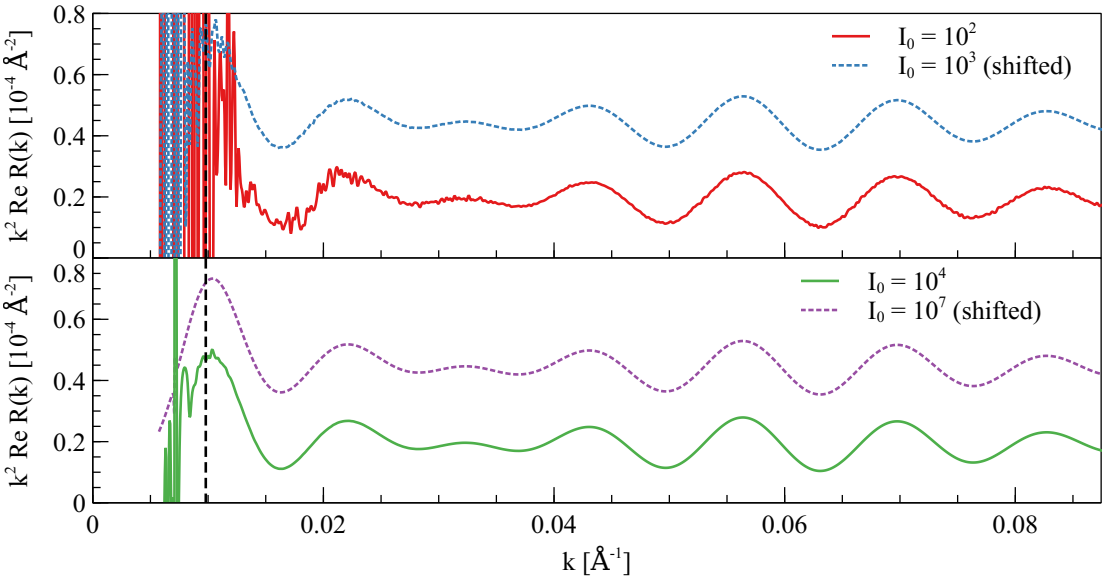

Figure 3.20: Real part of retrieved reflections using three simulated reflectivities with measurement errors. The curves are split into two groups and are shifted by 0.25 for reasons of clarity. The vertical dashed line is located at $k \approx 0.01\,\text{Å}^{-1}$ which corresponds to $|R(k)|^2 \approx 0.4$ in the simulated reflectivities.

close to the total reflection edge is distorted from measurement noise in the reflectivity. At reflectivities of $R \leq 0.4$ this effect has almost no relevance anymore even for incident intensities as low as $I_0 = 10^2$ counts.

The influence of the errors in the reflectivity on the retrieved reflection is shown in figure 3.20. The effect of measurement noise is most pronounced at small k values which correspond to high reflectivities. At higher k values the noise in the measurement becomes less relevant. Furthermore, with an increase in the incident intensity I_0 (lower uncertainty) the effect of random noise in the retrieved reflection becomes less significant. Thus, the reference layer method is well-suited for retrieving the reflection with noise degraded data. However, to retrieve the reflection close to the regime of total reflection, some care has to be taken to minimize the effect of noise degraded data.

To summarize, there are two sources of errors which especially affect the high reflectivity region. First, there is the measurement noise which distorts Σ such that small errors in the reflectivity cause large errors in the retrieved reflection, simply by the fact that $\frac{1}{x}$ behaves "badly" for $x \approx 0$ with measurement error ε_x. Secondly, the quantity Σ is biased which prevents to use arbitrary many measurements to improve an estimator $\hat{\Theta}$ for the reflection based on a linear least squares approach as this requires an unbiased error ε_Σ.

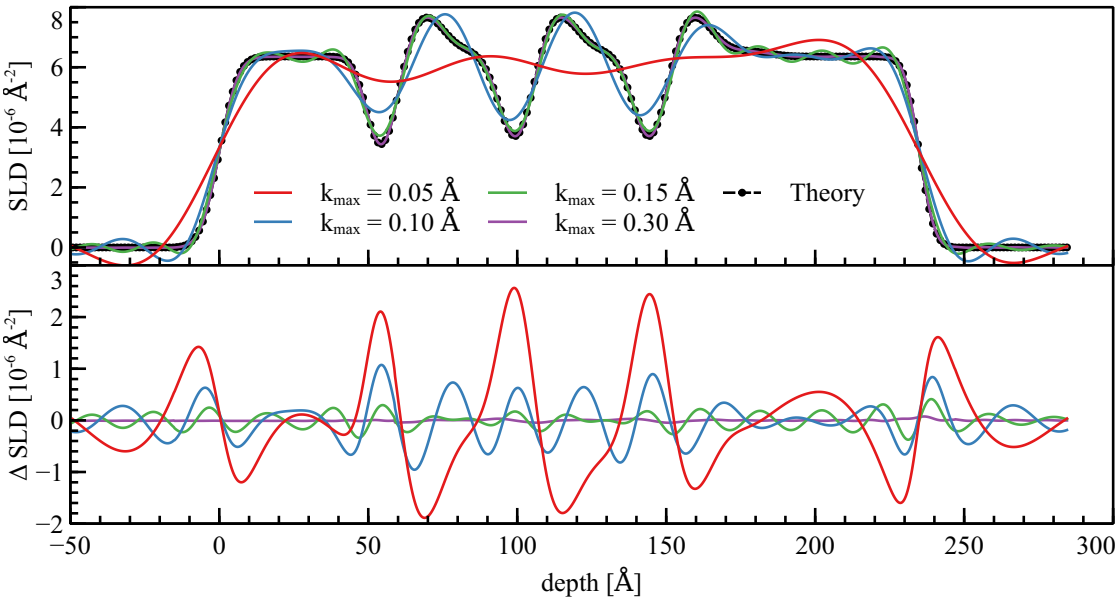

Figure 3.21: Effect of truncated reflection on the inverted scattering potential. The reflection was simulated using the theoretical SLD ($\sim V$) shown in the top graph. The top graph shows the inverted SLDs using the truncated reflection $\mathcal{T}_0^{k_{\max}} \circ \mathcal{R}[V]$. The bottom graphs depicts the difference of the SLD computed by $V - \mathcal{R}^{-1} \circ \mathcal{T}_0^{k_{\max}} \circ \mathcal{R}[V]$.

3.4.2 Bandwidth Limitation

The major issue when inverting the reflection to obtain the scattering potential is the limitation (or truncation $\mathcal{T}_0^{k_{\max}}$) in the available k range. As the reflectivity can only be measured up to a maximal $k_{\max}$ the resulting reflection is also truncated. Obviously, one cannot obtain the true scattering potential from truncated reflection data, i. e.

$$V \neq \mathcal{R}^{-1} \circ \mathcal{T}_0^{k_{\max}} \circ \mathcal{R}[V]. \tag{3.62}$$

It is thus important to analyze the influence of the truncation operator acting on the retrieved reflection.

The reflection inversion procedure exhibits similar features as a Fourier inversion, as the inversion relies on a Fourier transform shown in section 3.2. Thus, the truncation of high k values implants oscillations in the inverted scattering potential. The amplitude and frequency of these oscillations highly depend on $k_{\max}$. Figure 3.21 shows the effect of truncated reflection.

In the BA one can explicitly state the influence on the inverted potential $\hat{V}$ by [110]

$$\hat{V}(z) = \mathcal{T}_0^L \left[\int_{-\infty}^{\infty} \mathcal{K}_{k_{\max}}(z - \zeta) V(\zeta) \mathrm{d}\zeta \right], \tag{3.63}$$

where

$$\mathcal{K}_{k_{\max}}(z) = \frac{\sin 2k_{\max}z}{2k_{\max}z} = \operatorname{sinc} 2k_{\max}z \tag{3.64}$$

is the kernel of the convolution which is the sine cardinalis. Indeed, the truncation can be viewed as a simple convolution of the true scattering potential with the sine cardinalis. This result shows that the bandwidth limitation acts like a low-pass filter. In the limit $k_{\max} \to \infty$, the convolution kernel $\mathcal{K}_{k_{\max}}$ converges to the dirac delta function in the distributional sense. This explains why the complete knowledge of the reflection for *any* $k \in \mathbb{R}$ is not required for a practical inversion. Hence for a sufficiently large $k_{\max}$, one has

$$\mathcal{R}^{-1} \circ \mathcal{T}_0^{k_{\max}} \circ \mathcal{R}[V] \approx V. \tag{3.65}$$

In general, one can only give approximate values for $k_{\max}$ which produces sufficiently good inverted scattering potentials. A general rule of thumb is

$$k_{\max} = \frac{\pi}{d_{\min}}, \tag{3.66}$$

where $d_{\min}$ is the smallest layer size inside the sample. If the scattering potential contains for example sharp interfaces with no roughness $k_{\max}$ needs to be larger, if the scattering potential is smooth then $k_{\max}$ can be smaller than $\frac{\pi}{d_{\min}}$. The reason is that for smooth functions the Fourier transform decays quicker than for discontinuous functions.

The truncation effect is shown in figure 3.22 for three sample models which differ only by the roughness. One can clearly see that the truncation of the reflection has a lesser effect for rougher samples. The inversion with roughness $\sigma = 3\,\text{Å}$ (third column in figure 3.22) is already sufficient if the reflection is retrieved for $|k| \leq 0.75 k_{\max} \approx 0.236\,\text{Å}^{-1}$.

The difference of the inverted potential V_K to the true potential V as a function of K is shown in figure 3.23. Again, it shows that potentials with a higher roughness between layers can be better reconstructed with the same amount of "knowledge" of the reflection. Interestingly, for K between $0.16\,\text{Å}^{-1}$ and $\approx 0.25\,\text{Å}^{-1}$ the inverted potential V_K does not substantially improve the matching with the true potential V at least in the L^1 sense. In this context when planning an experiment at a beamline, it might be more beneficial to invest the valuable beamtime in e. g. lowering measurement noise instead of increasing the reflection domain k, since the additional reflection information does not significantly improve the inverted scattering potential, at least in this special case. It is, therefore, advantageous to investigate such a behavior prior executing PNR experiments to maximize the information output.

The bandwidth limitation has another interesting consequence which is similar to the Gibbs phenomenon [111]. The Gibbs phenomenon describes the fact that a finite Fourier series of a piecewise continuous function has large oscillations near jump discontinuities. The width of the oscillations decrease the more terms are added to the Fourier series, however, they do not vanish for any finite number of terms. In particular, the Fourier series will exhibit an overshoot right to a jump discontinuity and an undershoot left to

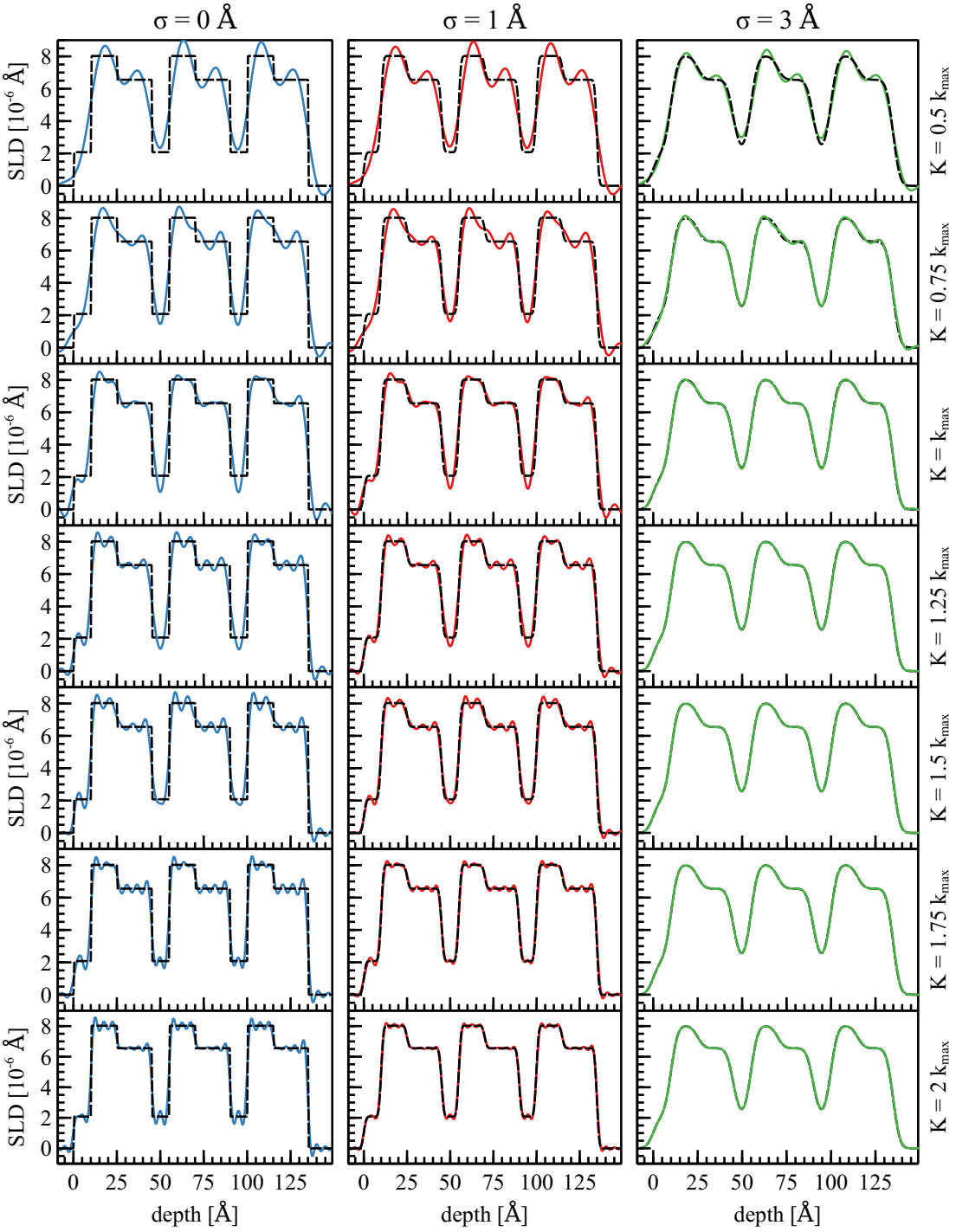

Figure 3.22: Inversion of a free-standing $[\mathrm{Al}(10\,\text{Å})/\mathrm{Fe}(15\,\text{Å})/\mathrm{Cu}(20\,\text{Å})]_3$ multilayer. Each column shows the true SLD (dashed curve) with roughness σ. Each row corresponds to a truncation of the reflection $R(k)$ for $0 \leq |k| \leq K$ with $k_{\max} \approx 0.314\,\text{Å}^{-1}$.

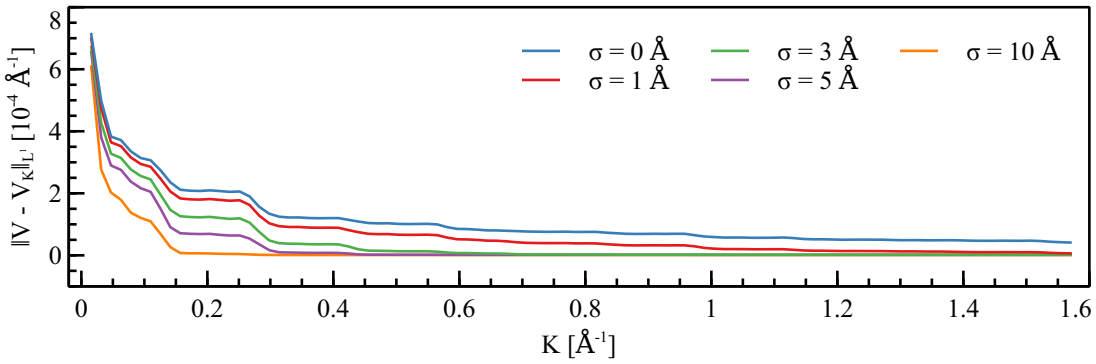

Figure 3.23: Difference of the true potential V to the inverted potential V_K as a function of the truncation quantity K and roughness σ measured in L^1. The potential V_K is calculated by $V_K = \mathcal{R}^{-1} \circ \mathcal{T}_0^K \circ \mathcal{R}[V]$. The potential V is a Al/Fe/Cu free-standing film, see figure 3.22.

a jump discontinuity. The truncated Fourier series has an overshoot or undershoot of

$$\frac{-1}{\pi} \int_{\pi}^{\infty} x^{-1} \sin(x) \mathrm{d}x = \frac{1}{\pi} \int_{0}^{\pi} x^{-1} \sin(x) \mathrm{d}x - \frac{1}{2} \approx 9\% \tag{3.67}$$

near a jump discontinuity [112–114]. This behavior can be seen in the inverted scattering potential as well, however, the relative overshoot and undershoot can vary between $\approx 6\%$ to $\approx 12\%$. This situation is exemplary shown in figure 3.24 where a 45 Å thick sample was used to show the overshoot and undershoot at the interface of two layers with zero interdiffusion or roughness.

Note that the feature of the overshoot and undershoot cannot be removed even when increasing the maximal k value. To remove this feature, the reflection over the complete k range has to be measured, i. e. $K = \infty$, which is not feasible.

In practice, the "ringing" usually does not exist inside the sample as perfectly sharp interfaces rarely exist, however, the "ringing" feature appears in regard to phase reconstruction by the reference layer method: As the whole sample is split into the unknown and reference part, a sharp interface is created there. In the context of *in situ* PNR by putting the reference layer on top of the sample, the ringing will thus appear at the interface of the top sample to the surrounding (air) in the scattering potential inverted from the reconstructed phase.

By extrapolating the reflection to higher q values the ringing effect can be reduced to an acceptable amount. The disadvantage with this approach is that a suitable extrapolation model has to be chosen. In section 4.2.2, an extrapolation has exemplarily been successfully carried out.

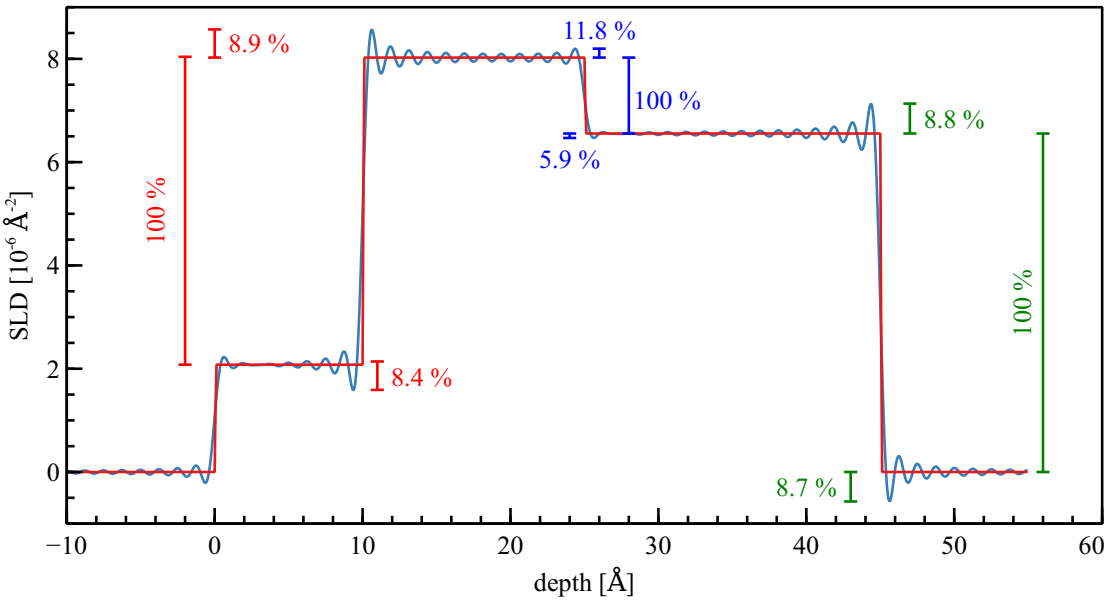

Figure 3.24: Overshoot and undershoot at jump discontinuities of the inverted scattering potential due to a bandwidth limitation $K = 5\,\text{Å}^{-1}$.

3.4.3 Resolution

The reflectivity used for the phase reconstruction is inevitable degraded by the resolution. The reflection will be degraded as well and one has

$$\text{Ret}\left[\left(\text{Res}\left[|R_i|^2\right], L_i\right)_{i=1}^{N}\right] \neq R. \tag{3.68}$$

The resolution in q is given by

$$\sigma_q = q\sqrt{\left(\frac{\sigma_\lambda}{\lambda}\right)^2 + \left(\frac{\sigma_\theta}{\tan(\theta)}\right)^2} \tag{3.69}$$

and the resolution of the reflectivity $\text{Res}\,|R|^2$ is computed by the convolution with a normal distribution $\mathcal{N}(0, \sigma_q)$ with mean $\mu = 0$ and standard deviation $\sigma = \sigma_q$ by

$$\text{Res}\left[|R|^2\right] = |R|^2 * \mathcal{N}(0, \sigma_q). \tag{3.70}$$

To evaluate the resolution effect on the reconstructed reflection and inverted SLD, the reflectivity is simulated first without including any resolution and then with a constant relative wavelength and constant relative angular resolution. The results are shown in figure 3.25. The main effect of the resolution on the reconstructed reflection is the damping of the oscillations accompanied by a slight decrease of the frequency. The decrease of the frequency causes the inverted SLD to be slightly thinner. The damping in the reflection overestimates the true SLD at the top surface (140 Å to 200 Å), where

as deeper inside the sample the SLD is underestimated (0 Å to 100 Å) until the substrate is overestimated again. The oscillations induced by the bandwidth limitation are not affected.

It is noted that the retrieval operator Ret and the resolution operator Res cannot be interchanged, i. e. none of the following reflections are equal

$$\mathrm{Ret}\left[(\mathrm{Res}\left[|R_i|^2\right], L_i)_i\right], \quad \mathrm{Res}\left[\mathrm{Ret}\left[(|R_i|^2, L_i)_i\right]\right], \quad \mathrm{Res}\left[|R|^2\right]. \tag{3.71}$$

Recall that $\mathrm{Ret}[(|R_i|^2, L_i)] = R$ holds, i. e. R is the true reflection reconstructed from the reflectivities $|R_i|^2$ and reference layers L_i. Especially, it is not possible to reconstruct the true reflection of the unknown sample from resolution degraded reflectivity data without further refinement of the measured reflectivity data. To see that the reflection mentioned above are not equal, figure 3.26 shows the corresponding reflectivities of each term. As the reflectivities do not match, the reflections and reflectivities cannot match either. The peak at $0.31\,\text{Å}^{-1}$ stems from a bad condition number in the constraint matrix (see section 3.3.2.1), which causes the imaginary part to diverge, independent of the applied resolution.

It is not yet clear how to optimally remove the resolution from the reflection data since a precise description of how the resolution of an instrument influences the reflection of the sample is not known. A naive idea would be to deconvolute the reflectivity and then retrieve the reflection. However, this approach did not yield any useful results as deconvolution is in general an ill-posed problem [115], especially if measurement noise is present in the reflectivity data.

3.4.4 Background

The background in reflectivity data plays an insignificant role when retrieving the reflection provided the background is constant for the various reflectivity measurements. For varying backgrounds the reflection can only be retrieved up to the q value where the background is substantially influencing the reflectivity, i. e. the background is of the same order of magnitude as the reflectivity or higher. More precisely, the following cases are considered

$$\begin{aligned} \text{constant background:} \quad & |\hat{R}_i(q)|^2 = |R_i(q)|^2 + B \\ \text{varying background:} \quad & |\hat{R}_i(q)|^2 = |R_i(q)|^2 + B_i \end{aligned} \tag{3.72}$$

with $B, B_i > 0$ being additive constants.

To understand why a constant background can be neglected in the context of phase reconstruction, consider the background $B > 0$ degraded quantity $\hat{\Sigma}_i$ (see section 3.3.2.1 for the definition of Σ) for small reflectivities $|R_i|^2 \ll 1$ and where the background

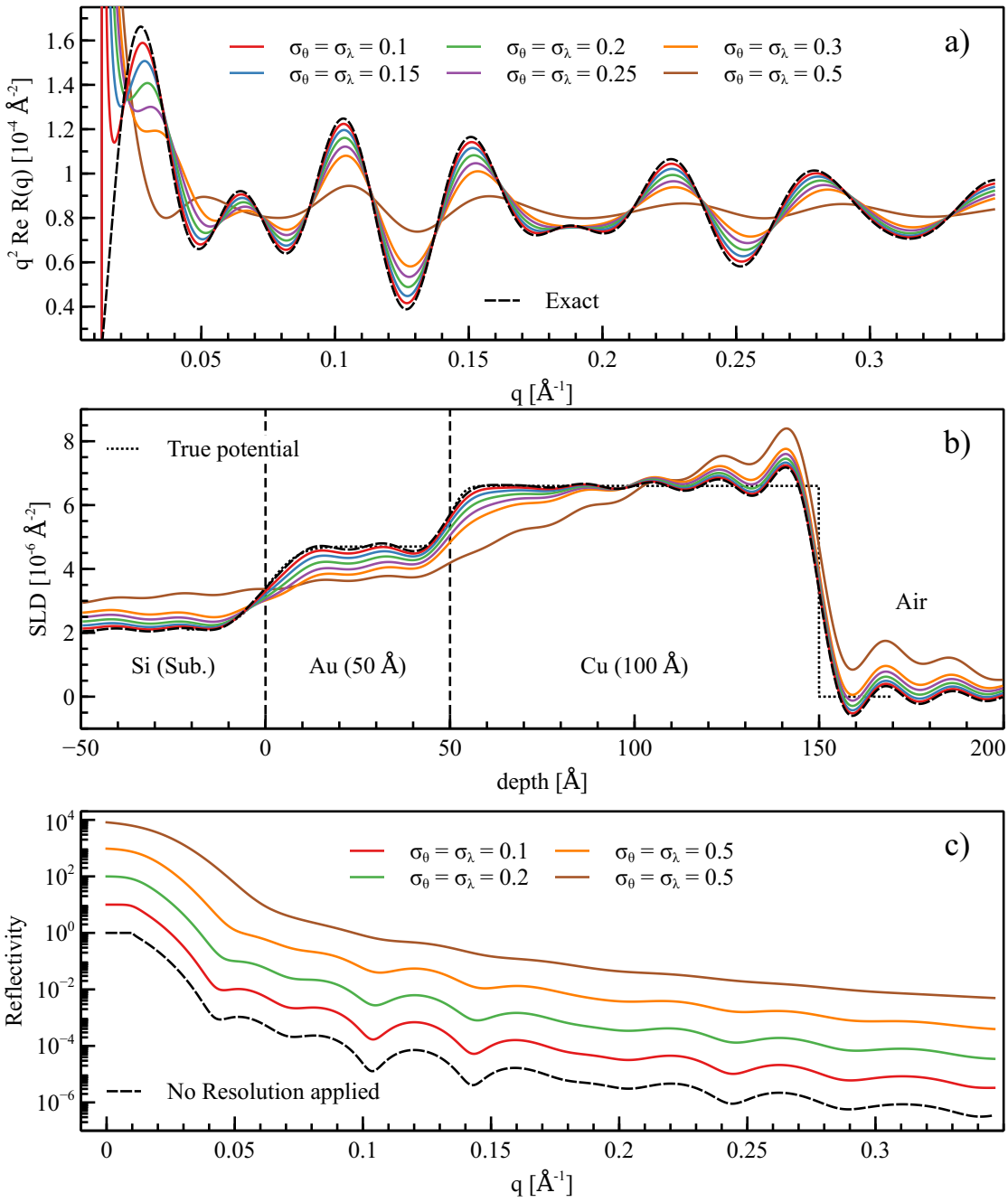

Figure 3.25: a) Reflection reconstructed from three reflectivities, which are degraded by the resolution operator Res with fixed angular divergence σ_θ and fixed σ_λ. b) The inverted SLD of the reflection shown above. The vertical lines indicate the Si/Au and Au/Cu interface, respectively c) The resolution degraded reflectivity used for the phase reconstruction. Only the reflectivities corresponding to one reference layer are shown.

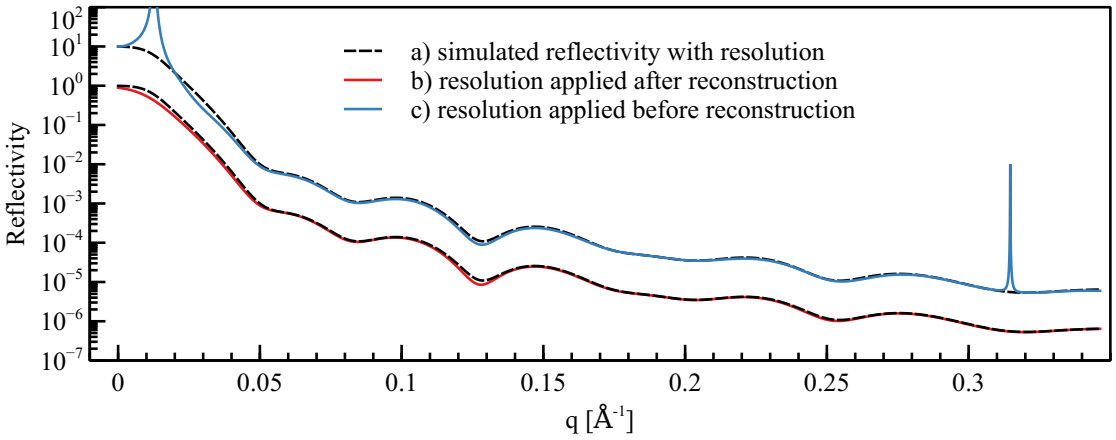

Figure 3.26: Comparison of the reflectivities after phase reconstruction with resolution $\sigma_\theta = \sigma_\lambda = 0.2$. a) shows the reflectivity as measured by a traditional reflectometry experiment $\mathrm{Res}\,|R|^2$. b) shows the reflectivity of the reconstructed reflection with perfect data and resolution applied afterwards $\mathrm{Res}[\mathrm{Ret}(|R_i|^2, L_i)_i]$. c) shows the reconstruction of resolution degraded reflectivity data $\mathrm{Ret}[(\mathrm{Res}(|R_i|^2), L_i)_i]$.

dominates the reflectivities. One can show that

$$\begin{aligned}\hat{\Sigma}_i = 2n_f n_b \frac{1+|R_i|^2+B}{1-|R_i|^2-B} &= \Sigma_i \left(1 + \frac{2B}{(1-|R_i|^2-B)(1+|R_i|^2)}\right) \\ &\approx \Sigma_i \left(1 + \frac{2B}{1-B}\right).\end{aligned} \tag{3.73}$$

Hence, the background degraded parameter vector $\hat{\Theta}_{\mathrm{U}}^{\mathrm{bb}}$, which uniquely determines the reflection, can be estimated by

$$\hat{\Theta}_{\mathrm{U}}^{\mathrm{bb}} = C_{\mathrm{K}}^{-1}\hat{\Sigma} \approx C_{\mathrm{K}}^{-1}\Sigma\left(1 + \frac{2B}{1-B}\right) = \Theta_{\mathrm{U}}^{\mathrm{bb}}\left(1 + \frac{2B}{1-B}\right), \tag{3.74}$$

where C_{K} is the constraint matrix and $\Sigma = (\Sigma_i)_{i=1}^{\mathsf{T}}$ is the transformed reflectivity vector. This result only holds if the background is independent of the reflectivity measurement. The background degraded reflection $\hat{R}$ is calculated by equation (3.38), which is

$$\hat{R} = -\frac{\hat{\alpha}-\hat{\beta}-2i\hat{\gamma}}{\hat{\alpha}+\hat{\beta}+2} \approx -\frac{\alpha-\beta-2i\gamma}{\alpha+\beta+\frac{2}{1+\frac{2B}{1-B}}} \approx R. \tag{3.75}$$

for a background B sufficiently small. It is noted that the background can be relatively large $0 \leq B \leq 10^{-2}$ without substantially distorting the reconstruction of the reflection, which is shown in figure 3.27. To put this into perspective, in PNR experiments the reflectivity is routinely measured to $|R|^2 \leq 10^{-5}$ and below [116–118].

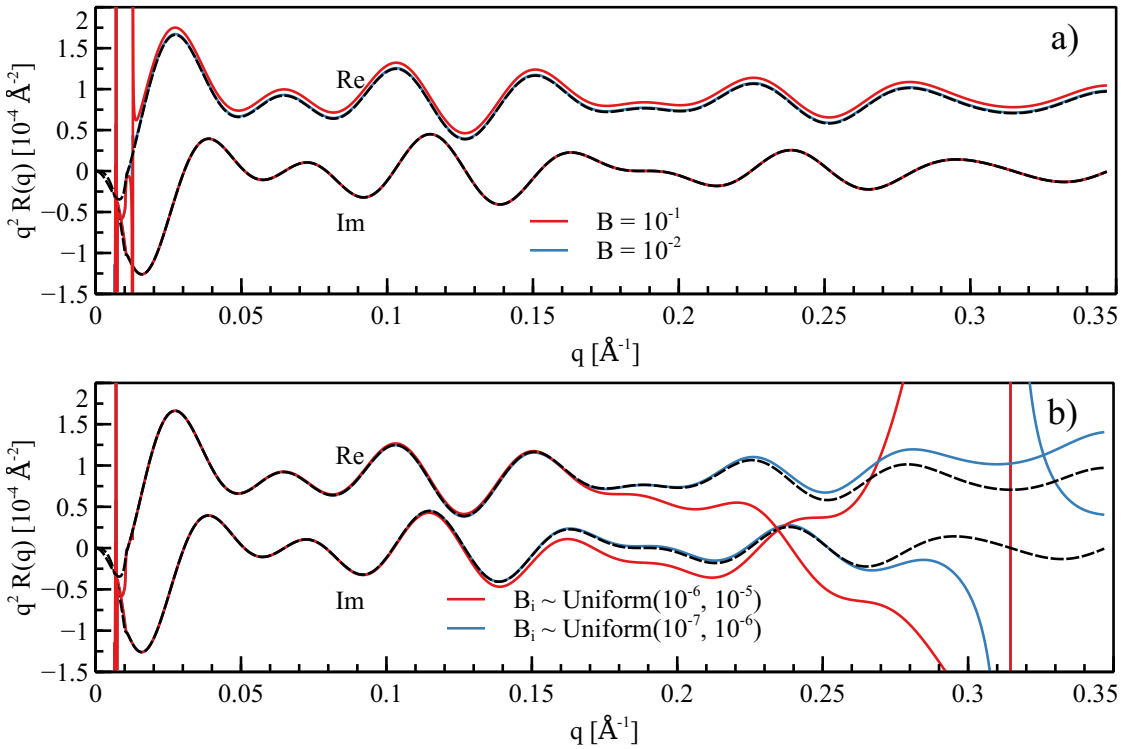

Figure 3.27: Influence of the background on the reconstructed reflection. The top graph a) shows a constant background B for each used reflectivity measurement, i. e. $R = \mathrm{Ret}[(|R_i|^2 + B, L_i)_i]$. b) depicts the case if the background is varying for each reflectivity curve and chosen from a uniform distribution.

However, if there is a variation in the background, the situation changes for the reconstructed reflection and it can only be reliably reconstructed as long as each reflectivity measurements is above the background level.

Figure 3.27 shows the two cases of the reconstruction: a) a constant background and b) a varying background in each reflectivity measurement drawn from a uniform distribution. On the one hand, one clearly sees that a constant background does change the reflection, and even for a high constant background $B = 10^{-1}$ there is only a small shift of $\approx 7 \times 10^{-6}\,\text{Å}^{-2}$ in the real part of the q^2 scaled reflection visible. On the other hand, the reflection reconstructed with a varying background exhibits tremendous deviations if the reflectivity is of the same order of magnitude as the background (indicated by the vertical dotted lines).

4 Phase Retrieval for in situ Polarized Neutron Reflectometry

In this chapter the phase retrieval and inverse scattering theory is applied for *in situ* polarized neutron reflectometry to recover a unique SLD profile of the inspected sample.

4.1 Experimental Setup

For retrieving the phase information, a compact *in situ* deposition chamber is used, which was designed by the University of Augsburg in cooperation with the Technical University of Munich [71, 72]. It allows PNR experiments to be performed while at the same time material can be deposited onto the sample.

The design of the chamber was gradually improved from the first version in 2010, which proved the feasibility of *in situ* PNR [72], to the current state, which e. g. incorporates a cryostat to allow the sample to be cooled or heated in a temperature range of 10 K to 1000 K [71, 119]. Further features of the *in situ* deposition chamber are (i) improved ultra-high-vacuum conditions with a base pressure below 5×10^{-9} mbar (ii) three $2''$ sputter guns operable in DC and RF mode which are rotated above the sample in order to maintain the sample's alignment and (iii) a fully automated deposition process with scripting capabilities which is integrated in the beamline control software.

As thin film deposition method magnetron sputter is applied in the *in situ* deposition system. In this process a inert gas, typically Ar, is inserted into the vacuum chamber by a leak valve in a controlled manner. The gas is then ionized to form a plasma whose ions are accelerated towards the sputter target. On impact of the ions, target material is released. This sputtered off material condenses on the sample. A shutter between the sample and sputter gun controls the amount of deposited material by the opening time of the shutter.

The *in situ* deposition chamber can be installed on any neutron reflectometer with a horizontal sample geometry, however, it is best suited for the Amor beamline at Swiss Spallation Neutron Source (SINQ), Paul Scherrer Institut (PSI), Switzerland, where a high neutron flux on the sample can be realized by applying the focusing Selene optics [120, 121]. The Selene optics is mounted in front of the *in situ* setup as shown in figure 4.1.

The neutron beam is polarized using a $m = 4.3$ Fe/Si multilayer polarizer and its polarization is selected by an rf spin flipper. Along the neutrons flight path, a magnetic guide field with permanent magnets are used to maintain the direction of the spin and the polarization of the neutron beam. Inside the *in situ* vacuum chamber, the guide field is

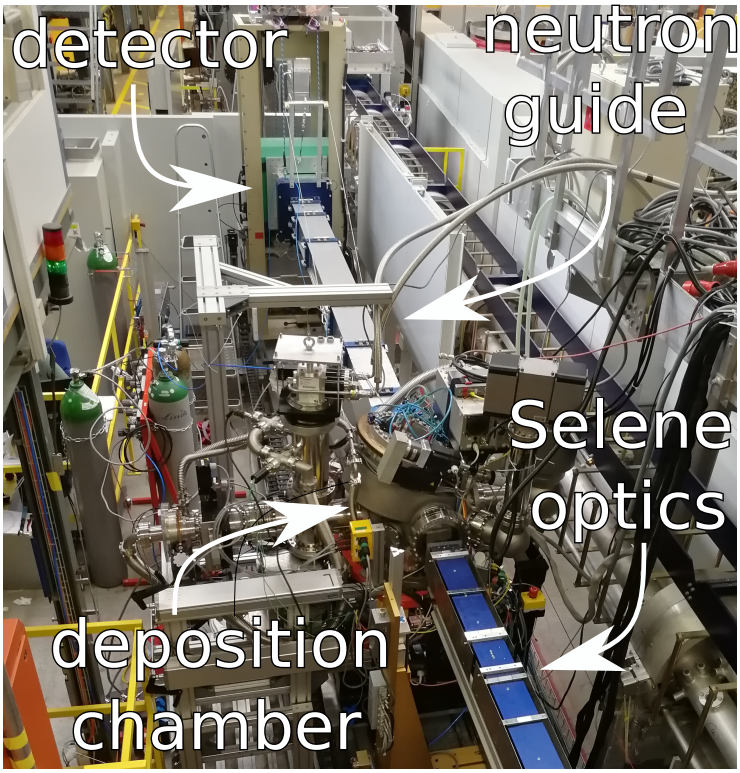

Figure 4.1: A photograph of the *in situ* deposition chamber installed on the Amor reflectometer beamline at PSI, Switzerland, in 2018.

maintained and at the sample position a magnetic field of 70 mT is applied perpendicular to the scattering plane by permanent magnets.

4.1.1 Sample Homogeneity

To create a sample with a homogeneous material distribution the sample is usually rotated around its surface normal while the sputtering gun is pointing at the sample at angle of 22.5° to the sample normal, however, the *in situ* vacuum chamber is designed such that the sample is kept aligned in the neutron beam at all time, incuding and in particular during deposition. Therefore, the sample might have an inhomogeneous layer thickness distribution, and care has to be taken when performing PNR experiments on *in situ* grown samples.

To assess the inhomogeneity of the sputtered samples in the *in situ* chamber, a SiO_2 specimen slide (76 mm × 26 mm ($x \times y$)) was cleaned with isopropyl alcohol and inserted into the vacuum chamber. The substrate was placed directly under one of the sputtering guns at a distance of approximately 11 cm which was loaded with a 1.5 mm thick 2″ Ni target with a purity of 99.99%. A slight misplacement of the sample with respect to the sputtering gun is due to the fact that the alignment was performed by eye.

The *in situ* sputtering chamber was then evacuated to a base pressure of $p_{\text{base}} = 4.7 \times 10^{-7}$ mbar. Prior to deposition, the target was pre-sputtered for 5 min to remove any oxidation or contamination on its surface. Subsequently, a nominally 200 Å thick Ni layer was deposited at room temperature using DC magnetron sputtering at a constant power of 50 W and an ultra-pure (7N) Ar sputtering gas at a pressure $p_{\text{sputtering}} = 6.5 \times 10^{-3}$ mbar, which corresponds to a deposition rate of 1.0 Ås^{-1}. The thickness of the Ni layer was controlled by the opening time of the shutter. The sputter time of 200 s was electronically controlled.

After deposition, the sample was analyzed *ex situ* in an x-ray reflectometer (D5000, Siemens GmbH). The reflectometer is operated in a $\theta - 2\theta$ geometry with parallel beam optics and uses a Cu tube with a characteristic wavelength $\lambda_{\text{Cu K}\alpha} = 1.5419\,\text{Å}^{-1}$. The sample was measured at 15 equidistant positions along the long side x, yielding a spacing of $\Delta x = 4.75$ mm. A knife edge was used to ensure a localized measurement of the sample's thickness.

The fitted x-ray reflectometry (XRR) curves and the resulting sample inhomogeneity is shown in figure 4.2. The fitting model is based on a SiO_2/Ni/NiO slab model where the NiO layer corresponds to a natural oxidation of the Ni layer. The total thickness of the XRR fits comprises the thicknesses of the Ni and NiO and it varies by ≈ 3 Å (1.3%) and ≈ 8 Å (3.8%) over a distance of 10 mm and 20 mm, respectively. The incident neutron beam on the sample at the Amor beamline at PSI has a beam width of at most 2 mm [120] which corresponds to a thickness inhomogeneity of $\approx 0.3\%$ along the short side y of the sample if a radial symmetric thickness distribution is assumed. Along the long side x, the incident neutron beam has a footprint < 10 mm. Hence, the inhomogeneity of the sample's thickness is negligible in both directions when performing PNR experiments at the Amor beamline.

4.2 Proof-of-Concept: Fe/Cu Thin Film

A 2 cm × 2 cm Si(001) substrate was cleaned by isopropyl alcohol and etched in a bath of 5% hydrofluoric acid, after which it was immediately placed into the *in situ* vacuum chamber. This treatment removes the native oxide layer and results in a hydrogen-terminated silicon surface, which restricts oxidation with ambient air [122]. The vacuum chamber was evacuated to a base pressure of $p_{\text{base}} < 5 \times 10^{-9}$ mbar and a 45 nm thick Cu seed layer was grown using DC magnetron sputtering. Fe reference layers were deposited with approximately monolayer thickness ($d = 2.6$ Å) in 28 repetitions, resulting in a ≈ 73 Å thick Fe layer. All deposition steps were carried out at room temperature. After each repetition, PNR measurements were carried out, but after the 14th repetition, only every second deposition is examined by PNR [123]. The resulting spin-up (+) and spin-down (−) reflectivity is denoted by $\mathcal{R}_i^{\pm}$, where i denotes the deposition step. Figure 4.3 shows the performed PNR measurements of the sample Si/Cu(450 Å)/Fe($i \times 2.6$ Å)/air [123].

The goal is to reconstruct the reflection of the unknown part of the sample, i. e. the Cu layer, by utilizing the thin Fe layers as reference. Before reconstructing the reflec-

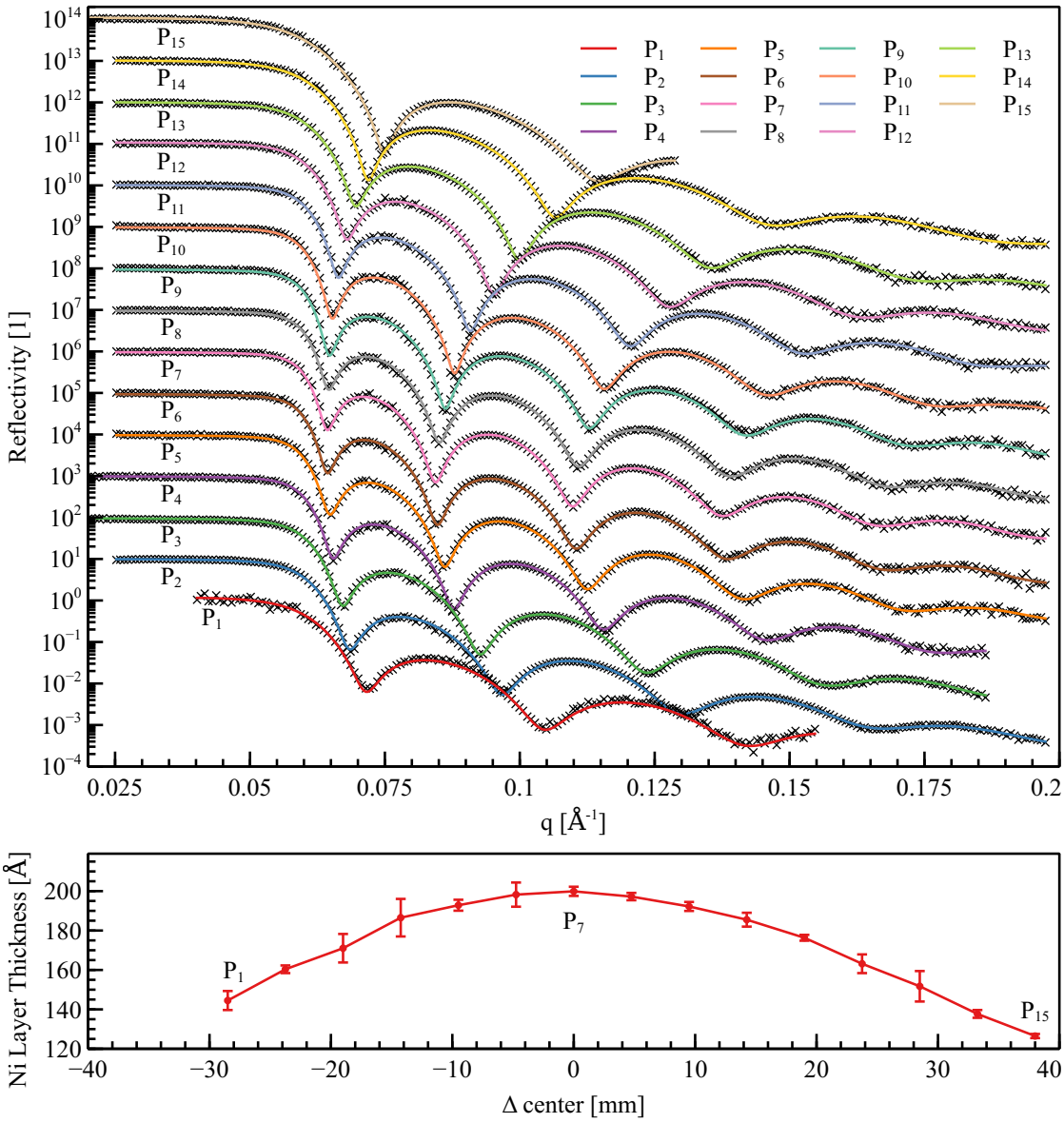

Figure 4.2: Thickness homogeneity of a single layer of Ni on SiO_2 specimen slide substrate. The top graph shows the XRR measurements (line cross) at equally spaced positions P_i together with their corresponding fits (solid line). The bottom graph shows the Ni layer thickness distribution as a function of measured position. The graph is shifted such that 0 corresponds to the maximal layer thickness at the center position below the sputtering gun.

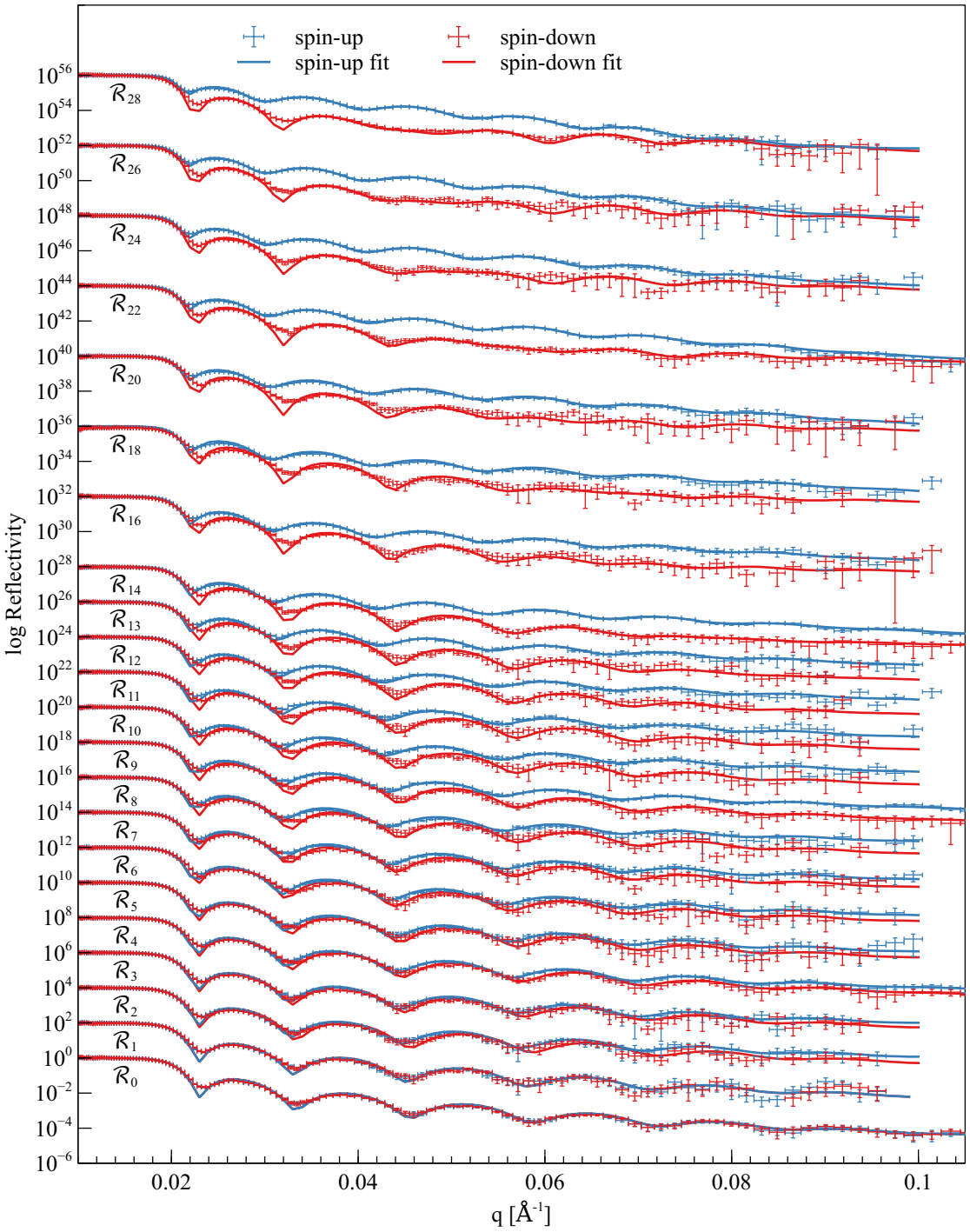

Figure 4.3: PNR curves $\mathcal{R}_i$ of the evolution the Si/Cu/Fe/air sample. The solid line shows the fitted reflectivity. Each reflectivity pair is vertically shifted by $2i$ orders of magnitude.

tion of the unknown part and inverting the reflection to obtain the SLD, the necessary requirements for the reconstruction and inversion are checked to ensure the feasibility.

The true SLD corresponding to the reflectivity measurement $\mathcal{R}_i$ is denoted by ρ_i and let ρ_i be split at a $z = z_\mathrm{s}$ into a unknown part ρ_u and a reference layer $\rho_{\mathrm{r},i}$ for each deposition step i, i. e.

$$\rho_i(z) = \begin{cases} \rho_\mathrm{u}(z), & z \leq z_\mathrm{s} \\ \rho_{\mathrm{r},i}(z), & \text{otherwise} \end{cases}. \tag{4.1}$$

The requirements for the reconstruction and inversion are:

1. The SLDs $\rho_\mathrm{u}, \rho_{\mathrm{r},i}$ are real valued for all i: All constituents of the sample, i. e. Si, Cu and Fe, have a bound scattering length b whose imaginary part is at least 7000 times smaller compared to the real part[1]. Thus the imaginary part is negligible and the SLDs are real valued.

2. The support of the SLD ρ_u is bounded from above, i. e. $\operatorname{supp} \rho_\mathrm{u} \leq b$: As the sample is a thin film, it is of finite extent regarding its top surface. Therefore, the support is bounded from above.

3. The SLD ρ_u has no bound states: The scattering length of Si, Cu and Fe are positive [14], thus $\rho_\mathrm{u} \geq 0$ and ρ_u cannot have a bound state by section 3.2.1.

4. The SLD ρ_u is constant for each PNR measurement $\mathcal{R}_i$: This feature is asserted by equation (4.1). Nevertheless, this property is worth to be explicitly mentioned.

4.2.1 Choice of Reference Layers

The reference layers can be arbitrarily chosen as long as the requirements for the reconstruction and inversion are fulfilled and the selected reference layer is precisely known. In the context of the Cu/Fe sample, only two special reference layer selections are physically reasonable. As the Fe reference layer is magnetic $\rho^+_{\mathrm{r},i} \neq \rho^-_{\mathrm{r},i}$ and due to the roughness between the reference layer and the underlying unknown part, one has to make sure that either

a) the splitting point z_s is selected such that $\rho^+_\mathrm{u} \neq \rho^-_\mathrm{u}$ and only one spin polarization is used for the reconstruction (see figure 4.4 and section 4.2.1.1) or

b) the splitting point z_s is selected such that $\rho^+_\mathrm{u} = \rho^-_\mathrm{u}$ and both spin directions are used for the reconstruction (see figure 4.5 and section 4.2.1.2).

Other selections of the reference layer are possible as well, but either require more *a priori* knowledge of the sample by shifting z_s more towards the Cu layer, i. e. shifting z_s to the left in figure 4.5, or do not allow to use all spin direction measurements by shifting z_s more towards the Fe layer, i. e. shifting z_s to the right in figure 4.4. Case a) reflects the

[1] The ratio $\frac{\operatorname{Re} b}{\operatorname{Im} b}$ is $88 \times 10^3, 13.6 \times 10^3$ and 7.6×10^3 for Si, Fe and Cu, respectively, when using $\lambda = 1.8\,\text{Å}$.

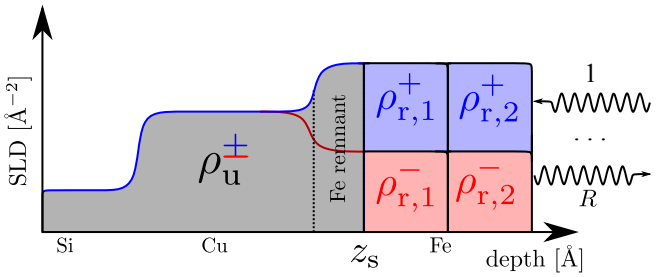

Figure 4.4: Case a): Schematic illustration of the selection of the splitting point z_{s} such that $\rho_{\mathrm{u}}^{+} \neq \rho_{\mathrm{u}}^{-}$. Only the reference layers $\rho_{\mathrm{r},i}^{+}$ can be used for reconstruction of ρ_{u}^{+}. Analogously, $\rho_{\mathrm{r},i}^{-}$ is the reference only for ρ_{u}^{-}.

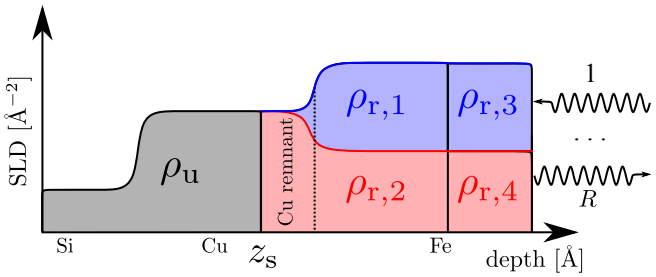

Figure 4.5: Case b): Schematic illustration of the selection of the splitting point z_{s} such that $\rho_{\mathrm{u}}^{+} = \rho_{\mathrm{u}}^{-}$. The references $\rho_{\mathrm{r},i}^{+} =: \rho_{\mathrm{r},2i+1}$ and $\rho_{\mathrm{r},i}^{-} =: \rho_{\mathrm{r},2i}$ can both be used to reconstruct ρ_{u}.

situation where the least amount of *a priori* knowledge is available, i. e. the interfacial roughness between Cu/Fe is not known, and case b) corresponds to the situation in which just enough knowledge of the Cu/Fe interface is given such that spin-up and down reflectivity measurements $\mathcal{R}_i^{\pm}$ can be used to reconstruct ρ_{u}.

The thickness is precisely controlled by the shutter system in the *in situ* deposition chamber, however, the parameters used for describing the SLD of the Fe reference layer were determined using a traditional fit [123] and as listed in table 4.1.

4.2.1.1 Remnant Fe Layer

The reflection reconstruction has to be separated based on the spin direction, since $\rho_{\mathrm{u}}^{+} \neq \rho_{\mathrm{u}}^{-}$ because the remnant Fe layer is included in the unknown sample, see figure 4.4. Furthermore, it is assumed that the SLD of the unknown sample at the Cu/Fe interface is not known. It is not possible to use all reflectivity measurements, since the roughness of the Cu layer prohibits the reflectivity measurements below deposition step $i = 14$ to be used $3\sigma_{\mathrm{Cu}} \approx 19\,\text{Å} \approx \frac{d_{14}}{2}$ (see table 4.1). To correctly determine $\rho_{\mathrm{r},i}$ for $i \leq 14$ the SLD of the unknown sample, i. e. the Cu/Fe interface, is required. Thus these deposition steps are ignored here. The SLD of the reference layers $\rho_{\mathrm{r},i}^{\pm}$ for $i = 16$ to $i = 28$ are depicted in figure 4.6 for the spin-up and down state.

Table 4.1: Fitted parameters of the Fe reference layer and of the unknown layer. From [123].

Name	thickness d [Å]	density ρ_{density} [g/cm^3]	roughness σ [Å]	magnetization M [μ_B/atom]
$\mathcal{R}_1$	6.3	3.07	3.1	0.13
$\mathcal{R}_2$	8.3	4.52	4.9	3.51
$\mathcal{R}_3$	10.6	5.26	4.5	1.74
$\mathcal{R}_4$	12.3	6.57	3.7	1.11
$\mathcal{R}_5$	13.9	6.87	4.8	1.19
$\mathcal{R}_6$	15.6	7.28	5.6	1.29
$\mathcal{R}_7$	17.5	7.36	6.1	1.23
$\mathcal{R}_8$	19.9	7.39	5.9	1.26
$\mathcal{R}_9$	23.5	7.06	7.4	1.40
$\mathcal{R}_{10}$	25.8	7.00	8.4	1.82
$\mathcal{R}_{11}$	28.3	7.06	9.5	1.85
$\mathcal{R}_{12}$	30.8	7.01	9.3	2.00
$\mathcal{R}_{13}$	33.8	6.98	9.5	1.98
$\mathcal{R}_{14}$	36.7	6.95	9.3	1.91
$\mathcal{R}_{16}$	40.6	7.05	10.1	1.98
$\mathcal{R}_{18}$	46.8	6.97	9.7	1.89
$\mathcal{R}_{20}$	52.5	6.94	8.7	1.92
$\mathcal{R}_{22}$	57.5	6.96	8.4	1.97
$\mathcal{R}_{24}$	61.7	7.01	7.5	1.93
$\mathcal{R}_{26}$	66.4	7.09	8.0	1.98
$\mathcal{R}_{28}$	70.3	7.16	11.0	2.03
	d [Å]	ρ_{density} [g/cm^3]	σ [Å]	SLD [10^{-6} Å^{-2}]
Cu	451	8.82	6.3	6.45
Si	∞	2.33	10.7	2.08

After applying the reconstruction method described in section 3.3.2.1, the reflection $\mathcal{R}[\rho_u^+]$ and $\mathcal{R}[\rho_u^-]$ are retrieved and shown in figure 4.7(top) and figure 4.8(top), respectively. The error bars are calculated by the propagation of errors using the covariance matrix of the linear least squares fit in equation (3.60). The extrapolated reflection (solid curve) shows the reflection at the total reflection edge for $q \leq 0.023\,\text{Å}^{-1}$. It is calculated using the method described in section 3.3.3. Between $z = 200\,\text{Å}$ and $z = 350\,\text{Å}$ the SLD of the unknown sample was set to the SLD of bulk Cu ($\rho_{\text{Cu}} = 6.554 \times 10^{-6}\,\text{Å}^{-2}$) to ensure the convergence of the algorithm.

The inverted SLDs of the unknown sample ρ_u^+ and ρ_u^- are shown in the bottom graph of figure 4.7 and figure 4.8, respectively. The inversion used the data points $\text{Re}\,R[\rho_u]$ together with the extrapolation at the total reflection edge. The errors in the SLD are estimated by the standard deviation of 5000 inversions, which are varied based upon the

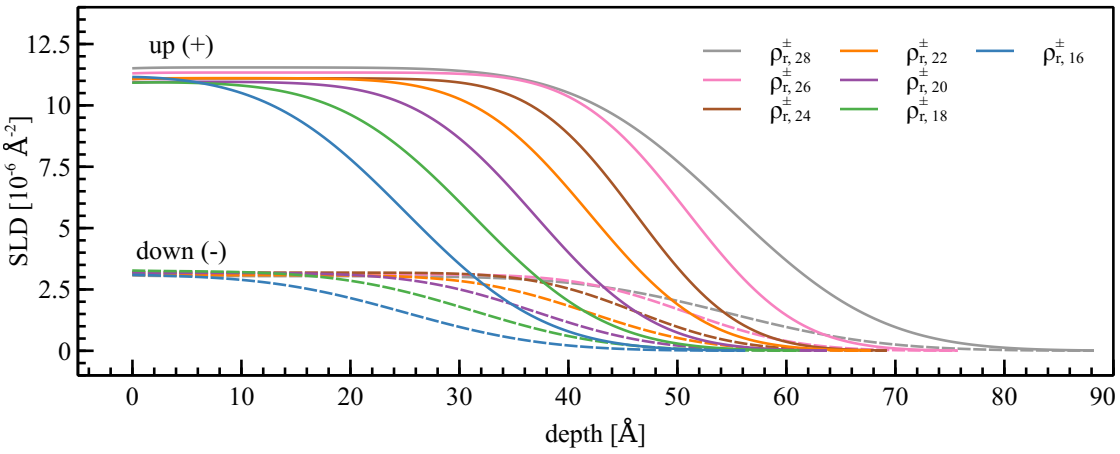

Figure 4.6: Reference layers $\rho^{+}_{\mathrm{r},i}$ and $\rho^{-}_{\mathrm{r},i}$ for reconstructing ρ^{+}_{u} and ρ^{-}_{u}, respectively. The reference layer $\rho^{\pm}_{\mathrm{r},i}$ are associated with the reflectivity measurement $\mathcal{R}^{\pm}_{i}$.

errors in the reflection and excluding possible uncertainties in the extrapolated low q reflection.

The real part of $\mathcal{R}[\rho^{+}_{\mathrm{u}}]$ and $\mathcal{R}[\rho^{-}_{\mathrm{u}}]$ both show good agreement with the expected reflection (dashed curve), which was calculated from the fitted model. The imaginary part, however, has a considerable disagreement with the expected reflection. Furthermore, the errors in the reflection $\mathcal{R}[\rho^{-}_{\mathrm{u}}]$ for $q \geq 0.7\,\text{Å}^{-1}$ are significantly larger compared to the errors of $\mathcal{R}[\rho^{+}_{\mathrm{u}}]$. This is due to the fact that the spin-down reflectivity decays faster compared to the spin-up reflectivity. On the one hand, the measurement uncertainty in the reflectivity originating from the background is more pronounced, which mainly influences the reflection in the high q region (shown in the analysis of a variable background in section 3.4.4). On the other hand, the errors in $\mathcal{R}[\rho^{-}_{\mathrm{u}}]$ are smaller than the errors in $\mathcal{R}[\rho^{+}_{\mathrm{u}}]$ for q close to the total reflection edge. This feature leads to smaller errors of ρ^{-}_{u} compared to ρ^{+}_{u}.

When comparing the two inverted SLDs, the spin-up case resembles the expected SLD better, even though the errors are higher. The worse phase information reconstruction in spin-down state can be attributed to this observation.

4.2.1.2 Combination of Spin-Up and Down

Assuming that the Cu/Fe interface is known, the spin-up and spin-down reflectivity measurements can be combined to reconstruct an improved reflection. The splitting point z_{s} is selected as shown in figure 4.5, which provides the necessary condition $\rho^{+}_{\mathrm{u}} = \rho^{-}_{\mathrm{u}}$.

The reference layers are shown in figure 4.9. The vertical dotted line indicates the virtual Cu/Fe interface with a roughness of $\sigma_{\mathrm{Cu}} = 6.3\,\text{Å}$. The reference layer includes a $3\sigma_{\mathrm{Cu}}$ thick Cu/Fe interface segment, which reduces the thickness of ρ_{u} by exactly 18.9 Å.

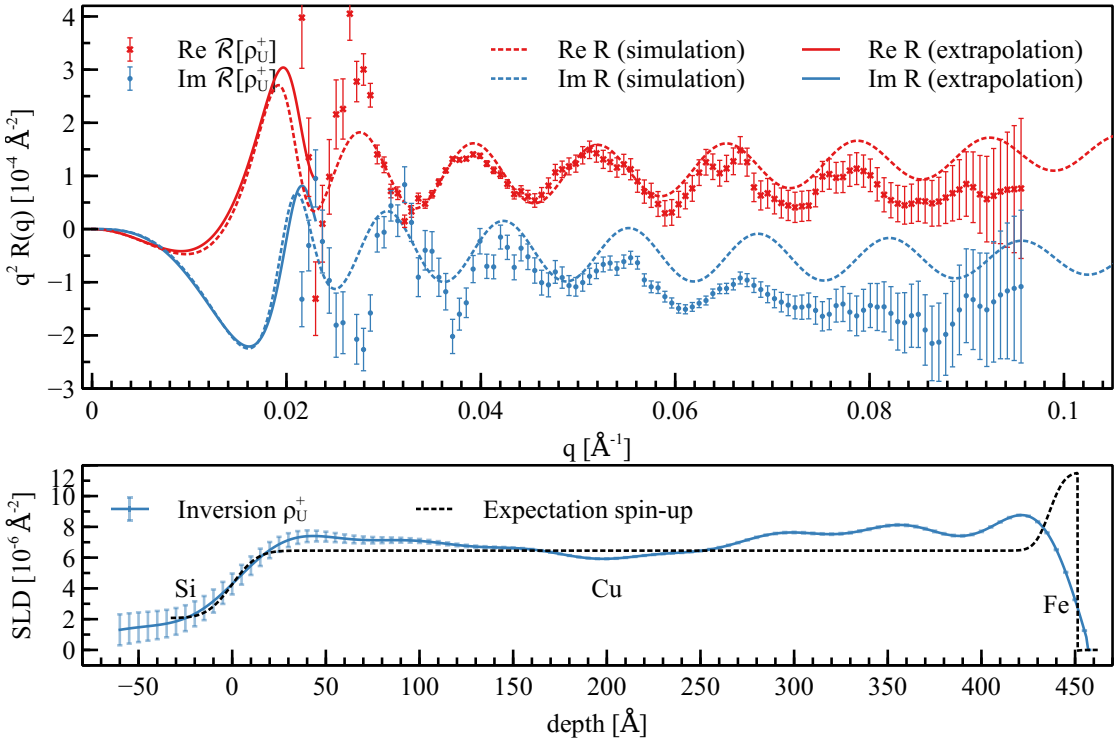

Figure 4.7: (Top) Scaled reflection of the unknown sample ρ_u^+ reconstructed from the reflectivity measurements $\mathcal{R}_i^+$ with $i \geq 16$. (Bottom) Inverted SLD ρ_u^+ using the reflection (with extrapolation) from the top.

The reflectivity measurements $\mathcal{R}_i$ for $i \geq 16$ are used in order to compare the results with the previous section 4.2.1.1.

The reconstructed reflection and the inverted SLD is shown in figure 4.10. The same methods and algorithms from section 4.2.1.1 are used here, except that the uncertainty in the reflection at the total reflection edge is estimated as well. These errors are estimated by the standard deviation of the low q retrieved reflection using 2000 normally drawn samples of the inverted reflection.

The usage of both spin directions results in an enhanced resemblance of the reconstructed SLD and the fitted SLD, if compared to previous results (see figure 4.7 and figure 4.7). Additionally, the noise and error bars in the reflection are significantly reduced.

The best reconstructed reflection is achieved by using all 42 reflectivity measurements $\mathcal{R}_i^{\pm}$, shown in figure 4.11. The reflection $R(q)$ is reconstructed on a larger q space ($q_c \approx 0.018\,\text{Å}^{-1} \leq q \leq 0.13\,\text{Å}^{-1}$), since a sufficient number of reflectivity measurements span it.

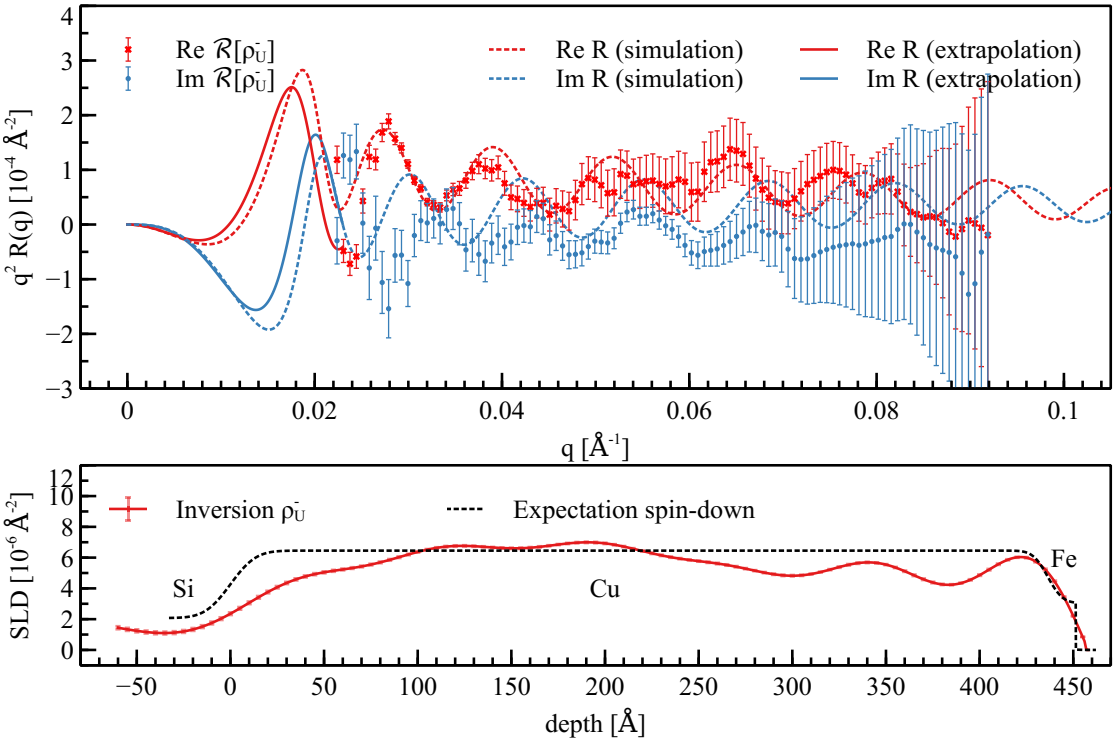

Figure 4.8: (Top) Scaled reflection of the unknown sample ρ_u^- reconstructed from the reflectivity measurements $\mathcal{R}_i^-$ with $i \geq 16$. (Bottom) Inverted SLD ρ_u^- using the reflection (with extrapolation) from the top.

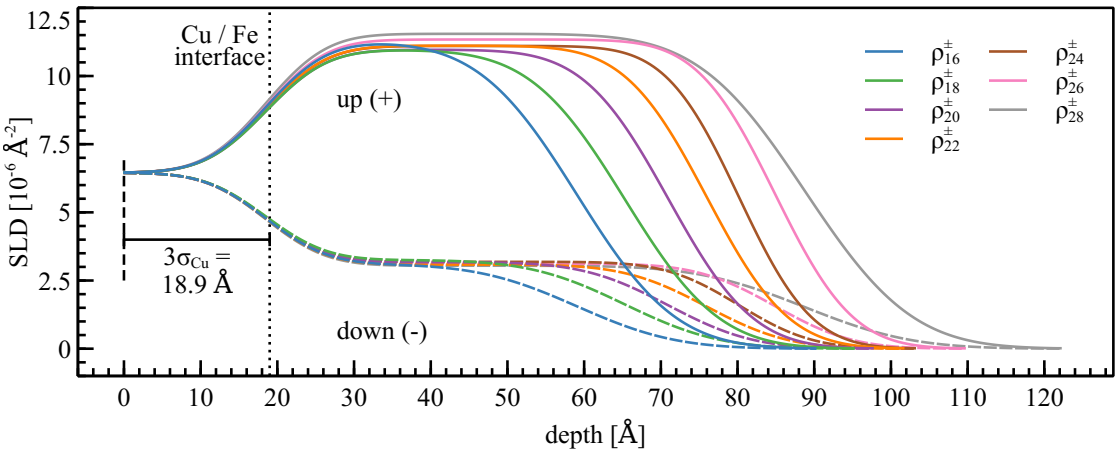

Figure 4.9: Reference layers for reconstructing ρ_u using both spin directions.

4.2.2 Reflection Extrapolation

The oscillations in the inverted SLD originate from the limited q range of the reflection [110]. The q truncation is the major reason which prohibits an even more precise

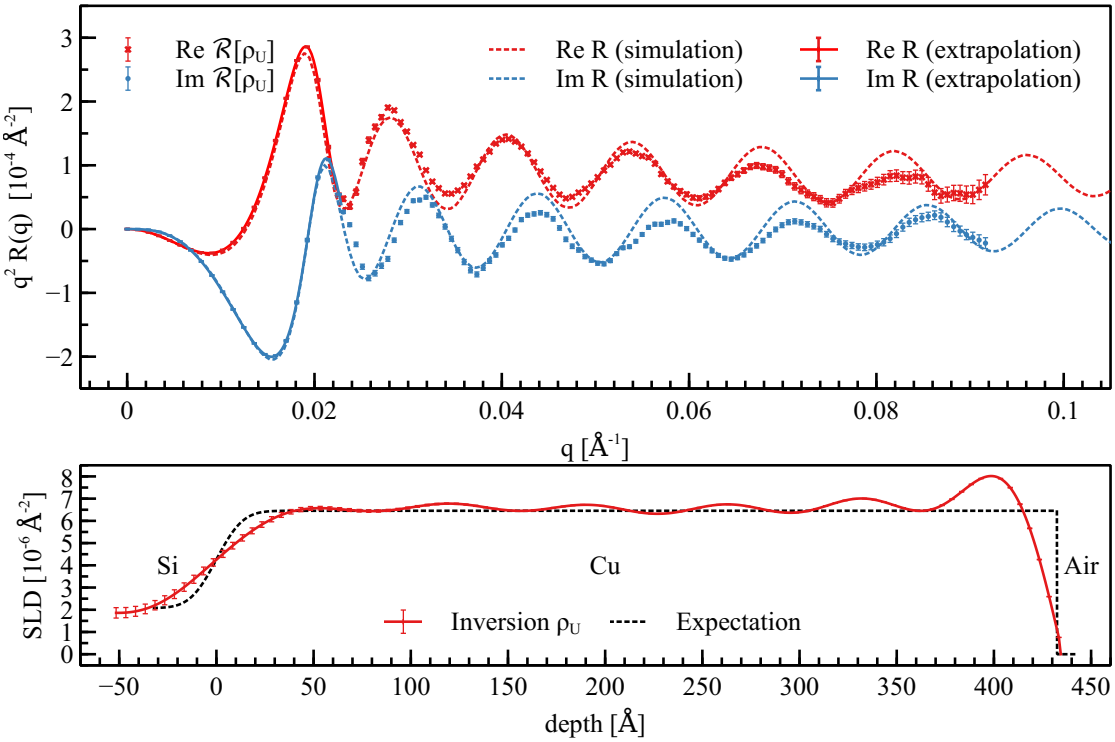

Figure 4.10: (Top) Scaled reflection of the unknown sample ρ_u reconstructed from the reflectivity measurements $\mathcal{R}_i$ with $i \geq 16$. (Bottom) Inverted SLD ρ_u using the reflection (with extrapolation) from the top.

potential inversion. To further eliminate these oscillations, the reflection $R(q)$ has to be known for larger q values, which might be possible by extrapolation with a suitable model function if no small structure features are present in the reflection as these would be visible in the high q range.

The extrapolation is carried out by fitting a model reflection to the data and evaluating it up to $q_{\max} = 5\,\text{Å}^{-1}$. The model function for the real part of the reflection is based on the BA and equation (2.45). It is heuristically selected assuming a single layer sample. It has the form

$$q^2 \operatorname{Re} R(q) = (4\pi\rho + a_1 q^{-1}) - \left(4\pi\rho_\Delta + \frac{a_0}{q - q_c}\right) \cos\left(qd + \phi_0 + \phi_1 q^{-1}\right) e^{-q^2\sigma^2}. \quad (4.2)$$

The parameters a_0, a_1, ϕ_0 and ϕ_1 are corrections terms and have no physical meaning. They are used to achieve a better fit as the model function is based on the BA. The remaining parameters are interpreted as follows: The quantity ρ corresponds to the SLD of Cu and ρ_Δ is the difference in the SLD of Cu and Si. The variable d is the thickness of the Cu layer, σ is the roughness of the Si/Cu interface and q_c corresponds to the critical wave vector.

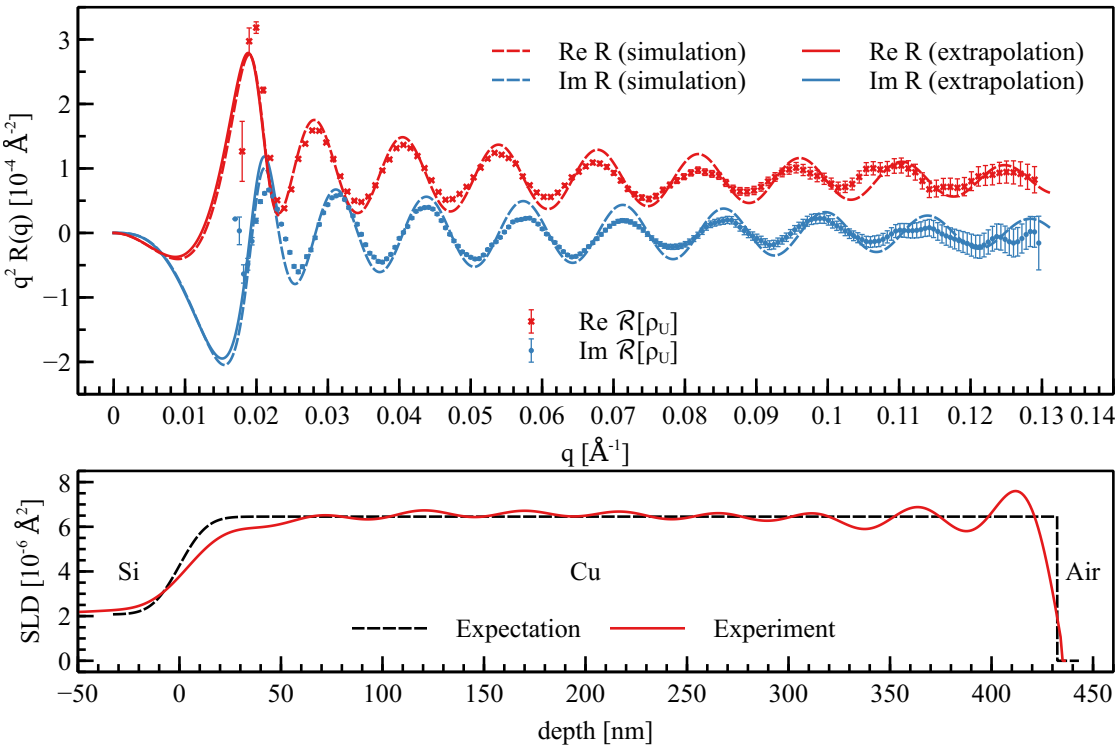

Figure 4.11: (Top) Scaled reflection of the unknown sample ρ_u reconstructed from all reflectivity measurements $\mathcal{R}_i$. (Bottom) Inverted SLD ρ_u using the reflection (with extrapolation) from the top.

The difference in the SLD leads to refraction of the neutrons and thus, the reflection depends on $\rho_{Cu} - \rho_{air} = \rho$ and $\rho_{Si} - \rho_{Cu} = -\rho_\Delta$. The first term in equation (4.2), which corresponds to the refraction at the Cu layer, does not contain any roughness smoothing as the reference layer method produces a sharp Cu/air interface. The second term contains the roughness smoothing $e^{-q^2\sigma^2}$ at the Si/Cu interface, the oscillations e^{iqd} caused by the Cu layer thickness and the refraction strength ρ_Δ.

The model is fitted to the reflection shown in figure 4.11. The optimal least-squares parameters and the expected values (obtained from the reflectivity fit) are shown in table 4.2. The fitted parameters match the expected parameters, but the SLDs of the Cu layer and Si substrate differ by $\approx 10\%$. As the reconstructed reflection contains the instrument resolution, the fitted roughness σ has to exceed the expected roughness, which is obtained by a traditional fit.

The reflection extrapolation is shown in figure 4.12(top) and it's inversion in the bottom graph. The inverted SLD shows an excellent agreement with the expected SLD, however, at the Si/Cu interface the two SLDs differ. The reason for the mismatch is the fact that the resolution has not been removed before reconstructing the reflection, but is included in the fitting model. The influence of the resolution is discussed in section 3.4.3, with findings supporting that claim. The sharp and narrow peak at the Cu/air interface

Table 4.2: Optimal least-squares fitting parameters for the reflection model (4.2) with $\chi^2_{\text{red}} = 1.38$. The errors correspond to the standard error $1-\sigma$, which are calculated from the covariance matrix.

Symbol	Fit	Expectation	Unit
d	433 ± 2	433	Å
σ	12.2 ± 0.4	10.7	Å
ρ	5.82 ± 0.04	6.45	$10^{-6}\,\text{Å}^{-2}$
ρ_Δ	3.94 ± 0.28	4.38	$10^{-6}\,\text{Å}^{-2}$
q_c	0.019 ± 0.001	0.018	Å^{-1}
a_0	$(1.5 \pm 0.4) \times 10^{-7}$	-	-
a_1	$(7.8 \pm 0.2) \times 10^{-6}$	-	-
ϕ_0	$(0.12 \pm 0.03)\,\pi$	-	-
ϕ_1	$(-9.3 \pm 0.2) \times 10^{-2}$	-	-

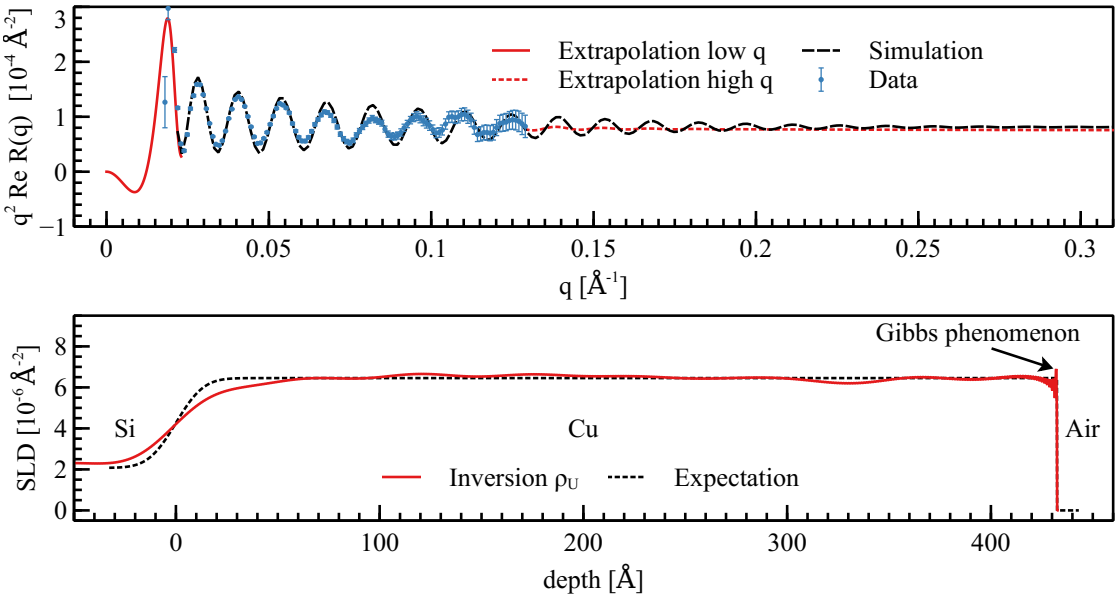

Figure 4.12: (Top) Scaled reflection of the unknown sample ρ_u reconstructed from all reflectivity measurements $\mathcal{R}_i$ and extrapolated using model equation (4.2). (Bottom) Inverted SLD ρ_u using the reflection (with extrapolation) for $0 \leq q \leq 5\,\text{Å}^{-1}$.

in figure 4.12 is due to the Gibbs phenomenon [111] originating from the discontinuity of the SLD at the interface.

4.2.3 Discussion

It is possible to use monolayers of Fe as reference layers to successfully retrieve the reflection. The choice of the reference layer, however, influences the quality of the reflection dramatically. For example, using only spin-down reflectivity measurements results in an unsatisfactory reflection and inverted SLD if compared to using only spin-up reflectivity measurements. The large error in the measured spin-down reflectivity $\mathcal{R}^-$ is suspected to be the major contribution for the poor reflection reconstruction. Especially the low signal-to-noise ratio of the spin-down reflectivity measurements cause high uncertainties in the retrieved reflection at high q values (see figure 4.8), since the background is of the same order of magnitude as the measured reflectivity (see figure 4.3).

These problems are mitigated when using only spin-up reflectivity as the background is less affecting the reflectivity even at high q values. The inverted SLD shows in general a reasonable agreement with the expected slab model (see figure 4.7), except at the remnant Fe layer at a depth of 400 Å to 450 Å.

A further improvement of the reflection is achieved by combining spin-up and down reflectivity $\mathcal{R}^\pm$ measurements. The major problem with this approach is the knowledge of the unknown parameters of the Cu/Fe interface, which are basically the information that are to be determined from the experiment. Nonetheless, the accuracy of the reconstructed reflection is substantially improved when using both spin direction measurements (see figure 4.10). Two factors play an important role: First, a higher contrast between the spin-up and down reference SLDs is achieved due to the magnetic references. Second, the number of reflectivity measurements, which are used for the reconstruction, is doubled. The major factor for the improved reconstruction is, however, the higher contrast between spin up and down reflectivities. If a single spin-down measurement replaces a spin-up measurement (or vice-versa) the reconstruction is dramatically improved. It is noted, that the extrapolation at the total reflection edge is almost perfectly matching the expected reflection, compared to the single spin channel case. The inverted SLD shows a good resemblance with the expectation. The deviation at the Si/Cu interface, which appears as a higher roughness, is attributed to the resolution in the reflectivity.

The extrapolation of the reflection to high q smoothens the oscillation in the SLD and a better matching with the expectation at the Cu layer is achieved. At a depth of $z = 20$ Å a mismatch of 10% in the SLD is observable, indicating a decrease in the density near the Si/Cu interface.

The structural parameters of the inverted SLD, obtained using the various reference layers, are compared with the parameters obtained from traditional data fitting in table 4.3. The displayed densities are calculated by the average SLD and the roughness is estimated by approximating the inverted SLD with the inversion of a model reflection[2]. Additionally, the fitted Cu layer thickness was reduced by $3\sigma_{\mathrm{Cu/Fe}} \approx 19$ Å to compensate for the Cu/Fe interface thickness (see figure 4.9). It is noted that the parameters

[2] Another approach to estimate the roughness is to calculate the FWHM of $\frac{\partial}{\partial z}\rho_{\mathrm{u}}$ at the interface. However, this method does not take the q truncation into account which influences the shape of the inverted SLD at the interface as well

Table 4.3: Overview of the extracted layer parameters for the various reference layer selections.

Method	Si		Cu	
	ρ_{density} [g/cm^3]	σ [Å]	ρ_{density} [g/cm^3]	d [Å]
Only spin-up	2.01	24.1	9.63	427
Spin-up & down	2.20	17.7	8.93	426
Extrapolation	2.57	12.3	8.83	431
Expectation / traditional fit	2.33	10.7	8.82	432

in table 4.3 should only be used for comparison and they do not suffice for parameters of a slab model. Instead, the full SLD profile as shown in e. g. figure 4.12 must be used.

The thickness of the Cu layer obtained by reflection inversion is consistent with the fitted parameter. In particular, the thickness of the extrapolated reflection differs only by 1 Å to the fitted thickness. The density of the Cu layer agree with the values reported in the literature for the spin-up & down and extrapolation case.

The density of the Si substrate is $\approx 10\%$ too high for the extrapolation method. The discrepancy is explained by the fact that the extrapolation parameters of the SLD (see table 4.2) have a mismatch (10%) to the expectation, which indicates an imperfect model function for the extrapolation.

The roughness and interdiffusion cannot reliably be inferred from the inverted SLD. This is an inherent problem as the resolution degrades the reflectivity which results in unusual high roughnesses/interdiffusion at interfaces (see section 3.4.3).

5 Conclusion and Outlook

The theory of phase-sensitive *in situ* polarized neutron reflectometry (PNR) was developed and applied in this thesis. It was proven that the *in situ* deposition with PNR measurements are capable to uniquely determine the complex reflection coefficient. The results demonstrate that the quality of the reconstructed reflection is excellent to obtain an inverted scattering length density (SLD).

An introduction to the state-of-the-art reflectivity data analysis was presented. In particular, the statistical analysis using Bayesian interference was applied to neutron and x-ray reflectometry. It was shown that the fitted parameters have to be critically assessed as the fitting program returns optimal parameters which depend on the used objective function. Indeed, it was shown that the statistically correct objective function χ^2 (MSWE) can yield insufficient optimal fit in some situations.

As every reflectivity measurement is always degraded by the measurement process, e. g. resolution, Poisson noise or background, the effect on the reconstructed reflection was investigated. The resulting degraded scattering potential was also studied. The main conclusions thereof are: The resolution causes a damping in the amplitudes of the reconstructed reflection. The damping results in an increased roughness in the inverted SLD. Apart from this, random measurement noise only affects the reconstructed reflection close to the total reflection edge where a high deviation is observable. The bandwidth limitation (because of the restricted q measurement range) causes oscillations in the inverted SLD which may be removed by extrapolating the reflection. The background in the reflectivity plays a minor role in the reconstruction of the reflection: a constant background can basically be ignored and only a non-constant background influences the reflection in a non-linear manner.

The reference layer method cannot retrieve the reflection (or phase) below the total reflection edge. Hence, a fixed-point algorithm to determine the reflection in this region was developed. The algorithm now allows a complete model-free evaluation of phase-sensitive PNR data, which was previously not possible as the reflection was estimated using a model of the sample. As the computational requirements are easily met with widely available computers, the analysis is drastically simplified. A straightforward and sufficient condition for the convergence of the algorithm based on the total film thickness was given. The algorithm was verified with two simulated examples, which are based on a realistic thin film (200 Å) and a randomly generated sample (330 Å). It was additionally tested on real data (chapter 4) and all its applications have shown an excellent accuracy. Even if the prerequisites are not given, a satisfactory result can be achieved if the algorithm converges.

A successful phase reconstruction was carried out on experimental data of a magnetic Cu/Fe thin film. The magnetic Fe layers were used as reference layers, which resulted

in a overall impressive agreement with the parameters obtained by traditional fitting methods. For example, the deviation in the Cu layer thickness and density is 1 Å (0.2%) and 0.01 g/cm^3 (0.1%), respectively. The choice of the reference layers, however, influences the retrieved reflection. It was identified that the contrast of the reference layer plays a crucial role therein. Reference layers which differ in approximately a single Fe layer are theoretically possible to use, but a larger contrast, i. e. spin-up vs. spin-down, is advantageous in practice. The best result was obtained by extrapolating the reflection to larger q in order to eliminate the effect of bandwidth limitation.

It was shown that *in situ* PNR is perfectly suited to retrieve the missing phase information and to retrieve a unique nuclear sample description. In particular, by variation of the magnetic state (with respect to the neutron spin polarization) and variation of the thickness of the reference layers, the phase is reconstructed with an impressive accuracy. However, the benefit of using the *in situ* growth technique is the ability to retrieve not only the non-magnetic components of a sample, but also the magnetic components by non-magnetic reference layer, whose thickness is varied. It is thus an ideal tool to probe the depth resolved magnetism in thin films.

The analysis showed that the resolution in reflectivity data lowers the accuracy of the reconstructed reflection. It showed that the roughness or interdiffusion at interfaces is significantly higher compared with results obtained by traditional fits. A sophisticated deconvolution method applied to the reflectivity prior to reconstruction might improve the reconstructed reflection. The difficulty here is that deconvolution is a highly ill-conditioned method, especially if the resolution convolution is based on a gaussian kernel [124]. A more in-depth analysis of the resolution effect should be carried out to quantitatively describe the degradation of the reconstructed reflection and to alleviate the effect using mathematical operations.

Another interesting research topic is the combination of reflectometry with information theory. Basically, there is no constraint on the shape of the reference layer used to retrieve the phase information, however, noisy reflectivity data or uncertainties in the true shape of the reference layer degrade the reconstructed reflection. It is thus reasonable to grow reference layers which result in the highest possible information gain of the reconstructed reflection. For example, a high contrast between spin-up and spin-down reference layers dramatically improves the reconstructed reflection, see section 4.2.1.2. A thorough investigation on optimizing the information gain by using more suitable reference layers should be performed. Similar approaches have already been realized in optimizing the information gain in contrast matching procedures [125, 126].

Bibliography

[1] M. N. Baibich, J. M. Broto, A. Fert, F. Nguyen Van Dau, F. Petroff, P. Etienne, G. Creuzet, A. Friederich, and J. Chazelas. Giant Magnetoresistance of (001)Fe/(001)Cr Magnetic Superlattices. *Physical Review Letters*, 61(21):2472–2475, 1988. doi:10.1103/PhysRevLett.61.2472.

[2] G. Binasch, P. Grünberg, F. Saurenbach, and W. Zinn. Enhanced magnetoresistance in layered magnetic structures with antiferromagnetic interlayer exchange. *Physical Review B*, 39(7):4828–4830, 1989. doi:10.1103/PhysRevB.39.4828.

[3] T Miyazaki and N Tezuka. Giant magnetic tunneling effect in Fe/Al_2O_3/Fe junction. *Journal of Magnetism and Magnetic Materials*, page 4, 1995. doi:10.1016/0304-8853(95)90001-2.

[4] S. Ikeda, J. Hayakawa, Y. Ashizawa, Y. M. Lee, K. Miura, H. Hasegawa, M. Tsunoda, F. Matsukura, and H. Ohno. Tunnel magnetoresistance of 604% at 300K by suppression of Ta diffusion in CoFeB/MgO/CoFeB pseudo-spin-valves annealed at high temperature. *Applied Physics Letters*, 93(8):082508, 2008. doi:10.1063/1.2976435.

[5] I. Barsukov, Yu Fu, C. Safranski, Y.-J. Chen, B. Youngblood, A. M. Gonçalves, M. Spasova, M. Farle, J. A. Katine, C. C. Kuo, and I. N. Krivorotov. Magnetic phase transitions in Ta/CoFeB/MgO multilayers. *Applied Physics Letters*, 106(19):192407, 2015. doi:10.1063/1.4921306.

[6] S. Ikeda, K. Miura, H. Yamamoto, K. Mizunuma, H. D. Gan, M. Endo, S. Kanai, J. Hayakawa, F. Matsukura, and H. Ohno. A perpendicular-anisotropy CoFeB–MgO magnetic tunnel junction. *Nature Materials*, 9(9):721–724, 2010-09. doi:10.1038/nmat2804.

[7] S. A. Wolf. Spintronics: A spin-based electronics vision for the future. *Science*, 294(5546):1488–1495, 2001. doi:10.1126/science.1065389.

[8] Shinji Yuasa, Taro Nagahama, Akio Fukushima, Yoshishige Suzuki, and Koji Ando. Giant room-temperature magnetoresistance in single-crystal fe/MgO/fe magnetic tunnel junctions. *Nature Materials*, 3(12):868–871, 2004. doi:10.1038/nmat1257.

[9] Hartmut Zabel, Ralf Siebrecht, and Andreas Schreyer. Neutron reflectometry on magnetic thin films. *Physica B*, page 5, 2000. doi:10.1016/S0921-4526(99)01469-6.

[10] G. P. Felcher. Neutron reflectometry as a tool to study magnetism (invited). *Journal of Applied Physics*, 87(9):5431–5436, 2000. doi:10.1063/1.373365.

[11] H. Béa, M. Bibes, F. Ott, B. Dupé, X.-H. Zhu, S. Petit, S. Fusil, C. Deranlot, K. Bouzehouane, and A. Barthélémy. Mechanisms of exchange bias with multiferroic BiFeO 3 epitaxial thin films. *Physical Review Letters*, 100(1):017204, 2008. doi:10.1103/PhysRevLett.100.017204.

[12] E. A. Karhu, S. Kahwaji, M. D. Robertson, H. Fritzsche, B. J. Kirby, C. F. Majkrzak, and T. L. Monchesky. Helical magnetic order in MnSi thin films. *Physical Review B*, 84(6):060404, 2011. doi:10.1103/PhysRevB.84.060404.

[13] M. N. Wilson, E. A. Karhu, D. P. Lake, A. S. Quigley, S. Meynell, A. N. Bogdanov, H. Fritzsche, U. K. Rößler, and T. L. Monchesky. Discrete helicoidal states in chiral magnetic thin films. *Physical Review B*, 88(21):214420, 2013. doi:10.1103/PhysRevB.88.214420.

[14] Varley F. Sears. Neutron scattering lengths and cross sections. *Neutron News*, 3(3):26–37, 1992. doi:10.1080/10448639208218770.

[15] Frank Heinrich. Deuteration in biological neutron reflectometry. In *Methods in Enzymology*, volume 566, pages 211–230. Elsevier, 2016. doi:10.1016/bs.mie.2015.05.019.

[16] Charles F. Majkrzak, Elisabeth Carpenter, Frank Heinrich, and Norman F. Berk. When beauty is only skin deep; optimizing the sensitivity of specular neutron reflectivity for probing structure beneath the surface of thin films. *Journal of Applied Physics*, 110(10):102212, 2011. doi:10.1063/1.3661979.

[17] Alessandro Greco, Vladimir Starostin, Christos Karapanagiotis, Alexander Hinderhofer, Alexander Gerlach, Linus Pithan, Sascha Liehr, Frank Schreiber, and Stefan Kowarik. Fast fitting of reflectivity data of growing thin films using neural networks. *Journal of Applied Crystallography*, 52(6):1342–1347, 2019. doi:10.1107/S1600576719013311.

[18] Alessandro Greco, Vladimir Starostin, Alexander Hinderhofer, Alexander Gerlach, Maximilian Skoda, Stefan Kowarik, and Frank Schreiber. Neural network analysis of neutron and x-ray reflectivity data: Pathological cases, performance and perspectives. *Machine Learning: Science and Technology*, 2021. doi:10.1088/2632-2153/abf9b1.

[19] Daniil Mironov, James H Durant, Rebecca Mackenzie, and Joshaniel F K Cooper. Towards automated analysis for neutron reflectivity. *Machine Learning: Science and Technology*, 2(3):035006, 2021. doi:10.1088/2632-2153/abe7b5.

[20] Juan Manuel Carmona Loaiza and Zamaan Raza. Towards reflectivity profile inversion through artificial neural networks. *Machine Learning: Science and Technology*, 2(2):025034, 2021. doi:10.1088/2632-2153/abe564.

[21] Ben Yu-Kuang Hu. Kramers–Kronig in two lines. *American Journal of Physics*, 57(9):821–821, 1989. doi:10.1119/1.15901.

[22] Xiao-Lin Zhou and Sow-Hsin Chen. Theoretical foundation of x-ray and neutron reflectometry. *Physics Reports*, 257(4):223–348, 1995. doi:10.1016/0370-1573(94)00110-0.

[23] G. L. Squires. *Introduction to the Theory of Thermal Neutron Scattering*. Cambridge University Press, 3 edition, 2012. doi:10.1017/CBO9781139107808.

[24] A. J. Dianoux, G. H. Lander, and Institut Laue-Langevin. *Neutron Data Booklet*. Institut Laue-Langevin, 2002.

[25] C. F. Majkrzak, K. V. O'Donovan, and N. F. Berk. Polarized neutron reflectometry. In Tapan Chatterji, editor, *Neutron Scattering from Magnetic Materials*, pages 397–471. Elsevier Science, 2006. doi:10.1016/B978-044451050-1/50010-0.

[26] Javier Dawidowski, José Rolando Granada, Javier Roberto Santisteban, Florencia Cantargi, and Luis Alberto Rodríguez Palomino. Appendix - neutron scattering lengths and cross sections. In Felix Fernandez-Alonso and David L. Price, editors, *Experimental Methods in the Physical Sciences*, volume 44 of *Neutron Scattering – Fundamentals*, pages 471–528. Academic Press, 2013. doi:10.1016/B978-0-12-398374-9.09989-7.

[27] Jean Daillant and Alain Gibaud, editors. *X-ray and Neutron Reflectivity: Principles and Applications*, volume 770 of *Lecture Notes in Physics*. Springer Berlin Heidelberg, 2009. doi:10.1007/978-3-540-88588-7.

[28] L. D. Faddeyev and B. Seckler. The inverse problem in the quantum theory of scattering. *Journal of Mathematical Physics*, 4(1):72–104, 1963. doi:10.1063/1.1703891.

[29] Res Jost. Über die falschen nullstellen der eigenwerte der s-matrix. *Helvetica Physica Acta*, 1947. doi:10.5169/SEALS-111803.

[30] M. Reed and B. Simon. *Methods of Modern Mathematical Physics. III. Scattering Theory*. Academic Press, 1979.

[31] P. Deift and E. Trubowitz. Inverse scattering on the line. *Communications on Pure and Applied Mathematics*, 32(2):121–251, 1979. doi:10.1002/cpa.3160320202.

[32] Charles F. Majkrzak, N. F. Berk, John F. Ankner, Sushil K. Satija, and Terence P. Russell. Determination of nonmagnetic density profiles using polarized neutron reflectivity. In *Neutron Optical Devices and Applications*, volume 1738, pages 282–304. International Society for Optics and Photonics, 1992. doi:10.1117/12.130639.

[33] K. Chadan and P. C. Sabatier. *Inverse problems in quantum scattering theory.* Texts and monographs in physics. Springer-Verlag, 2nd ed., rev. and expanded edition, 1989.

[34] Heinz Kiessig. Untersuchungen zur Totalreflexion von Röntgenstrahlen. *Annalen der Physik*, 402(6):715–768, 1931. doi:https://doi.org/10.1002/andp.19314020607.

[35] Heinz Kiessig. Interferenz von Röntgenstrahlen an dünnen Schichten. *Annalen der Physik*, 402(7):769–788, 1931. doi:10.1002/andp.19314020702.

[36] William Henry Bragg and William Lawrence Bragg. The reflection of x-rays by crystals. *Proceedings of the Royal Society of London. Series A, Containing Papers of a Mathematical and Physical Character*, 88(605):428–438, 1913. doi:10.1098/rspa.1913.0040.

[37] S. K. Sinha, E. B. Sirota, S. Garoff, and H. B. Stanley. X-ray and neutron scattering from rough surfaces. *Physical Review B*, 38(4):2297–2311, 1988. doi:10.1103/PhysRevB.38.2297.

[38] Metin Tolan. *X-Ray Scattering from Soft-Matter Thin Films: Materials Science and Basic Research.* Springer Tracts in Modern Physics. Springer-Verlag, 1999. doi:10.1007/BFb0112834.

[39] L. Névot and P. Croce. Caractérisation des surfaces par réflexion rasante de rayons x. application à l'étude du polissage de quelques verres silicates. *Revue de Physique Appliquée*, 15(3):761–779, 1980. doi:10.1051/rphysap:01980001503076100.

[40] P. Debye. Interferenz von Röntgenstrahlen und Wärmebewegung. *Annalen der Physik*, 348(1):49–92, 1913. doi:10.1002/andp.19133480105.

[41] Ivar Waller. Zur Frage der Einwirkung der Wärmebewegung auf die Interferenz von Röntgenstrahlen. *Zeitschrift für Physik*, 17(1):398–408, 1923. doi:10.1007/BF01328696.

[42] Florin Abelès. Sur la propagation des ondes électromagnétiques dans les milieux stratifiés. *Annales de Physique*, 12(3):504–520, 1948. doi:10.1051/anphys/194812030504.

[43] L. G. Parratt. Surface studies of solids by total reflection of x-rays. *Physical Review*, 95(2):359–369, 1954. doi:10.1103/PhysRev.95.359.

[44] Almadena Chtchelkanova, John Gunnels, Greg Morrow, James Overfelt, and Robert A. van de Geijn. Parallel implementation of BLAS: general techniques for level 3 BLAS. *Concurrency: Practice and Experience*, 9(9):837–857, 1997. doi:10.1002/(SICI)1096-9128(199709)9:9<837::AID-CPE267>3.0.CO;2-2.

[45] C. F Majkrzak and N. F Berk. Phase sensitive reflectometry and the unambiguous determination of scattering length density profiles. *Physica B: Condensed Matter*, 336(1):27–38, 2003. doi:10.1016/S0921-4526(03)00266-7.

[46] C. F. Majkrzak and N. F. Berk. Exact determination of the phase in neutron reflectometry. *Physical Review B*, 52(15):10827–10830, October 1995. doi:10.1103/PhysRevB.52.10827.

[47] Max Born and Emil Wolf. *Principles of Optics: Electromagnetic Theory of Propagation, Interference and Diffraction of Light*. Cambridge University Press, 7 edition, 1999. doi:10.1017/CBO9781139644181.

[48] Matthew Wormington, Charles Panaccione, Kevin M. Matney, and D. Keith Bowen. Characterization of structures from x-ray scattering data using genetic algorithms. *Philosophical Transactions of the Royal Society of London. Series A: Mathematical, Physical and Engineering Sciences*, 357(1761):2827–2848, 1999. doi:10.1098/rsta.1999.0469.

[49] M. Björck and G. Andersson. GenX: an extensible x-ray reflectivity refinement program utilizing differential evolution. *Journal of Applied Crystallography*, 40(6):1174–1178, 2007. doi:10.1107/S0021889807045086.

[50] Devinderjit Sivia and John Skilling. *Data Analysis: A Bayesian Tutorial*. Oxford University Press, 2006.

[51] Joint Committee for Guides in Metrology. Evaluation of measurement data — Supplement 1 to the "Guide to the expression of uncertainty in measurement" — Propagation of distributions using a Monte Carlo method. Technical report, Joint Committee for Guides in Metrology (JCGM), 2008.

[52] Herman C. and E. L. Lehmann. The use of maximum likelihood estimates in χ^2 tests for goodness of fit. *The Annals of Mathematical Statistics*, 25(3):579–586, 1954. doi:10.1214/aoms/1177728726.

[53] Rene Andrae, Tim Schulze-Hartung, and Peter Melchior. Dos and don'ts of reduced chi-squared. *arXiv:1012.3754 [astro-ph, physics:physics, stat]*, 2010. URL: http://arxiv.org/abs/1012.3754, arXiv:1012.3754.

[54] Leonhard Held and Daniel Sabanés Bové. *Applied Statistical Inference*. Springer Berlin Heidelberg, 2014. doi:10.1007/978-3-642-37887-4.

[55] E. T. Jaynes and Oscar Kempthorne. Confidence intervals vs bayesian intervals. In William Leonard Harper and Clifford Alan Hooker, editors, *Foundations of Probability Theory, Statistical Inference, and Statistical Theories of Science: Proceedings of an International Research Colloquium held at the University of Western Ontario, London, Canada, 10–13 May 1973 Volume II Foundations and Philosophy of Statistical Inference*, The University of Western On-

tario Series in Philosophy of Science, pages 175–257. Springer Netherlands, 1976. doi:10.1007/978-94-010-1436-6_6.

[56] Alfio Quarteroni, Riccardo Sacco, and Fausto Saleri. *Numerical Mathematics*. Texts in Applied Mathematics. Springer-Verlag, 2 edition, 2007. doi:10.1007/b98885.

[57] Philip J. Davis and Philip Rabinowitz. *Methods of Numerical Integration - 2nd Edition*. Academic Press, 1984.

[58] Nicholas Metropolis, Arianna W. Rosenbluth, Marshall N. Rosenbluth, Augusta H. Teller, and Edward Teller. Equation of state calculations by fast computing machines. *The Journal of Chemical Physics*, 21(6):1087–1092, 1953. doi:10.1063/1.1699114.

[59] W. K. Hastings. Monte Carlo sampling methods using Markov chains and their applications. *Biometrika*, 57(1):97–109, 04 1970. doi:10.1093/biomet/57.1.97.

[60] Daniel Foreman-Mackey. corner.py: Scatterplot matrices in python. *The Journal of Open Source Software*, 1(2):24, jun 2016. doi:10.21105/joss.00024.

[61] D. Foreman-Mackey, D. W. Hogg, D. Lang, and J. Goodman. emcee: The MCMC hammer. *PASP*, 125:306–312, 2013. arXiv:1202.3665, doi:10.1086/670067.

[62] El Houcine Bergou, Youssef Diouane, and Vyacheslav Kungurtsev. Convergence and complexity analysis of a levenberg–marquardt algorithm for inverse problems. *Journal of Optimization Theory and Applications*, 185(3):927–944, 2020. doi:10.1007/s10957-020-01666-1.

[63] Christian Kanzow, Nobuo Yamashita, and Masao Fukushima. Levenberg–marquardt methods with strong local convergence properties for solving nonlinear equations with convex constraints. *Journal of Computational and Applied Mathematics*, 172(2):375–397, 2004. doi:10.1016/j.cam.2004.02.013.

[64] Rainer Storn and Kenneth Price. Differential evolution–a simple and efficient heuristic for global optimization over continuous spaces. *Journal of global optimization*, 11(4):341–359, 1997. doi:10.1023/A:1008202821328.

[65] R. Storn. On the usage of differential evolution for function optimization. In *Proceedings of North American Fuzzy Information Processing*, pages 519–523, 1996. doi:10.1109/NAFIPS.1996.534789.

[66] Kenneth V. Price, Rainer M. Storn, and Jouni A. Lampinen. *Differential evolution: a practical approach to global optimization*. Natural computing series. Springer, 2005. doi:10.1007/3-540-31306-0.

[67] B. J. Kirby, P. A. Kienzle, B. B. Maranville, N. F. Berk, J. Krycka, F. Heinrich, and C. F. Majkrzak. Phase-sensitive specular neutron reflectometry for imaging the

nanometer scale composition depth profile of thin-film materials. *Current Opinion in Colloid & Interface Science*, 17(1):44–53, 2012. doi:10.1016/j.cocis.2011.11.001.

[68] P. A. Kienzle, J. Krycka, N. Patel, and I. Sahin. Refl1D. (Version 0.8.14) [Computer Software]. College Park, MD: University of Maryland, 2011-.

[69] P. A. Kienzle, J. Krycka, N. Patel, and I. Sahin. Bumps. (Version 0.8.0) [Computer Software]. College Park, MD: University of Maryland, 2011-.

[70] J. A. Vrugt, C. J. F. ter Braak, C. G. H. Diks, B. A. Robinson, J. M. Hyman, and D. Higdon. Accelerating markov chain monte carlo simulation by differential evolution with self-adaptive randomized subspace sampling. *International Journal of Nonlinear Sciences and Numerical Simulation*, 10(3), 2009. doi:10.1515/IJNSNS.2009.10.3.273.

[71] Jingfan Ye, Alexander Book, Sina Mayr, Henrik Gabold, Fankai Meng, Helena Schäfferer, Ryan Need, Dustin Gilbert, Thomas Saerbeck, Jochen Stahn, Peter Böni, and Wolfgang Kreuzpaintner. Design and realization of a sputter deposition system for the in situ and in operando use in polarized neutron reflectometry experiments: Novel capabilities. *Nuclear Instruments and Methods in Physics Research Section A: Accelerators, Spectrometers, Detectors and Associated Equipment*, 964:163710, 2020. doi:10.1016/j.nima.2020.163710.

[72] Andreas Schmehl, Thomas Mairoser, Alexander Herrnberger, Cyril Stephanos, Stefan Meir, Benjamin Förg, Birgit Wiedemann, Peter Böni, Jochen Mannhart, and Wolfgang Kreuzpaintner. Design and realization of a sputter deposition system for the in situ- and in operando-use in polarized neutron reflectometry experiments. *Nuclear Instruments and Methods in Physics Research Section A: Accelerators, Spectrometers, Detectors and Associated Equipment*, 883:170–182, 2018. doi:10.1016/j.nima.2017.11.086.

[73] P. D. Lax. *Functional Analysis*. Pure and Applied Mathematics: A Wiley Series of Texts, Monographs and Tracts. Wiley, 2014.

[74] Amy Cohen and Thomas Kappeler. Scattering and inverse scattering for steplike potentials in the schrödinger equation. *Indiana University Mathematics Journal*, 34(1):127–180, 1985. URL: http://www.jstor.org/stable/24893895.

[75] Res Jost and Walter Kohn. Construction of a potential from a phase shift. *Physical Review*, 87(6):977–992, 1952. doi:10.1103/PhysRev.87.977.

[76] Paul E. Sacks. Reconstruction of steplike potentials. *Wave Motion*, 18(1):21–30, October 1993. doi:10.1016/0165-2125(93)90058-N.

[77] Barry Simon. The bound state of weakly coupled schrödinger operators in one and two dimensions. *Annals of Physics*, 97(2):279–288, 1976. doi:10.1016/0003-4916(76)90038-5.

[78] L. Koester, H. Rauch, and E. Seymann. Neutron scattering lengths: A survey of experimental data and methods. *Atomic Data and Nuclear Data Tables*, 49(1):65–120, 1991. doi:10.1016/0092-640X(91)90012-S.

[79] N. Levinson. On the uniqueness of the potential in a schrödinger equation for a given asymptotic phase. *Kgl. Danske Videnskab Selskab. Mat. Fys. Medd.*, 25, 1949. doi:10.1007/978-1-4612-5341-9_17.

[80] Lyudvig Dmitrievich Faddeev. Properties of the s-matrix of the one-dimensional schrodinger equation. *Trudy Matematicheskogo Instituta imeni VA Steklova*, 73:314–336, 1964.

[81] Z. S. Agranovich and V. A. Marchenko. *The Inverse Problem of Scattering Theory*. Courier Dover Publications, 1963.

[82] Tuncay Aktosun and Paul E. Sacks. Potential splitting and numerical solution of the inverse scattering problem on the line. *Mathematical Methods in the Applied Sciences*, 25(4):347–355, 2002. doi:10.1002/mma.292.

[83] Cornelis van der Mee, Sebastiano Seatzu, and Daniela Theis. Structured matrix algorithms for inverse scattering on the line. *Calcolo*, 44(2):59–87, 2007. doi:10.1007/s10092-007-0129-9.

[84] Kenneth P. Bube and Robert Burridge. The one-dimensional inverse problem of reflection seismology. *SIAM Review*, 25(4):497–559, 1983. doi:10.1137/1025122.

[85] Alexander Book. DirectInversion (dinv). (Version 0.1.0) [Computer Software], 2019. URL: https://github.com/TUM-E21-ThinFilms/DirectInversion.

[86] Python Software Foundation. Python language reference. (Version 3.9.4) [Computer Software], 2021. URL: http://www.python.org.

[87] Charles R. Harris, K. Jarrod Millman, Stéfan J. van der Walt, Ralf Gommers, Pauli Virtanen, David Cournapeau, Eric Wieser, Julian Taylor, Sebastian Berg, Nathaniel J. Smith, Robert Kern, Matti Picus, Stephan Hoyer, Marten H. van Kerkwijk, Matthew Brett, Allan Haldane, Jaime Fernández del Río, Mark Wiebe, Pearu Peterson, Pierre Gérard-Marchant, Kevin Sheppard, Tyler Reddy, Warren Weckesser, Hameer Abbasi, Christoph Gohlke, and Travis E. Oliphant. Array programming with NumPy. *Nature*, 585(7825):357–362, September 2020. doi:10.1038/s41586-020-2649-2.

[88] Pauli Virtanen, Ralf Gommers, Travis E. Oliphant, Matt Haberland, Tyler Reddy, David Cournapeau, Evgeni Burovski, Pearu Peterson, Warren Weckesser, Jonathan Bright, Stéfan J. van der Walt, Matthew Brett, Joshua Wilson, K. Jarrod Millman, Nikolay Mayorov, Andrew R. J. Nelson, Eric Jones, Robert Kern, Eric Larson, C J Carey, İlhan Polat, Yu Feng, Eric W. Moore, Jake VanderPlas, Denis Laxalde, Josef Perktold, Robert Cimrman, Ian Henriksen, E. A. Quintero,

Charles R. Harris, Anne M. Archibald, Antônio H. Ribeiro, Fabian Pedregosa, Paul van Mulbregt, and SciPy 1.0 Contributors. SciPy 1.0: Fundamental Algorithms for Scientific Computing in Python. *Nature Methods*, 17:261–272, 2020. doi:10.1038/s41592-019-0686-2.

[89] H. Fiedeldey, R. Lipperheide, H. Leeb, and S.A. Sofianos. A proposal for the determination of the phases in specular neutron reflection. *Physics Letters A*, 170(5):347–351, November 1992. doi:10.1016/0375-9601(92)90885-P.

[90] R. Golub, S. Felber, R. Gähler, and E. Gutsmiedl. A modest proposal concerning tunneling times. *Physics Letters A*, 148(1):27–30, 1990. doi:10.1016/0375-9601(90)90568-9.

[91] William L. Clinton. Phase determination in x-ray and neutron reflectivity using logarithmic dispersion relations. *Physical Review B*, 48(1):1–5, July 1993. Publisher: American Physical Society. doi:10.1103/PhysRevB.48.1.

[92] Patrick L. Nash, R. J. Bell, and R. Alexander. On the kramers-kronig relation for the phase spectrum. *Journal of Modern Optics*, 42(9):1837–1842, 1995. doi:10.1080/09500349514551601.

[93] Jean-Michel André, Karine Le Guen, Philippe Jonnard, Nicola Mahne, Angelo Giglia, and Stefano Nannarone. On the kramers–kronig transform with logarithmic kernel for the reflection phase in the drude model. *Journal of Modern Optics*, 57(16):1504–1512, 2010. doi:10.1080/09500340.2010.506015.

[94] V.-O. de Haan, A. A. van Well, S. Adenwalla, and G. P. Felcher. Retrieval of phase information in neutron reflectometry. *Physical Review B*, 52(15):10831–10833, October 1995. doi:10.1103/PhysRevB.52.10831.

[95] C. F. Majkrzak, N. F. Berk, J. A. Dura, S. K. Satija, A. Karim, J. Pedulla, and R. D. Deslattes. Phase determination and inversion in specular neutron reflectometry. *Physica B: Condensed Matter*, 248(1):338–342, June 1998. doi:10.1016/S0921-4526(98)00260-9.

[96] C. F. Majkrzak, N. F. Berk, P. Kienzle, and U. Perez-Salas. Progress in the Development of Phase-Sensitive Neutron Reflectometry Methods. *Langmuir*, 25(7):4154–4161, April 2009. doi:10.1021/la802838t.

[97] V. O. de Haan, A. A. van Well, P. E. Sacks, S. Adenwalla, and G. P. Felcher. Toward the solution of the inverse problem in neutron reflectometry. *Physica B: Condensed Matter*, 221(1):524–532, 1996. doi:10.1016/0921-4526(95)00975-2.

[98] B. J. Kirby, P. A. Kienzle, B. B. Maranville, N. F. Berk, J. Krycka, F. Heinrich, and C. F. Majkrzak. Phase-sensitive specular neutron reflectometry for imaging the nanometer scale composition depth profile of thin-film materials. *Current Opinion in Colloid & Interface Science*, 17(1):44–53, February 2012. doi:10.1016/j.cocis.2011.11.001.

[99] C. F. Majkrzak, N. F. Berk, V. Silin, and C. W. Meuse. Experimental demonstration of phase determination in neutron reflectometry by variation of the surrounding media. *Physica B: Condensed Matter*, 283(1):248–252, June 2000. doi:10.1016/S0921-4526(99)01985-7.

[100] M. K. Sanyal, S. K. Sinha, A. Gibaud, K. G. Huang, B. L. Carvalho, M. Rafailovich, J. Sokolov, X. Zhao, and W. Zhao. Fourier Reconstruction of Density Profiles of Thin Films Using Anomalous X-Ray Reflectivity. *Europhysics Letters (EPL)*, 21(6):691–696, February 1993. doi:10.1209/0295-5075/21/6/010.

[101] J. E. Lynn and P. A. Seeger. Resonance effects in neutron scattering lengths of rare-earth nuclides. *Atomic Data and Nuclear Data Tables*, 44(2):191–207, March 1990. doi:10.1016/0092-640X(90)90013-A.

[102] Yu. A. Salamatov and E. A. Kravtsov. Use of gadolinium as a reference layer for neutron reflectometry. *Journal of Surface Investigation. X-ray, Synchrotron and Neutron Techniques*, 10(6):1169–1172, November 2016. doi:10.1134/S1027451016050591.

[103] E. S. Nikova, Yu. A. Salamatov, E. A. Kravtsov, M. V. Makarova, V. V. Proglyado, V. V. Ustinov, V. I. Bodnarchuk, and A. V. Nagorny. Experimental Approbation of Reference Layer Method in Resonant Neutron Reflectometry. *Physics of Metals and Metallography*, 120(9):838–843, September 2019. doi:10.1134/S0031918X19090102.

[104] E. S. Nikova, Yu. A. Salamatov, E. A. Kravtsov, V. V. Ustinov, V. I. Bodnarchuk, and A. V. Nagorny. Development of Reference Layer Method in Resonant Neutron Reflectometry. *Journal of Surface Investigation: X-ray, Synchrotron and Neutron Techniques*, 14(S1):S161–S164, October 2020. doi:10.1134/S1027451020070344.

[105] E. W. Cheney and David Kincaid. *Numerical mathematics and computing*. Brooks/Cole, 6th edition, 2007.

[106] H. Leeb, J. Kasper, and R. Lipperheide. Determination of the phase in neutron reflectometry by polarization measurements. *Physics Letters A*, 239(3):147–152, 1998. doi:10.1016/S0375-9601(97)00972-9.

[107] J. Kasper, H. Leeb, and R. Lipperheide. Phase determination in spin-polarized neutron specular reflection. *Physical Review Letters*, 80(12):2614–2617, 1998. doi:10.1103/PhysRevLett.80.2614.

[108] Alexander Book and Paul A. Kienzle. Retrieval of the complex reflection coefficient below the critical edge for neutron reflectometry. *Physica B: Condensed Matter*, 588:412181, 2020. doi:10.1016/j.physb.2020.412181.

[109] Joint Committee for Guides in Metrology. International vocabulary of metrology — Basic and general concepts and associated terms. Technical report, Joint Committee for Guides in Metrology (JCGM), 2008.

[110] N. F. Berk and C. F. Majkrzak. Statistical analysis of phase-inversion neutron specular reflectivity. *Langmuir*, 25(7):4132–4144, 2009. doi:10.1021/la802779r.

[111] Edwin Hewitt and Robert E. Hewitt. The gibbs-wilbraham phenomenon: An episode in fourier analysis. *Archive for History of Exact Sciences*, 21(2):129–160, 1979. doi:10.1007/BF00330404.

[112] OEIS Foundation Inc. The on-line encyclopedia of integer sequences. *OEIS*, 2021. URL: https://oeis.org/A036792.

[113] Maxime Bocher. Introduction to the theory of fourier's series. *Annals of Mathematics*, 7(3):81–152, 1906. doi:10.2307/1967238.

[114] Horatio Scott Carslaw. *Introduction to the Theory of Fourier's Series and Integrals and the Mathematical Theory of the Conduction of Heat*. Macmillan and Company, limited, 1906.

[115] A. N. Tikhonov, A. V. Goncharsky, V. V. Stepanov, and A. G. Yagola. *Numerical Methods for the Solution of Ill-Posed Problems*. Springer Netherlands, 1995. doi:10.1007/978-94-015-8480-7.

[116] J. F. Ankner and G. P. Felcher. Polarized-neutron reflectometry. *Journal of Magnetism and Magnetic Materials*, page 14, 1999. doi:10.1016/S0304-8853(99)00392-3.

[117] K. V. O'Donovan, J. A. Borchers, C. F. Majkrzak, O. Hellwig, and E. E. Fullerton. Pinpointing chiral structures with front-back polarized neutron reflectometry. *Physical Review Letters*, 88(6):067201, 2002. doi:10.1103/PhysRevLett.88.067201.

[118] X. Z. Zhan, G. Li, J. W. Cai, T. Zhu, J. F. K. Cooper, C. J. Kinane, and S. Langridge. Probing the transfer of the exchange bias effect by polarized neutron reflectometry. *Scientific Reports*, 9(1):6708, 2019. doi:10.1038/s41598-019-43251-1.

[119] Jingfan Ye. *In situ Polarized Neutron Reflectometry and Investigations of Exchange Biased and Multiferroic Heterostructures*. PhD thesis, Technical University of Munich, Department of Physics, 2019. URL: http://nbn-resolving.de/urn/resolver.pl?urn:nbn:de:bvb:91-diss-20190920-1514936-1-4.

[120] J. Stahn and A. Glavic. Focusing neutron reflectometry: Implementation and experience on the TOF-reflectometer amor. *Nuclear Instruments and Methods in Physics Research Section A: Accelerators, Spectrometers, Detectors and Associated Equipment*, 821, 2016. doi:10.1016/j.nima.2016.03.007.

[121] J. Stahn, T. Panzner, U. Filges, C. Marcelot, and P. Böni. Study on a focusing, low-background neutron delivery system. *Nuclear Instruments and Methods in Physics Research Section A: Accelerators, Spectrometers, Detectors and Associated Equipment*, 634(1):S12–S16, 2011. doi:10.1016/j.nima.2010.06.221.

[122] N. Hirashita, M. Kinoshita, I. Aikawa, and T. Ajioka. Effects of surface hydrogen on the air oxidation at room temperature of HF-treated si (100) surfaces. *Applied Physics Letters*, 56(5):451–453, 1990. doi:10.1063/1.102762.

[123] Wolfgang Kreuzpaintner, Birgit Wiedemann, Jochen Stahn, Jean-François Moulin, Sina Mayr, Thomas Mairoser, Andreas Schmehl, Alexander Herrnberger, Panagiotis Korelis, Martin Haese, Jingfan Ye, Matthias Pomm, Peter Böni, and Jochen Mannhart. In situ Polarized Neutron Reflectometry: Epitaxial Thin-Film Growth of Fe on Cu(001) by dc Magnetron Sputtering. *Physical Review Applied*, 7(5):054004, 2017. doi:10.1103/PhysRevApplied.7.054004.

[124] J. Philip. The most ill-posed non-negative kernels in discrete deconvolution. *Inverse Problems*, 3(2):309–328, 1987. doi:10.1088/0266-5611/3/2/013.

[125] B. W. Treece, P. A. Kienzle, D. P. Hoogerheide, C. F. Majkrzak, M. Lösche, and F. Heinrich. Optimization of reflectometry experiments using information theory. *Journal of Applied Crystallography*, 52(1):47–59, 2019. doi:10.1107/S1600576718017016.

[126] Frank Heinrich, Paul A. Kienzle, David P. Hoogerheide, and Mathias Lösche. Information gain from isotopic contrast variation in neutron reflectometry on protein–membrane complex structures. *Journal of Applied Crystallography*, 53(3):800–810, 2020. doi:10.1107/S1600576720005634.

Appendix A

Developed Programs

This chapter gives an overview of python [86] programs, which were developed to analyze the reflectivity data. The two main programs, which will be described in detail, are *DiRefl* and *DirectInversion*. The package *DiRefl* is used to retrieve the reflection from the reflectivity. The second package *DirectInversion* calculates the solution of the GLM integral equation to invert the reflection and obtain the SLD. In addition, it can retrieve the reflection below the total reflection edge.

Other packages were developed as well. Some of them are

1. *UXDConverter*: This graphical program converts x-ray reflectivity data files, which are measured on D500, D5000 and D8 Siemens GmbH/Bruker diffractometers, to a human readable format, which is used for reflectivity fitting software.

2. *skipi*: This package provides tools to easily work with one dimensional functions without needing to specify the domain of the function each time. It supports Fourier, cosine, sine transforms and their corresponding inverse transforms, convolution operators and some statistical operations.

3. Communication protocols for the *in situ* sputtering chamber: A total of 21 protocols were implemented to fully automate the communication with vacuum gauges, pumps, valves, sputtering power supplies and temperature control units.

The software is available online on `https://github.com/TUM-E21-ThinFilms` and licensed under the GNU General Public License or MIT License.

A.1 DirectInversion

The *DirectInversion* software is the implementation of the GLM integral equation. It directly discretizes the integral equation and solves a linear system to obtain an inverted scattering potential. The discretization scheme and an approximation for speeding up the computation is described in appendix B.3 . Furthermore, the fixed-point algorithm of section 3.3.3 is implemented therein.

Let $q = (q_i)_i$ be an array of wave vector transfers and $r = (R(q_i))_i$ be the array of the evaluated reflection. The scattering potential V is reconstructed with the following code:

```
from dinv.glm import PotentialReconstruction
from dinv.fourier import FourierTransform

""" q = [q_1, q_2, q_3, ... q_n], Unit: 1/Angstrom """
""" r = [R(q_1), R(q_2), ... R(q_n)] """
thickness = 500 """ Unit: Angstrom """
precision = 1

fourier = FourierTransform(q / 2.0, r.real, r.imag)
rec = PotentialReconstruction(thickness, precision)
V = rec.reconstruct(fourier)
```

The scattering potential V is reconstructed on a equidistantly spaced grid $z = 0$ to $z =$ `thickness` with `thickness` $\times$ `precision` number of points.

To retrieve the reflection below the total reflection edge using the reflection $r = R(q)$ with $q \geq q_c$, the following code is used:

```
from dinv.helper import DataRun, Function

Reflection = Function.to_function(q, r)

def constraint(potential, z_space):
    V = potential(z_space)
    V[(z_space > 200) & (z_space <= 350)] = 6.554e-6 """ Cu SLD """
    return Function.to_function(z_space, V)

run = DataRun(Reflection, is_k_space=False)

run.iterations = 300
run.tolerance = 1e-8

run.precision = 1
run.thickness = 500

run.setup()

reflection = run.run(constraint)
q_space = run.q_interpolation_range
```

In this example, the `constraint` function constraints the scattering potential between $z = 200\,\text{Å}$ and $z = 350\,\text{Å}$ to a Cu SLD. This can be useful if the algorithm does not converge due to a violation of the requirement in Corollary 2. The variable `run.iterations` denotes the maximum number of iterations of the fixed-point algorithm until termination and `run.tolerance` is the stopping tolerance for convergence, which is defined by equation (3.54). In each iteration of the fixed-point algorithm, an intermediate scattering potential is computed. The grid of the scattering potential is defined with the variables `run.thickness` and `run.precision`.

The solution of the fixed-point algorithm is stored in `reflection`, i. e. $R(q)$ for $0 \leq q \leq q_c$. It is the reflection evaluated at $q \in$ `q_space`. The variable `q_space` contains the

points on a grid from $q = 0$ to $q = q_c$ where the discretization Δq is determined from the input data.

A.2 DiRefl

The program *DiRefl* (Direct Inversion Reflectometry) was developed by the National Institute of Standards and Technology (NIST) and University of Maryland. The software reconstructs the reflection by a variation of surrounding approach.

To reconstruct the reflection from measurements performed with the *in situ* deposition chamber, the software was upgraded such that it can supports the top and bottom reference variation approach. The software loads the reflectivity from a text file containing $q, |R|^2(q)$ and $\Delta|R|^2(q)$ and associates it with a reference SLD. The description of the reference SLD can either be a user defined function, a slab model assembled with the *refl1d* semantic or loaded from file.

The following code shows an exemplary usage of the software API loading one reflectivity measurement. The reference layer is a 35 Å thick Fe layer with a roughness 5 Å at the Fe/Air interface. The reference is described with the *refl1d* semantic:

```
1  from refl1d.names import *
2  from direfl.api.reference_layer import TopReferenceVariation
3  from direfl.api.sld_profile import SlabsSLDProfile
4
5  Fe_SLD = SLD(rho=8.024)
6  fe_reference = Slab(Fe_SLD, thickness=35, interface=5)
7  reference = SlabsSLDProfile.from_sample(Stack([air, fe, air]))
8
9  """ Si SLD: 2.077e-6 1/AA^2 """
10 var = TopReferenceVariation(0e-6, 2.074e-6)
11
12 var.load("reflectivity.dat", reference)
13
14 var.remesh()
15 var.run()
16
17 q, R, dR = var.Q, var.R, var.dR
```

The software can reconstruct the reflection with $N \geq 2$ reflectivity measurements, but, if $N = 2$ it will return two branches of possible reflections. Uncertainty estimation is performed if $N \geq 3$ and it is based on the covariance matrix of a linear least squares problem.

If the various reflectivity data are not measured on the same grid, a re-mesh is necessary which is achieved with the method `var.remesh`. It computes the coarsest grid based on all q grids and linearly interpolates the reflectivity $|R|^2$ and its uncertainty $\Delta|R|^2$ on the new grid. The new grid is accessible with `var.Q` and the reconstructed reflection and its uncertainty are stored in `var.R` and `var.dR`, respectively.

Appendix B

Additional Calculations

B.1 Calculations for the Reference Layer Method

In this section the reference layer method with a variable top reference is deduced. Basically, the idea of the reference layer method is reflected in equation (3.41), which states that there exists a constraint vector c_K such that $\Sigma = c_\mathrm{K} \cdot \Theta_\mathrm{U}^{bb}$, where Σ is a *measurable* quantity, c_K contains the *known* reference layer information and Θ_U^{bb} corresponds to the *unknown* reflection.

The starting point is the structure of the reflection in equation (3.38):

$$R(\mathcal{T}) = -\frac{\alpha^{fb} - \beta^{fb} - 2i\gamma^{fb}}{\alpha^{fb} + \beta^{fb} + 2}$$

with

$$\begin{aligned} \alpha^{fb} &= n_f^{-1} n_b \mathcal{T}_{11}^2 + n_f^{-1} n_b^{-1} \mathcal{T}_{21}^2 \\ \beta^{fb} &= n_f n_b \mathcal{T}_{12}^2 + n_f n_b^{-1} \mathcal{T}_{22}^2 \\ \gamma^{fb} &= n_b \mathcal{T}_{11} \mathcal{T}_{12} + n_b^{-1} \mathcal{T}_{21} \mathcal{T}_{22}, \end{aligned} \tag{B.1}$$

where n_f and n_b are the refractive indices (see equation (2.27)) of the fronting and backing SLD, respectively. The reflectivity $|R(\mathcal{T})|^2$ is expressed as

$$\begin{aligned} |R(\mathcal{T})|^2 = R(\mathcal{T})\overline{R(\mathcal{T})} &= \frac{(\alpha^{fb} - \beta^{fb} - 2i\gamma^{fb})(\alpha^{fb} - \beta^{fb} + 2i\gamma^{fb})}{(\alpha^{fb} + \beta^{fb} + 2)^2} \\ &= \frac{(\alpha^{fb} - \beta^{fb})^2 + 4(\gamma^{fb})^2}{(\alpha^{fb} + \beta^{fb} + 2)^2}. \end{aligned} \tag{B.2}$$

Notce that this calculation requires that α, β and γ are real valued, which is true if and only if the transfer matrix $\mathcal{T}$ is real valued, i. e. the SLD is non-absorbing.

Plugging the reflectivity into $\Sigma = 2n_f n_b \frac{1+|R|^2}{1-|R|^2}$ and using $(\gamma^{fb})^2 = \alpha^{fb}\beta^{fb} - 1$ (due to the unimodularity of $\mathcal{T}$, see Lemma 2) results in

$$\Sigma = n_f n_b \left(\alpha^{fb} + \beta^{fb}\right). \tag{B.3}$$

The transfer matrix is now split into two sub transfer matrices, i. e. $\mathcal{T} = \mathcal{T}_\mathrm{U}\mathcal{T}_\mathrm{K}$, where $\mathcal{T}_\mathrm{U}$ corresponds to the unknown sample and $\mathcal{T}_\mathrm{K}$ is a known reference. The possibility

of splitting a transfer matrix and expressing it simply by a matrix multiplication is discussed in section 2.5.2. The sub transfer matrices $\mathcal{T}_\mathrm{U}, \mathcal{T}_\mathrm{K}$ and the reversed known transfer matrix[1] $\overleftrightarrow{\mathcal{T}}_\mathrm{K}$ are expressed by

$$\mathcal{T}_\mathrm{U} = \begin{pmatrix} a & b \\ c & d \end{pmatrix}, \quad \mathcal{T}_\mathrm{K} = \begin{pmatrix} w & x \\ y & z \end{pmatrix} \quad \text{and} \quad \overleftrightarrow{\mathcal{T}}_\mathrm{K} = \begin{pmatrix} z & x \\ y & w \end{pmatrix}. \tag{B.4}$$

Plugging in the matrix product of the sub matrices in the definition of α, β and γ and evaluating the measurable quantity Σ yields, after another algebraic manipulation

$$\begin{aligned} \Sigma = &\left(a^2 + n_b^{-2} c^2\right) \left[n_b^2 w^2 + n_f^2 n_b^2 x^2\right] + \left(n_b^2 b^2 + d^2\right) \left[y^2 + n_f^2 z^2\right] \\ &+ 2 \left(n_b ab + n_b^{-1} cd\right) \left[n_b wy + n_f^2 n_b xz\right]. \end{aligned} \tag{B.5}$$

The round and square brackets contain only the the unknown and known transfer matrix entries, respectively. By carefully examining the structure of α, β and γ, one sees that

$$\Sigma = n_b^2 \alpha_\mathrm{U}^{bb} \overleftrightarrow{\beta}_\mathrm{K}^{ff} + n_f^2 \beta_\mathrm{U}^{bb} \overleftrightarrow{\alpha}_\mathrm{K}^{ff} + 2 n_f n_b \gamma_\mathrm{U}^{bb} \overleftrightarrow{\gamma}_\mathrm{K}^{ff}, \tag{B.6}$$

where $\alpha_\mathrm{U}^{bb}, \beta_\mathrm{U}^{bb}, \gamma_\mathrm{U}^{bb}$ are defined by equation (B.1) when taking $\mathcal{T} = \mathcal{T}_\mathrm{U}$ and they correspond to the unknown sample with $n_f = n_b$. Analogously, $\overleftrightarrow{\alpha}_\mathrm{U}^{ff}, \overleftrightarrow{\beta}_\mathrm{U}^{ff}, \overleftrightarrow{\gamma}_\mathrm{U}^{ff}$ are defined by equation (B.1) with $\mathcal{T} = \overleftrightarrow{\mathcal{T}}_\mathrm{K}$ and $n_b = n_f$, i. e. they correspond to the *reversed* reference layer with backing SLD being the fronting SLD.

As the measurable quantity Σ can be factored *linearly* into an unknown and known part, it is possible to construct a constraint vector c_K such that

$$\Sigma = c_\mathrm{K} \cdot \Theta_\mathrm{U}^{bb} \quad \text{with} \quad c_\mathrm{K} \coloneqq \overleftarrow{\begin{pmatrix} n_b^2 \beta \\ n_f^2 \alpha \\ 2 n_f n_b \gamma \end{pmatrix}_\mathrm{K}^{ff}}^{\mathsf{T}} \quad \text{and} \quad \Theta_\mathrm{U}^{bb} \coloneqq \begin{pmatrix} \alpha \\ \beta \\ \gamma \end{pmatrix}_\mathrm{U}^{bb}. \tag{B.7}$$

The vector Θ_U^{bb} is then used to reconstruct the reflection based on equation (3.38).

B.2 Deviation of the Expected Error

The intensity I is assumed to be a Poisson random variable with "rate" I_r, hence, the probability mass of I is expressed as

$$p_I(j) = \begin{cases} \frac{I_\mathrm{r}^j e^{-I_\mathrm{r}}}{j!}, & j \geq 0 \\ 0, & \text{otherwise.} \end{cases} \tag{B.8}$$

[1] This is the transfer matrix that corresponds to the reversed or flipped reference layer. Reversing a sample is discussed in section 2.5.2.2.

where j is the number of counts. The quantity Σ is required for the reference layer method and it is determined from the reflected intensity by

$$\Sigma \sim \frac{I_0 + I_\mathrm{r}}{I_0 - I_\mathrm{r}}. \tag{B.9}$$

The error of Σ is defined as $\varepsilon_\Sigma = \hat{\Sigma} - \Sigma$ where $\hat{\Sigma} = \Sigma(I_\mathrm{r} + \varepsilon_{I_\mathrm{r}})$ is the intensity error $\varepsilon_{I_\mathrm{r}}$ degraded quantity. A simple computation shows that the error of Σ can be expressed as

$$\varepsilon_\Sigma = \frac{2\varepsilon_{I_\mathrm{r}} I_0}{(I_0 - I_\mathrm{r} - \varepsilon)(I_0 - I_\mathrm{r})}. \tag{B.10}$$

The error $\varepsilon_{I_\mathrm{r}}$ is a shifted Poisson distribution by I_r which is furthermore truncated such that the intensity I can never equal or exceed the incident intensity I_0. The probability mass of $\varepsilon_{I_\mathrm{r}}$ is thus

$$p_{\varepsilon_{I_\mathrm{r}}}(j) = \frac{1}{\mathrm{CDF}_{\mathrm{Pois}(I_\mathrm{r})}(I_0 - 1)} \begin{cases} \frac{e^{-I_\mathrm{r}} I_\mathrm{r}^{j+I_\mathrm{r}}}{(j+I_\mathrm{r})!}, & -I_\mathrm{r} \leq j \leq I_0 - I_\mathrm{r} - 1 \\ 0, & \text{otherwise} \end{cases} \tag{B.11}$$

The normalization factor including the CDF ensures that the total probability sums up to 1. In particular one has

$$\begin{aligned} \sum_{j=-I_\mathrm{r}}^{I_0 - I_\mathrm{r} - 1} p_{\varepsilon_{I_\mathrm{r}}}(j) &= \frac{1}{\mathrm{CDF}_{\mathrm{Pois}(I_\mathrm{r})}(I_0 - 1)} \sum_{j=-I_\mathrm{r}}^{I_0 - I_\mathrm{r} - 1} \frac{e^{-I_\mathrm{r}} I_\mathrm{r}^{j+I_\mathrm{r}}}{(j + I_\mathrm{r})!} \\ &= \frac{1}{\mathrm{CDF}_{\mathrm{Pois}(I_\mathrm{r})}(I_0 - 1)} \sum_{j=0}^{I_0 - 1} \frac{e^{-I_\mathrm{r}} I_\mathrm{r}^{j}}{j!} = 1. \end{aligned} \tag{B.12}$$

Putting everything together yields the expectation of the error ε_Σ which is stated in the main part of the work

$$\begin{aligned} E[\varepsilon_\Sigma] &= \sum_{j=-\infty}^{\infty} p_{\varepsilon_{I_\mathrm{r}}}(j) \frac{2jI_0}{(I_0 - I_\mathrm{r} - j)(I_0 - I_\mathrm{r})} \\ &= \frac{1}{\mathrm{CDF}_{\mathrm{Pois}(I_\mathrm{r})}(I_0 - 1)} \sum_{j=0}^{I_0 - 1} \frac{I_\mathrm{r}^j e^{-I_\mathrm{r}}}{j!} \left(\frac{2I_0(j - I_\mathrm{r})}{(I_0 - j)(I_0 - I_\mathrm{r})} \right). \end{aligned} \tag{B.13}$$

Numerical simulations are displayed in figure 3.19.

B.3 Direct Discretization Scheme of the Gel'fand-Levitan-Marchenko Integral Equation

To achieve a fast and simple implementation a variant of the GLM integral equation is used which incorporates the fact that the scattering potential has compact support

[76, 82]. The upper limit in the integral equation is then replaced by a finite value and it reads [76]

$$K(z,t) + g(z+t) + \int_{-t}^{z} K(z,y)g(y+t)\mathrm{d}y = 0, \quad z > t, \tag{B.14}$$

where the potential is recovered from $V(z) = \frac{\mathrm{d}}{\mathrm{d}z}K(z,z)$.

The integral equation is discretized for a fixed $z \in \mathbb{R}$ on a grid $G = \{k\Delta - z\}_{k=0}^{N}$ with discretization width $\Delta > 0$ and $N = \frac{2z}{\Delta}$; the grid G thus spans from $-z$ to $+z$. The integral itself is approximated by the trapezoidal rule on the grid G and for a fixed $t = n\Delta - z \in G, n \in \{0, \ldots, N\}$ one has the discretization scheme

$$K(z, z+(n-N)\Delta) + \sum_{k=0}^{n} \omega_k^n K(z, z+(k-n)\Delta)g(k\Delta) = -g(n\Delta), \tag{B.15}$$

where ω_k^n is the weighting function for the trapezoidal integration rule, which is

$$\omega_k^0 = 0 \quad \text{and} \quad \omega_k^n = \Delta \begin{cases} 0, & k < 0 \\ \frac{1}{2}, & k = 0 \\ 1, & 0 < k < n \\ \frac{1}{2}, & k = n \end{cases}. \tag{B.16}$$

The case $k = 0$ and $k = n$ for ω_k^n stem from the start and end point of the integration as they contribute only half the weight compared with the interior points. The discretization scheme is a linear equation of $n+2$ unknowns $K(z,\cdot)$, however, by extending the summation k over all $N+1$ unknowns, the same discretization scheme is equivalently described by

$$\vec{\Omega}_n \cdot \vec{K} = -g(n\Delta), \tag{B.17}$$

where

$$\vec{\Omega}_n = \vec{e}_{n+1} + \begin{pmatrix} \omega_{n-N}^n g\left((n-N)\,\Delta\right) \\ \vdots \\ \omega_n^n g(n\Delta) \end{pmatrix} \in \mathbb{R}^{N+1} \quad \text{and} \quad \vec{K} = \begin{pmatrix} K(z, z-N\Delta) \\ \vdots \\ K(z,z) \end{pmatrix} \in \mathbb{R}^{N+1}, \tag{B.18}$$

and $\vec{e}_{n+1} \in \mathbb{R}^{N+1}$ denotes the unit vector in the cartesian coordinate system. Hence, by establishing the discretization scheme for all $n = 0, \ldots, N$ one obtains a linear system of $N+1$ equations in $N+1$ unknowns $\vec{K}$

$$\Omega \cdot \vec{K} = -G, \tag{B.19}$$

where $\Omega = \left(\Omega_n^{\mathsf{T}}\right)_{n=0}^{N} \in \mathbb{R}^{(N+1)\times(N+1)}$ and $G = \left(g(n\Delta)\right)_{n=0}^{N} \in \mathbb{R}^{N+1}$. To solve the linear equation a LU decomposition of the matrix $\Omega = LU$ is a promising ansatz with U and

L being an upper and lower triangular matrix, respectively. The equation then reads

$$U\vec{K} = -L^{-1}G, \tag{B.20}$$

and the desired value $K(z,z)$ is computed from the last entry of the vector $L^{-1}G$ and matrix U

$$K(z,z) = \frac{-(L^{-1}G)_{N+1}}{U_{N+1,N+1}}. \tag{B.21}$$

The LU decomposition of a single Ω has a complexity of $\mathcal{O}(N^3) = \mathcal{O}(z^3/\Delta^3)$ and hence a complete determination of V on the grid G has a complexity of $\mathcal{O}(N^4)$.

Utilizing the Structure of the Discretization Matrix

The matrix Ω is the sum of the identity matrix $\mathbb{1}_{N+1}$ with a mirrored (at a virtual vertical line) lower triangle matrix. For example Ω for $N = 6$ has the structure

$$\Omega = \begin{pmatrix} 1 & 0 & 0 & 0 & 0 & 0 & 0 \\ 0 & 1 & 0 & 0 & 0 & \frac{1}{2}g_0 & \frac{1}{2}g_1 \\ 0 & 0 & 1 & 0 & \frac{1}{2}g_0 & g_1 & \frac{1}{2}g_2 \\ 0 & 0 & 0 & 1+\frac{1}{2}g_0 & g_1 & g_2 & \frac{1}{2}g_3 \\ 0 & 0 & \frac{1}{2}g_0 & g_1 & 1+g_2 & g_3 & \frac{1}{2}g_4 \\ 0 & \frac{1}{2}g_0 & g_1 & g_2 & g_3 & 1+g_4 & \frac{1}{2}g_5 \\ \frac{1}{2}g_0 & g_1 & g_2 & g_3 & g_4 & g_5 & 1+\frac{1}{2}g_6 \end{pmatrix} \in \mathbb{R}^{7\times 7},$$

where $g_i = \Delta g(i\Delta)$ is used as an abbreviation. The top first row of Ω corresponds to the integral equation evaluated at $t = -z$, where the integral vanishes due to the integration limits being equal. The ones on the diagonal originate from the term $K(z,t)$ in the integral equation (B.14) and the lower triangular structure is only due to the integral, where the prefactor of $\frac{1}{2}$ indicates the integration limits.

To discuss another structural feature of Ω the notion of an *inner* matrix is required.

Definition 2. *Let $A = (a_{ij})_{i,j=1,\dots,N} \in \mathbb{R}^{N\times N}$ with $N > 2$ be a square matrix. The* inner *matrix $A' = (a_{ij})_{i,j=2,\dots,N-1} \in \mathbb{R}^{(N-2)\times(N-2)}$ is obtained by removing the top and bottom rows together with the left and right columns of A. The consecutive application of the inner matrix is denoted by $A^{(k)}$ and is defined by $A^{(k+1)} = \left(A^{(k)}\right)'$ with $A^{(0)} = A$ and $A^{(1)} = A'$.*

Denote by $\Omega(z) = \Omega$ the discretization matrix for the GLM integral equation at depth z. The matrix $\Omega(z)$ is then self similar, meaning that the inner matrix $\Omega(z)'$ after a scaling of the last column by $\frac{1}{2}$ corresponds to the same integral equation but at a depth $z \to z - \Delta$. More precisely, denote by $T(z)$ the triangular part of $\Omega(z)$,

$$A = \begin{pmatrix} a_{11} & a_{12} & a_{13} & a_{14} & a_{15} & a_{16} & a_{17} \\ a_{21} & a_{22} & a_{23} & a_{24} & a_{25} & a_{26} & a_{27} \\ a_{31} & a_{32} & a_{33} & a_{34} & a_{35} & a_{36} & a_{37} \\ a_{41} & a_{42} & a_{43} & \boxed{a_{44}} & a_{45} & a_{46} & a_{47} \\ a_{51} & a_{52} & a_{53} & a_{54} & a_{55} & a_{56} & a_{57} \\ a_{61} & a_{62} & a_{63} & a_{64} & a_{65} & a_{66} & a_{67} \\ a_{71} & a_{72} & a_{73} & a_{74} & a_{75} & a_{76} & a_{77} \end{pmatrix} \in \mathbb{R}^{7\times 7}$$

Figure B.1: Illustration of the definition of the *inner* matrix.

i. e. $T(z) = \Omega(z) - \mathbb{1}_{N(z)}$, then one has

$$\Omega(z-\Delta) = \mathbb{1}_{N(z)-2} + T'(z) \cdot \begin{pmatrix} 1 & & & \\ & \ddots & & \\ & & 1 & \\ & & & \frac{1}{2} \end{pmatrix} = \mathbb{1}_{N(z-\Delta)} + T(z-\Delta). \tag{B.22}$$

This structural feature of $\Omega(z)$ can be exploited to reduce the number of LU decompositions and thus drastically speed up the inversion algorithm. The idea is to replace the LU decomposition of $\Omega(z-k\Delta)$ for any k with the LU decomposition of $\Omega(z)$. Hence, only one LU decomposition of the $\Omega(z) \in \mathbb{R}^{(N+1)\times(N+1)}$ matrix has to be calculated, while the other LU decompositions $\Omega(z-k\Delta) \in \mathbb{R}^{(N+1-2k)\times(N+1-2k)}$ are derived from the first one. In particular, as only the last entry of $\vec{K}$ is needed, the following approximations for the LU decomposition of $\Omega(z-k\Delta)$ are made for $1 \le k \le \frac{N}{2}$

$$\begin{aligned} U_{N+1-2k,N+1-2k}(z-k\Delta) &\approx \frac{1}{2}\left(\left(U^{(k)}(z)\right)_{N+1-2k,N+1-2k} + 1\right) \\ L^{-1}(z-k\Delta) &\approx (L^{-1})^{(k)}. \end{aligned} \tag{B.23}$$

The computation of the kernel K is then carried out as follows

$$\begin{aligned} K(z,z) &= \frac{-(L^{-1}(z)G)_{N+1}}{U_{N+1,N+1}(z)} \\ K(z-\Delta k, z-\Delta k) &= \frac{-2\left((L^{-1})^{(k)}G_k\right)_{N+1-2k}}{\left(U^{(k)}(z)\right)_{N+1-2k,N+1-2k}+1}, \quad \text{for} \quad 1 \le k \le \frac{N}{2}, \end{aligned} \tag{B.24}$$

where G_k is the vector obtained by removing $2k$ rows from the bottom of G.

The LU decomposition of $\Omega(z) = L(z)U(z)$ and the inverse of L is required for determining $K(z,z)$. Both operations are of order $\mathcal{O}(N^3)$ and to evaluate the kernel on other

grid points, only the inner matrix of L^{-1} and U are required, which are computational negligible, resulting in a total computational complexity of $\mathcal{O}(N^3)$.

List of Figures

List of Tables

List of Publications

1. **A. Book**, S. Mayr, J. Stahn, P. Böni, W. Kreuzpaintner, *Phase Reconstruction of a Cu(001) Seed Layer from in situ Polarized Neutron Reflectometry Data using Fe Reference Layers.* Nucl. Inst. Meth. Phys. Res. A (submitted) (2021)

2. W. Kreuzpaintner, A. Schmehl, **A. Book**, T. Mairoser, J. Ye, B. Wiedemann, S. Mayr, J.-F. Moulin, J. Stahn, D. Gilbert, H. Gabold, Z. Inanloo-Maranloo, M. Heigl, S. Masalovich, R. Georgii, M. Albrecht, J. Mannhart, P. Böni, *Reflectometry with Polarized Neutrons on In Situ Grown Thin Films.* Physica Status Solidi B doi: 10.1002/pssb.202100153 (2021)

3. **A. Book**, P. Kienzle, *Retrieval of the Complex Reflection Coefficient below the Critical Edge for Neutron Reflectometry.* Physica B, 412181 (2020). doi: 10.1016/j.physb.2020.412181

4. J. Ye, **A. Book**, S. Mayr, H. Gabold, F. Meng, H. Schäfferer, R. Need, D. Gilbert, T. Saerbeck, J. Stahn, P. Böni, W. Kreuzpaintner, *Design and Realization of a Sputter Deposition System for the in situ and in operando Use in Polarized Neutron Reflectomtry Experiments: Novel Capabilities.* Nucl. Inst. Meth. Phys. Res. A, 133710 (2020). doi: 10.1016/j.nima.2020.163710

List of Abbreviations

BA	Born-Approximation
BLAS	Basic Linear Algebra Subprograms
CDF	Cumulative Distribution Function
DE	Differential Evolution
DREAM	Differential Evolution Adaptive Metropolis
GLM	Gel'fand-Levitan-Marchenko
GMR	Giant Magnetoresistance
GPU	Graphical Processing Unit
MCMC	Markov Chain Monte Carlo
MH	Metropolis-Hastings
MLE	Maximum Likelihood Estimator
MRAM	Magnetoresistive Random Access Memory
$\mathbf{MSE_{log}}$	Mean Squared Logarithmic Error
$\mathbf{MSE_{sqrt}}$	Mean Squared Root Error
MSWE	Mean Squared Weighted Error
NIST	National Institute of Standards and Technology
PDF	Probability Density Function
PNR	Polarized Neutron Reflectometry
PSI	Paul Scherrer Institut
SINQ	Swiss Spallation Neutron Source
SLD	Scattering Length Density
TMR	Tunnel Magnetoresistance
XRR	X-Ray Reflectometry

Acknowledgments

This thesis would not have been possible without the assistance, support and advice of various people. I would like to express my sincere gratitude to the following persons:

- My supervisor Prof. Dr. Peter Böni. Thank you for the opportunity for working on this thesis. Especially, I want to thank you for the support and ideas you gave me and the independent working atmosphere at your chair during the last four years. It was always a pleasure discussing problems with you.

- My advisor Prof. Dr. Wolfgang Kreuzpaintner. Thank you for pushing me to pursue my Ph.D. and spending so much time teaching me XRR/XRD and all the little quirks of the "old but gold" D5000/D8 diffractometers. I really appreciate the time we spent together on conferences, measuring samples with the *in situ* chamber at Amor and repairing all kind of devices, especially the diffractometers when nobody had an idea and it was just a broken light bulb.

- The NIST Center for Neutron Research (NCNR) team including Charles Majkrzak, Paul Kienzle, Brian Maranville and Ryan Need and the team of the Polarized Beam Reflectometer (PBR) and MAGIK Reflectometer. Thank you for the opportunity to stay at the NCNR and learn so much about neutron reflectometry and statistics. It was a wonderful time and in particular the cake club every Friday with self-made delicious cakes was a nice and welcomed distraction.

- My colleagues at E21 and E51 chair for the great atmosphere at work and all the activities after work like the chinese hot pot dinners, slackline in the westpark, coffee breaks (even though I never drank coffee), biking tours and the full-time discord sessions we established during the corona crisis. In particular, I want to thank Lukas Beddrich, Ran Tang, Christoph Herb, Jingfan Ye, Sina Mayr and, last but not least, Henrik Gabold for the extraordinary discussions and jokes at work. I want to thank Stefan Giemsa for his assistance concerning all technical problems. Further, I thank Fankai Meng, Helena Schäfferer, Jan-Henrik Schmidt-Dencker, Zyad Benoun and Mahla Bakshi for their contributions for upgrading the sputtering chamber during their time as working students.

- The team at the Amor beamline at PSI, in particular Dr. Jochen Stahn, for their help setting up the deposition chamber on the beamline and the ad-hoc repairment of the internal heating system.

- My parents, sister and friends for their encourage over the duration of this thesis.

Acknowledgments

Funding by the Deutsche Forschungsgemeinschaft (DFG, German Research Foundation) within the Transregional Collaborative Research Center “From electronic correlations to functionality” - Projekt ID 107745057 - TRR 80 is acknowledged.